Review Article

Nano Research
2022, 15(8): 6888–6923

ISSN 1998-0124 CN 11-5974/O4
https://doi.org/10.1007/s12274-022-4371-x

Understanding the structure–performance relationship of active sites at atomic scale

Runze Li and Dingsheng Wang (✉)

Department of Chemistry, Tsinghua University, Beijing 100084, China

Received: 13 February 2022 / **Revised:** 22 March 2022 / **Accepted:** 28 March 2022

ABSTRACT

Metal-based atomically dispersed catalysts have attracted more attention because of their excellent catalytic performance and nearly 100% atom utilization. Therefore, it is very important to comprehensively and systematically understand the relationship between catalytic active sites and catalytic performance at atomic scale. Here, we discuss and summarize in detail the key and fundamental factors affecting the active site, and relate them to the catalytic performance. First, we describe the effectiveness of active site design by coordination effects. Then, the role of chemical bonds in the active sites in changing the reaction performance is discussed. In addition, for intermetallic compounds, we explore how the spacing of active atoms affects the catalytic behavior. Moreover, the importance of synergistic effect in catalyst design is further discussed. Finally, the key parameters affecting the catalytic performance at atomic scale are summarized, and the main challenges and development prospects of atomic catalysts in the future are put forward.

KEYWORDS

single-atom catalysts, coordination environment, structure–performance relationship, electronic structure, synergistic effect

1 Introduction

With the increasing consumption of fossil energy, it is cumulatively urgent to reduce the dependence on non-renewable resources. The design and preparation of cheap and efficient catalysts in the energy field are highly important for both basic research and industrial application [1–4]. Generally speaking, noble metal catalysts have high intrinsic catalytic activity due to their unique electronic structure. However, the high cost, low reserves, and poor stability of noble metal catalysts restrict their commercial application [5, 6]. Reducing the metal loading of transition metal (TM) catalysts is an effective way to reduce the cost. When the metal loading is reduced, the utilization of metal atoms must be increased to maintain the original activity of the catalyst. Designing catalysts at atomic scale is the most efficient way to make full use of each atom on the supported catalysts, creating single-atom catalysts (SACs) [7–17]. For example, Zhang et al. reported the synthesis of single-atom catalysts, in which isolated platinum atoms are anchored on the surface of FeO_x nanocrystals, showing high activity and satisfactory stability for CO oxidation and having preferential oxidation of CO [18]. SACs also inherit the advantages of homogeneous and heterogeneous catalysts [19, 20]. The physical and chemical properties of fixed isolated atoms depend on quantum size effects as well as metal–support interactions, unlike metal nanoparticles (NPs) [21–24]. Unsaturated coordination environments and unique electronic structures have been shown to have great potential for improving catalytic activity in a variety of reactions [25–30]. The isolated geometry of metal species provides unparalleled selectivity as well as even higher activity than nanoparticles in a great number of reactions. In addition, due to their simplicity and homogeneity, these active sites can be accurately identified and characterized, which contributes to a deep and comprehensive understanding of the relationship between their structure and catalytic performance, facilitating the development of rational catalyst designs for targeting reactions at atomic scale [31–34]. However, the properties of single-atom sites are not determined only by isolated individual atoms. The homogenous active sites and their surrounding environment have a very important influence on the catalytic performance [35, 36]. Adjusting the electronic structure of metal centers is a practical strategy to improve the catalytic activity. With electronic adjustment, a redistribution of spin and charge density occurs, leading to an enhancement of catalytic performance [37, 38]. Therefore, it is important to understand the relationship between the structure of active sites and catalytic performance at atomic scale for rational design of catalysts and construction of definite active sites. How to build this long-sought bridge depends on finding key descriptors to build the understanding of the structure–performance relationship (Fig. 1).

It is well known that local coordination atoms around the active center have a profound effect on the activity, stability, and selectivity of single-atom catalysts [39–41]. It is of great significance to determine the relationship between the structure and performance of the local coordination environment of single-atom metal and the catalytic activity for further understanding the pathway and mechanism of the reaction. Coordination engineering by selectively manipulating coordination atoms in the metal center to improve their electronic environment is a very

Address correspondence to wangdingsheng@mail.tsinghua.edu.cn

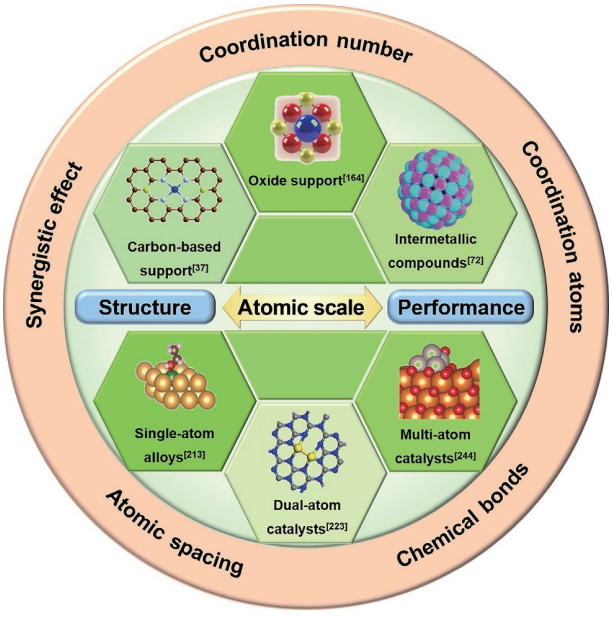

Figure 1 Overview of the topics covered in this review.

effective strategy for synthesizing SACs with specific functions, especially for carbon-supported SACs [42]. Among them, nitrogen-doped carbon (NC) is an impressive support for SACs because of its increased conductivity and wettability as well as the high stability of strong metal N covalent bonds and high metal loading by concentration-controlled N-doping [43–46]. In the case of most carbon-based materials as the supports, the central metal atoms of SACs are fixed to the supports by N atoms [47, 48]. In addition, the local coordination environment of SACs is reconstructed by replacing or injecting other non-metal elements into the original coordination structure, which causes the coordination atoms to contribute dynamic electrons to the metal central atoms, thus affecting the catalytic performance [49, 50]. In these catalytic systems, coordination species with lone electron pairs, such as N, P, and S, can not only capture isolated metal centers, but also regulate their electronic structures. Therefore, reasonable design strategy, fine preparation of the environment atoms of single-atom sites, and regulation of the coordination number and species of the coordination atoms and the coordination structure play a significant role in the activity, stability, and selectivity of SACs.

As a general concept in chemistry, chemical bond is also crucial to the regulation of active sites in SACs [51, 52]. The properties of chemical bonds affect the charge distribution between atoms, and the effects of bond length, bond angle, and bond polarity should be considered. In addition, for nano catalysts, doping another metal atoms in one metal crystal to form intermetallic compounds can effectively adjust the spacing of active atoms, so as to better adapt to the requirements of catalytic reaction and improve selectivity without changing the active atoms [53, 54]. Therefore, although many intermetallic compounds cannot be called SACs, for some of them, the active sites are homogeneous and can be regulated by changes in atomic spacing. Chemical bond properties and atomic spacing can often be regulated by designing lattice strains [55, 56]. If a monolayer metal can be obtained, it will be a good model, and the effect of another atom doping on atomic spacing will be more intuitive.

SACs containing only a single active site may hinder their further application. On the one hand, some complex reactions require two or more active sites to activate reactants, but SACs are powerless in these reactions [57, 58]. On the other hand, since SACs have only a single active center, it is difficult to break the linear relationship between the adsorption energy of intermediates, which fundamentally limits the catalytic efficiency [59, 60]. Fortunately, synergistic effect of two or more atoms at the active sites has been discovered in recent years. This synergistic effect has the potential to change the adsorption configuration of the reactants and cause the catalytic reaction to exhibit a different reaction pathway than that of a single site, thus optimizing the catalytic performance. In single-atom alloys (SAAs), nanocrystals can optimize the electronic structure of isolated metal atoms, thus changing the activation barrier and the binding strength of reactants and intermediates, and regulating the catalytic performance [61–63]. On the other hand, the single atoms in SAAs can also regulate the electronic properties of the metal support, showing synergistic effects that are mutually optimized to meet the requirements of highly active and selective catalysts. In addition, dual-atom catalysts (DACs) with the smallest bridge active site and trinary-atom catalysts (TACs) with the smallest hollow site may have more applications in catalytic reactions [64–67]. In addition to the advantages of SACs, the main superiority is that they have higher metal atom loading and top, bridge, or hollow active sites, which are more flexible [68]. Therefore, an increase in the number of metal atoms forming the active site opens up new opportunities for catalytic reactions.

It is worth noting that the factors affecting the catalytic active sites at atomic scale are not isolated, but related to the whole. For example, in carbon-based supports, the change of coordination number or coordination shell will also change the chemical bond length simultaneously; while the doping of non-metal atoms will also change the coordination number of different atoms simultaneously [69, 70]. In addition, when the atomic spacing of active metal is adjusted, the reaction sites may change as quantitative change begets qualitative change [71–73]. Therefore, when studying specific catalysts, it is necessary to grasp the main contradiction and explore the main factors affecting the catalytic performance of the active site. On the other hand, we want to make it clear that many of the influencing factors are not fundamental. For example, the oxidation state of a metal atom can be determined by a variety of coordination structures [74, 75]. The strain of supports or metallic crystals can be attributed to the change of chemical bond length, bond angle, and active atomic spacing [52, 54, 76]. Therefore, by understanding the most important and essential descriptors affecting active sites, it is possible to develop a toolkit for understanding the structure–performance relationships of catalysts at atomic scale.

Advanced characterization techniques play an important role in the development of nano materials and provide useful information for the structural study of active sites. The morphology of catalytic materials can be directly observed by microscopy techniques. Among them, it is possible to directly observe lattice fringes or isolated single atoms with high resolution microscope, which provides direct evidence for the determination of active sites. Infrared (IR) spectroscopy uses appropriate probe molecules to evaluate the presence and proportion of single metal atoms on the supports. X-ray spectroscopy can provide information on the dispersion of isolated atoms, the coordination environment of active species, and the oxidation states of metal atoms. *In situ* X-ray absorption spectroscopy (XAS) can provide real-time structural changes of the catalytic active sites. Therefore, these advanced characterization techniques provide favorable support for understanding the relationship between structure and properties of catalysts.

How to understand the structure–performance relationship of catalytic active sites at atomic scale is very important for rational design of catalysts in the future. In this paper, the effects of local environment on catalytic performance of catalysts at atomic scale are discussed with typical examples. Firstly, we will discuss the

effects of coordination effects, including coordination number and species of coordination atoms, mainly in SACs with carbon-based materials as supports. We will then discuss the chemical bonds at the active sites, including bond length, bond angle, and bond polarity, to reveal the precise relationships between structure and performance of SACs. For metal nanocatalysts, we will focus on the effect of the active atomic spacing in intermetallic compounds with uniform active sites and metal atom layer on the catalytic performance. Further, we will explore the synergistic effect between different metal atoms through nanocatalysts with isolated metal sites and dual-atom catalysts. Based on the above discussion, a comprehensive summary will be made to clarify that differences in the structure of catalytic sites at atomic scale can explain the differences in catalytic properties observed at macroscopic scale. Finally, we will present some problems in the rational design of catalysts at atomic scale, and point out the direction for the design of atomic catalysts including single-atom catalysts in the future.

2 Coordination effect of active sites

Metal atoms do not drive the catalytic reaction alone, but together with coordination atoms determine the catalytic performance. The actual catalytic site of SACs greatly depends on local coordination environment [77–79]. For most carbon-based supports, the central metal atom of SACs is fixed by coordination bonds with non-metallic atoms, forming various coordination environments, as shown in Fig. 2. By adjusting the coordination environment, the electronic and geometric structure of the central metal atom can be adjusted to change the absorption activity of reactants on metal atoms, thus affecting the catalytic performance [42, 80, 81]. Therefore, it is of great significance to determine the relationship between the structure and performance of the local coordination environment of single-atom metal for further understanding of the reaction pathway and mechanism. On the one hand, the number of N atoms coordinated with the active metal atom directly determines the interaction between the metal atom and the supports as well as the overall catalytic performance, so the valence state of the metal atom can be affected by electronic structure. By constructing coordination vacancies, higher unsaturation of metal active centers can be achieved, thus improving the activity of metal atoms. On the other hand, changing the properties of coordination N atoms or introducing heteroatoms (P, S, B, Cl) can effectively optimize the electronic structure [27]. The substitution or injection of foreign atoms into the original coordination structure will reconstruct the local coordination environment of SACs, resulting in the coordination atoms contributing dynamic electrons to the metal central atoms. In addition, the bond length, bond angle, and bond polarity of coordination bonds also need to be considered. In this section, we will discuss the influence of coordination number and type of coordination atoms on the geometric structure and electronic structure of SACs supported by carbon-based materials, respectively, so as to clarify the diversity of coordination of active atoms and its influence on catalytic performance, and explore how to rationally design carbon-based single-atom catalysts.

2.1 Coordination number

On general N-doped carbon support, the metal atom center will form a four-coordination structure of the active site, which can be represented by $M–N_xC_y$ ($x + y = 4$) [82]. By adjusting the coordination number of N atom, the electronic structure of metal site can be effectively adjusted and the valence state of metal atom can be adjusted [80, 83–87]. In addition, the change of electronic structure caused by the change of O coordination number can also be observed on the oxide support. For example, as the coordination number of Pt–O decreases, the oxidation state of single-atom Pt is almost linearly correlated, indicating that its electronic structure is largely changed with local environment between the single atom and the surrounding donor atoms [88]. However, ideal $M–N_4$ sites exhibit theoretically unfavorable energy properties, leading to their low chemical activation. Some research demonstrated that the more unsaturated the central coordination is, the more likely it is to contact the substrate molecule and the better the catalytic performance [89, 90]. Therefore, a large number of studies have found that the catalytic performance of low-coordination $M–N_x$ ($x < 4$) site through vacancy is better than that of $M–N_4$ site [91–93]. Low coordination number will not only increase the adsorption opportunity of reactants, but also affect the actual catalytic reaction process in the catalytic system. However, the synthesis of low-coordination $M–N_x$ sites is more unstable than $M–N_4$ sites, which makes the preparation of catalysts difficult.

2.1.1 Change of N coordination number on N-doped carbon supports

Many studies have found that the structure of four N atom coordination can promote electron transfer and the formation of key intermediates. For example, for Co atom centers, the $Co–N_4$ structure showed the highest triiodide reduction reaction (IRR)

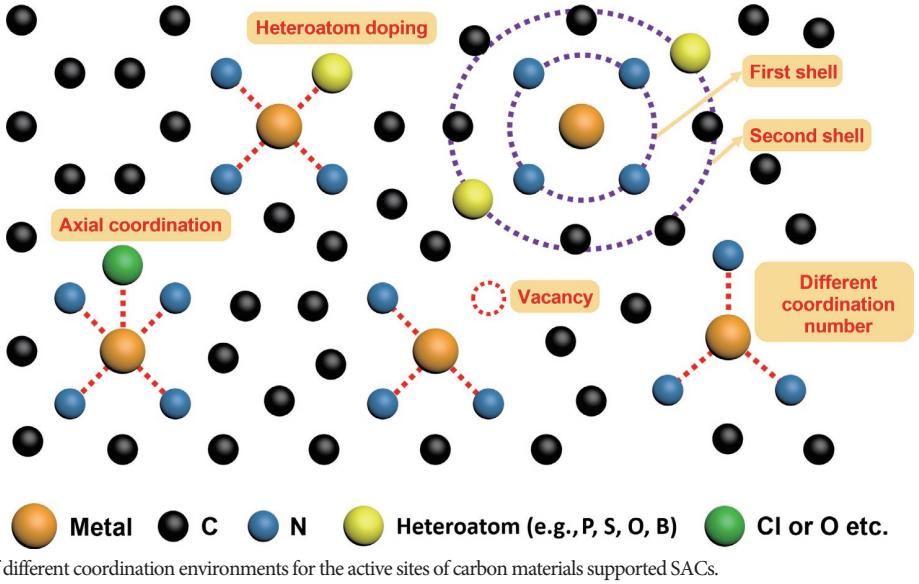

Figure 2 Illustrations of different coordination environments for the active sites of carbon materials supported SACs.

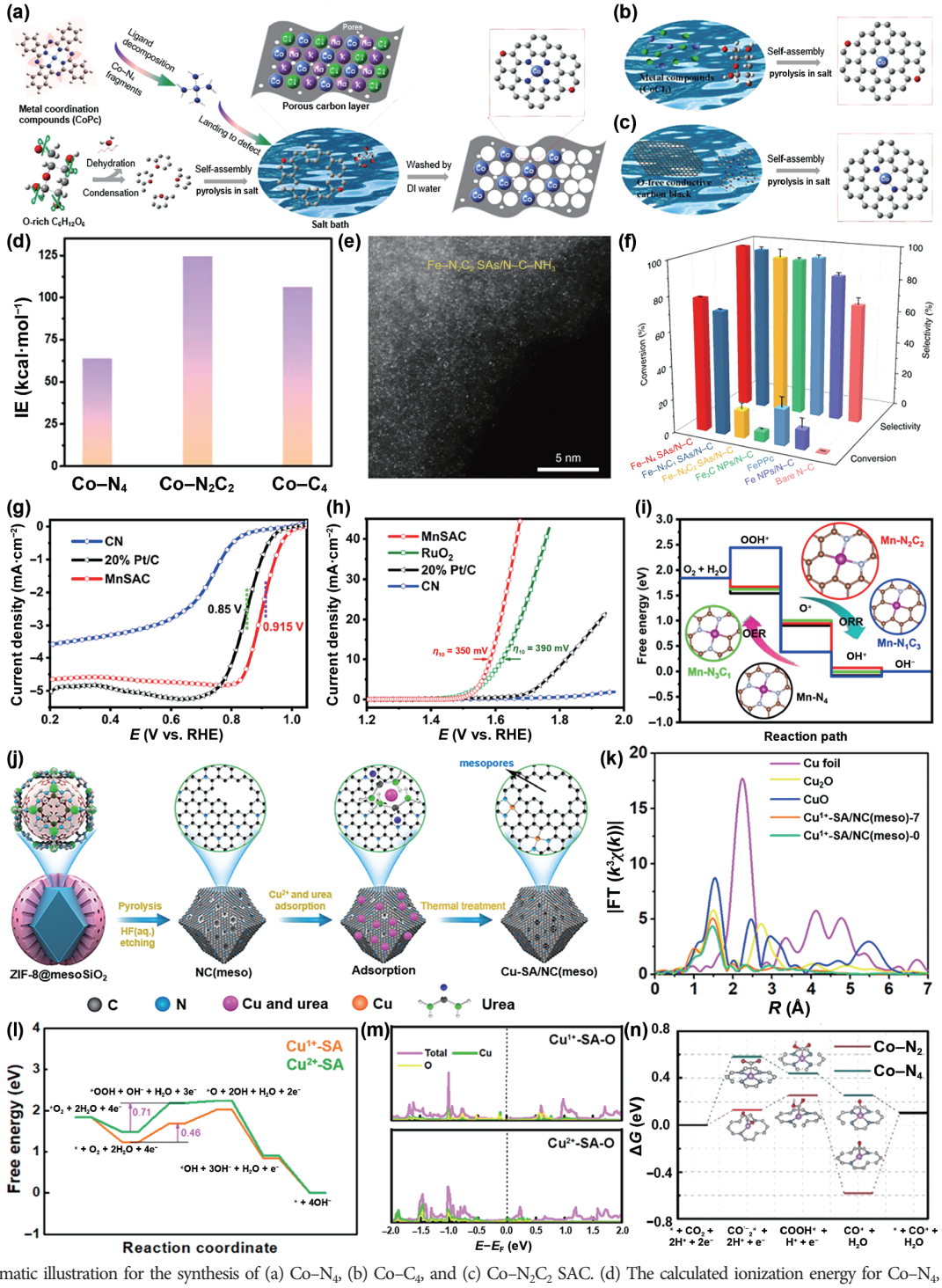

Figure 3 Schematic illustration for the synthesis of (a) Co–N_4, (b) Co–C_4, and (c) Co–N_2C_2 SAC. (d) The calculated ionization energy for Co–N_4, Co–N_2C_2, and Co–C_4, respectively. Reproduced with permission from Ref. [94], © Elsevier Ltd. 2021. (e) AC-HAADF-STEM image of the Fe–N_2C_2 SAs/N–C–NH_3. (f) Comparison of BOR performance of the as-synthesized different catalysts at 30 °C for 24 h. Reproduced with permission from Ref. [95], © Pan, Y. et al. 2019. (g) *iR*-corrected ORR polarization curves for MnSAC, CN, and 20% Pt/C. (h) *iR*-corrected OER polarization curves of MnSAC, CN, commercial RuO_2, and 20% Pt/C in 0.1 M KOH solution. (i) Theoretical ORR and OER activity of MnSAC. Reproduced with permission from Ref. [73], © American Chemical Society 2020. (j) The formation process of Cu-SA/NC(meso) catalysts. (k) Fourier transformed EXAFS spectra of the Cu K edge for Cu foil, CuO, Cu_2O, Cu^{1+}-SA/NC(meso)-7, and Cu^{2+}-SA/NC(meso)-0. (l) Free energy diagram for ORR reaction pathways on Cu^{1+}-SA active sites and Cu^{2+}-SA active sites in alkaline media (pH=13). (m) Total DOS for one oxygen absorbed Cu^{1+}-SA and Cu^{2+}-SA and PDOS of Cu atoms and O atoms from them. The O atoms are absorbed on the Cu sites. Reproduced with permission from Ref. [75], © American Chemical Society 2020. (n) Calculated Gibbs free energy diagrams for CO_2 electroreduction to CO on Co–N_2 and Co–N_4. Reproduced with permission from Ref. [96], © Wiley-VCH Verlag GmbH & Co. KGaA, Weinheim 2018.

activity [94]. As shown in Figs. 3(a)–3(c), special metal coordination complexes are introduced to form Co–N_4 with the single Co atom anchored with four coordination N atoms when the support contains O-rich defects. When conventional metal compounds are introduced, Co–C_4 is formed by isolated cobalt atoms occupying the oxygen vacancy of the support. When the defect is few, the metal complexes are hard to anchor, and the electron-deficit effect occurs after the self-coordination bond breaks, quickly forming Co–N_2C_2. Due to the unique coordination environment and layer porosity, dye-sensitized solar cells (DSCs) constructed from Co–N_4 active site counter electrode (CE) achieved the minimum peak-to-peak potential separation (264.02 mV) and the highest power conversion efficiency (7.43%), which was superior to noble Pt CE. The charge state of Co sites in

Co–N_4 and Co–N_2C_2 is more positive by about 0.60 |e|, while that in Co–C_4 is 0.49 |e|, reflecting that I_3^- more readily interacts electronically with the Co centers of Co–N_4 and Co–N_2C_2. As shown in Fig. 3(d), the ionization energy of Co–N_4 is the lowest (64 kcal·mol^{-1}), better than that of Co–N_2C_2 (124 kcal·mol^{-1}) and Co–C_4 (106 kcal·mol^{-1}), which illustrates that the geometrical structure of Co–N_4 has the strongest ability to accelerate electron transport. In addition, Chen et al. reported a series of Fe-based SACs with different coordination environment by a polymerization-regulated-pyrolysis strategy (Fig. 3(e)) [95]. The single-atom Fe sites anchored by four nitrogen atoms showed the highest benzene oxidation reaction (BOR) performance, with a conversion rate of 78.4% and phenol selectivity of 100% at 30 °C (Fig. 3(f)). The Auger spectra show that the valence state of Fe atoms in Fe–N_4 SAs/N–C catalysts is higher than those in Fe–N_3C_1 SAs/N–C and Fe–N_2C_2 SAs/N–C catalysts. The BOR activity of the single-atom Fe site catalyst decreased gradually as one or two C atoms replaced the coordination N, showing significant coordination sensitivity. The charge transfer between Fe–N_4 and O atoms is the strongest and the binding strength is the weakest. The increase of Fe–N coordination number promotes the formation and activation of the key intermediate O=Fe=O.

When different numbers of coordination N atoms are replaced by C atoms, the electronic structure of the active site can be adjusted more flexibly, so that the catalyst exhibits better performance. Considering different coordination numbers of N and C, Wang et al. constructed four possible structures of the central metal Mn [73]. The half-wave potential of oxygen reduction reaction (ORR) on Mn–N_2C_2 is 0.915 V under alkaline condition (Fig. 3(g)), and the overpotential (η) of oxygen evolution reaction (OER) is 350 mV at 10 mA·cm^{-2} (Fig. 3(h)). On the one hand, the whole process of Mn–N_2C_2 is exothermic, indicating that Mn–N_2C_2 has better ORR performance (Fig. 3(i)). On the other hand, the OER overpotential of Mn–N_4, Mn–N_3C_1, Mn–N_2C_2, and Mn–N_1C_3 are 0.981, 1.011, 0.871, and 2.061 V, respectively, indicating that Mn–N_2C_2 has the best OER performance among the four Mn–N_xC_y atomic models. The electronic properties show that the coordination environment has a significant regulating effect on the d-states peaks of Mn atom. The peak of about −2 eV on Mn–N_2C_2 confers itself a superior active site. In addition, highly efficient single Cu atom catalysts, consisting of high-density atomic Cu sites, have highly improved mesoporous structure and accessibility of active sites (Fig. 3(j)) [75]. The ratio of +1/+2 oxidation states of the Cu sites in Cu-SA/NC(meso) catalysts can change with the content of urea in the adsorption precursor, and the increase of Cu^{1+} sites can promote the ORR activity. The Fourier transform k^3-weighted extended X-ray absorption fine structure (FT-EXAFS) curves of Cu^{1+}-SA/NC(meso)-7 and Cu^{2+}-SA/NC(meso)-0 samples only show a significant peak at 1.5 Å (Fig. 3(k)), which can be attributed to the Cu–N and Cu–C coordination of the first shell, and the most possible structure of the active site is Cu–N_2C_2. Density functional theory (DFT) calculation shows that the rate-determining step (RDS) is the first protonation of the adsorptive O_2 species, and the forward reaction energy of the reaction is 0.46 and 0.71 eV, respectively (Fig. 3(l)), which results in a lower overpotential required to drive the ORR process on Cu^{1+}-SA than on Cu^{2+}-SA. Cu^{1+}-SA shows higher O_2 and OOH adsorption energy during efficient ORR compared with Cu^{2+}-SA, indicating that Cu^{1+}-SA has higher electrocatalytic activity in alkaline environment. The energy of the Cu 3d orbital of the Cu^{1+}-SA–O structure is close to the Fermi level, and that of some hybrid electronic states exceeds the Fermi level (Fig. 3(m)). As a result, the O 2p–d anti-bonding state is less occupied and the oxygen binding strength is greatly high. Wu et al. prepared a series of atomically dispersed Co catalysts with different nitrogen coordination numbers and studied their catalytic performance for CO_2 reduction reaction (CO_2RR) [96]. The best catalyst was the Co atoms coordinated with two N atoms. At 520 mV overpotential, the Faraday rate of CO formation was 94%, and the current density was 18.1 mA·cm^{-2}. As shown in the Gibbs free energy diagram of the CO_2 → CO pathway (Fig. 3(n)), the CO_2* formation energy is small, which explains the higher catalytic activity of CO_2RR. Jiang et al. reported a series of single-atom Ni catalysts with different N coordination numbers by controlling the pyrolysis temperature [97]. It is noteworthy that the Ni_{SA}–N_2–C catalyst with the lowest N coordination number has higher CO Faradaic efficiency (FE_{CO}; 98%) and turnover frequency (TOF; 1,622 h^{-1}) in CO_2RR, which is far superior to Ni_{SA}–N_3–C and Ni_{SA}–N_4–C. For all catalysts, the formation of COOH* intermediates is RDS. Obviously, the change of free energy (ΔG) required for RDS of Ni_{SA}–N_2–C catalyst is 1.42 eV, which is lower than that of Ni_{SA}–N_4–C (1.73 eV) and Ni_{SA}–N_3–C (1.45 eV). This indicates that COOH* is more easily formed at the Ni–N_2 site. In addition, the CO* desorption energy of Ni_{SA}–N_2–C is much lower (0.47 eV), indicating that Ni_{SA}–N_2–C catalyst is more likely to release CO* to generate CO.

In addition to the common four coordination structures, the three or five coordination structures of metal atoms can exhibit different electronic properties. For example, Chen et al. developed an N coordination strategy to design a stable CO_2RR electrocatalyst with atomically dispersed Co–N_5 anchored on polymer-derived N-doped hollow carbon spheres (Figs. 4(a)–4(d)) [98]. As shown in Fig. 4(e), in the potential range of 0.57 to 0.88 V, the catalyst has a high selectivity for CO_2RR, and FE_{CO} is above 90%. After 10 h of electrolysis, the CO current density and FE_{CO} remain basically unchanged, showing significant stability. Since creatine provides two different coordination sites (guanidine and carboxyl), Wang et al. selected creatine as the key ligand of the Cu complex and reported a dual-active site copper catalyst (DAS-Cu) containing both Cu–N_3 and Cu–N_4 sites [99]. The average coordination number of Cu atoms in DAS-Cu system is 3.3 and the average bond length is 1.94 Å. The data show that there are two different Cu atom sites in DAS-Cu, which are coordinated by three or four N atoms, respectively. The catalyst showed high catalytic performance (up to 97% yield) for oxyphosphorylation of alkenes, whereas the catalysts with the single active site (Cu–N_3 or Cu–N_4) were inert in this reaction. The Cu–N_3 site captures oxygen and triggers further oxidation processes, while the Cu–N_4 site provides a moderate adsorption site for protection of phosphine radicals.

2.1.2 *Vacancy effect*

It is a strategy to design active site structure by constructing coordination vacancy in the structure of active sites. Wang et al. successfully synthesized Co SACs with a metal loading of 23.58 wt.% on carbon nitride [100]. In FT-EXAFS spectra of Co SACs, only one main peak is located at 1.50 Å, corresponding to Co–N coordination of the first shell (Fig. 4(f)). The corresponding Co atom has a coordination number of about 2.3 and an average bond length of 1.95 Å. These results show that Co atoms are coordinated with two nitrogen atoms in Co SACs, which is consistent with DFT calculations. Under the same conditions, Co SACs have a higher TOF (19.6 h^{-1}) than other non-noble metal catalysts as well as high selectivity (97%) and stability. Co SACs have low energy barrier in the first basic step and high resistance against water, which makes the reaction have good catalytic performance. Furthermore, Co atoms in ZIF-67 can be converted to Co–N_3 coupling vacancy (Co–N_3–V) during the pyrolysis process by exactly controlling the precursor ratio of ZIF-67 to glucose in the molten salt medium [101]. When the catalyst was

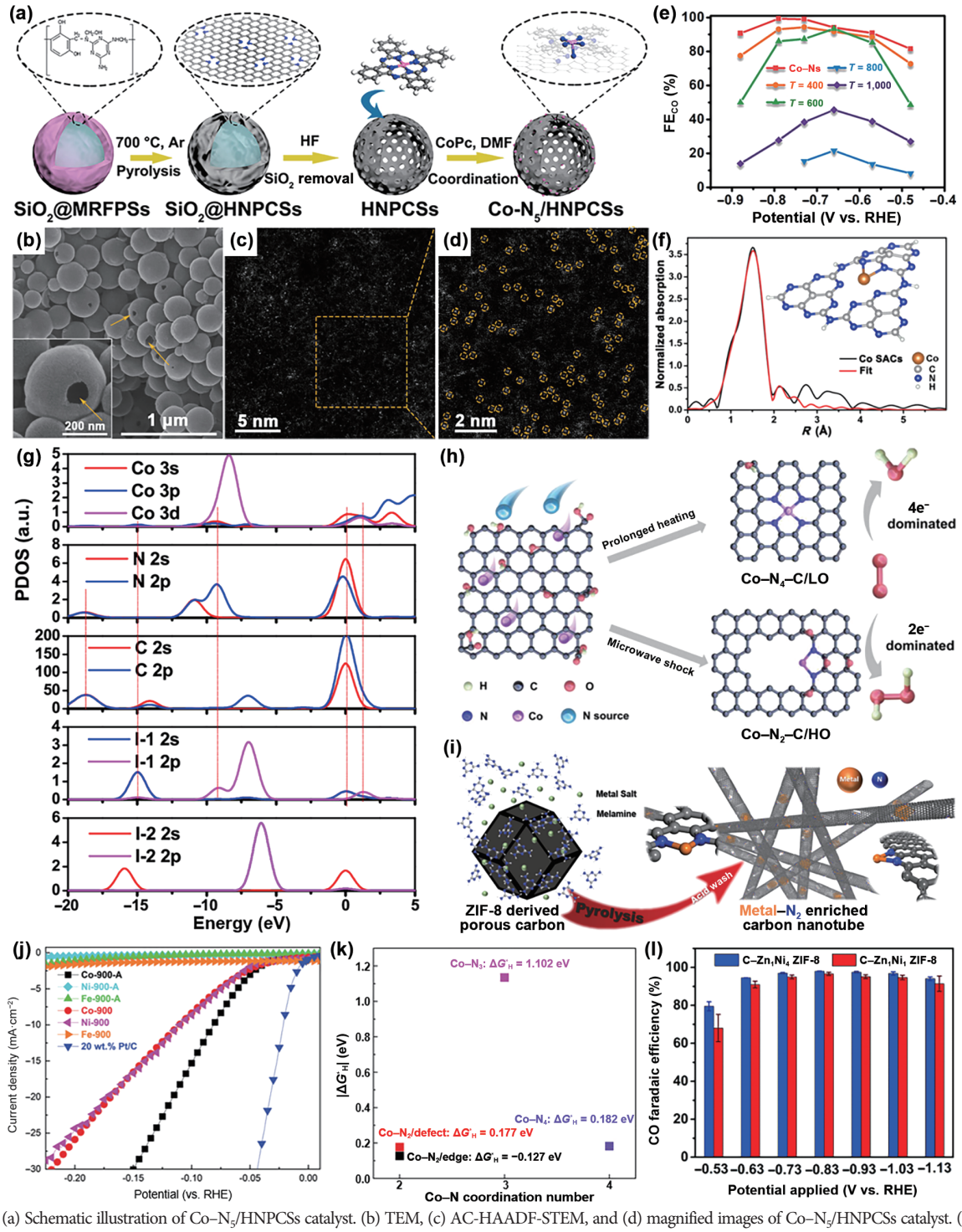

Figure 4 (a) Schematic illustration of Co–N_5/HNPCSs catalyst. (b) TEM, (c) AC-HAADF-STEM, and (d) magnified images of Co–N_5/HNPCSs catalyst. (e) FE_{CO} of Co–N_5/HNPCSs-T. Reproduced with permission from Ref. [98], © American Chemical Society 2018. (f) EXAFS curve fitting of Co SACs at *R* space. The inset is structure model of Co SACs. Reproduced with permission from Ref. [100], © Tsinghua University Press and Springer-Verlag GmbH Germany 2020. (g) PDOS for Co–N_3–V and I_2. I-1 and I-2 are the two I atoms in I_2. Reproduced with permission from Ref. [101], © American Chemical Society 2021. (h) Schematic diagram of the synthesis route to Co–N_4–C/LO and Co–N_2–C/HO. Reproduced with permission from Ref. [102], © Wiley-VCH GmbH 2021. (i) Illustration of the synthesis process. (j) Linear sweep voltammetric (LSV) curves of commercial Pt/C and various carbon-nanotube products before and after washing in 0.5 M H_2SO_4. (k) Calculated ΔG_H^* values of Co–N sites with different coordination numbers. Reproduced with permission from Ref. [103], © Wiley-VCH GmbH 2021. (l) Applied potential dependence of CO Faradaic efficiency measured in CO_2-saturated 0.5 M $KHCO_3$ solution with a catalyst loading of 0.088 mg·cm^{-2} for C-Zn_1Ni_4 ZIF-8 and 0.226 mg·cm^{-2} for C-Zn_1Ni_1 ZIF-8. Reproduced with permission from Ref. [104], © The Royal Society of Chemistry 2018.

used as CE for triiodide reduction reaction in dye-sensitized solar cells, the photoelectricity conversion efficiency was 7.89%, while Pt CE was 7.76%. The coordination number of central Co is three according to EXAFS fitting, indicating the existence of Co–N_3 site. The highest occupied molecular orbital–lowest unoccupied molecular orbital (HOMO–LUMO) position of Co–N3–V is suitable, which can shorten the electron transfer distance from CE to I_3^- and promote the succeeding reduction of I^-. As shown in Fig. 4(g), the orbital overlap of the interaction between Co–N, N–C, and Co–I-1 can also be discovered, indicating that a strong interaction of the Co–N bond, and there is an appropriate electron coupling between I-1 and Co–N_3–V, which is favorable for charge transfer.

Single-atom centers with low coordination by producing

vacancies may have higher catalytic properties than ideal quadridentate metal centers, which have been found on many Co or Ni based SACs. Fei et al. used a highly selective Co–N–C electrocatalyst with high H_2O_2 selectivity (91.3%) for H_2O_2 electrosynthesis by simultaneously adjusting the coordination number of atomically dispersed cobalt sites and nearby oxygen functional groups through one-step microwave thermal shock (TS) (Fig. 4(h)) [102]. In contrast to typical 4-electron ORR on $Co–N_4$ sites, this Co–N–C catalysts have low coordination with $Co–N_2$ configuration and rich epoxy groups, which synergically promote 2-electron ORR. In CoN_3 configuration, the limit overpotential of CoN_3H_5, CoN_3H_5–4O, and CoN_3H_5–4O–O are 1.06, 1.35, and 0.54 V, respectively, while in CoN_4 configuration, that of CoN_4–4O–O is 0.64 V. Therefore, the catalytic performance is sensitive to coordination configurations and oxygen functional groups. In addition, Liu et al. proposed a novel low-cost method to construct unique low-coordination metal atom sites dispersed on carbon nanotubes (CNT) for hydrogen evolution reaction (HER) (Fig. 4(i)) [103]. The abundance of Co–N sites with low coordination makes it have high catalytic activity in acidic electrolytes. As shown in Fig. 4(j), in 0.5 M H_2SO_4, the overpotential was only 82 mV at 10 mA·cm^{-2}. The Co–N fitting coordination number was confirmed to be 2.2, which is different from the commonly reported value of 3 or 4. Based on DFT simulation, the absolute value of H-adsorption Gibbs free energy ($|\Delta G_H^*|$) of $Co–N_2$ located within defects is 0.177 eV (Fig. 4(k)). Compared with ΔG_H^* values of $Co–N_3$ (−1.102 eV) and $Co–N_4$ (0.182 eV), these common high coordination Co–N single-atom sites showed lower intrinsic HER activity than the low coordination Co–N single-atom sites proposed in this study.

For Ni single atom, Bao et al. successfully synthesized coordination unsaturated Ni–N on porous carbon-doped with nickel loading up to 5.44% [104]. The CO current density reached 71.5 mA·cm^{-2} at the voltage of 1.03 V, and FE_{CO} remained 92.0%–98.0% in the voltage from −0.53 to −1.03 V (Fig. 4(l)). C-Zn_1Ni_4 ZIF-8 has a coordination number of 2.4 ± 0.4, indicating that Ni species are in coordination unsaturated state. The free energy of *COOH (G_{*COOH}) of NiN_3, NiN_3V, and NiN_2V_2 with unsaturated coordination is significantly lower than that of NiN_4. Especially for NiN_2V_2, G_{*COOH} (0.62 eV) is lower than G_{*H} (0.69 eV), indicating that it has a high selectivity for CO_2RR. In addition, Joo et al. used Ni(II) phthalocyanine molecules grafted onto CNT (NiPc/CNT) and NiPc/CNT (H-NiPC/CNT) after heat treatment as model catalysts to investigate the effect of thermal activation on the active center structure and CO_2RR activity (Fig. 5(a)) [105]. EXAFS analysis and DFT calculations show that heat treatment transforms the $Ni^{2+}–N_4$ site into $Ni^{+}–N_3V$. The presence of $Ni^{+}–N_3$ sites in graphene results in the local structural shrinkage of Ni–N–C and the reduction of the central oxidation state of Ni from +2 to +1. The hydrogen adsorption free energy of $Ni–N_3$ site is too close to 0, which will increase HER rate and decrease CO selectivity, indicating that $Ni–N_3V$ is more likely to be the active site of CO_2RR than $Ni–N_3$. Lu et al. used precursors containing oxygen and nitrogen atoms to generate vacancy defects $Ni–N_3–V$ by removing oxygen atoms in initially formed $Ni–N_3O$ at high temperature [106]. Vacancy defects in $Ni–N_3–V$ SAC can significantly improve the electrocatalytic reduction activity for CO_2RR. As shown in Figs. 5(b) and 5(c), the current density of $Ni–N_3–V$ SAC is up to 65 mA·cm^{-2}, and the Faraday efficiency is over 90% at –0.9 V as well as the high TOF of 1.35×10^5 h^{-1}, much higher than those of $Ni–N_4$-SAC. DFT calculation shows that the free energies of $Ni–N_4$, $Ni–N_3–V$, and $Ni–N_3$ are 1.649, 0.680, and −0.061 eV, respectively, indicating that $Ni–N_3$ has the most favorable ΔG (Fig. 5(d)). In the fourth step, the active center of $Ni–N_3$ is difficult to release CO, and the calculated free energy (ΔG = 1.264 eV) is the largest among the three catalysts, indicating that $Ni–N_3$ without vacancy is not an effective SAC for CO_2RR.

2.1.3 *Change of O coordination number on oxide supports*

For SACs supported by oxides, the metal atoms are coordinated with the oxygen donor on the support. Due to the rigid crystal structure of the oxide supports, the $M–O_x$ structure is harder to change than $M–N_x$. Therefore, it is a challenged task to control the coordination environment without destroying the dispersion on oxides. The electronic structure of metal active center can also be optimized by adjusting O coordination number. For example, Zhang et al. successfully modelled the coordination and oxidation states of single Pt atom by changing the rapid thermal treatment (RTT) temperature [88]. When the RTT temperature increases from 500 to 600 °C, the coordination number of the first layer Pt–O decreases from 3.8 to 1.8, and Pt–Fe coordination begins to occur at 525 °C, but its contribution is relatively small. At the same time, the strength of white line decreases gradually, indicating that the oxidation state of Pt decreases. The precursor (Pt_1/FeOOH-RT) has an average Pt oxidation state of 2.46. For Pt_1/Fe_2O_3-600, the average oxidation state of Pt decreases to 0.56 (Fig. 5(e)). Pt_1/Fe_2O_3-600 exhibited the strongest activity, with TOF of 3,809 h^{-1} at 40 °C and 21,099 h^{-1} at 60 °C. Figure 5(f) demonstrates the relationship between catalytic activity and coordination structure. DFT calculations show that Pt Bader charge of the three coordination Pt_1/Fe_2O_3-550 catalyst is +1.31 |e|, higher than that of two coordination Pt_1/Fe_2O_3-600 catalyst (+0.78 |e|), but less than that of four ligand Pt_1/Fe_2O_3-500 catalyst. At 300 K, the reaction energies of Pt_1/Fe_2O_3 with four coordination, three coordination and two coordination are −1.48, −1.71, and −1.87 eV, respectively (Fig. 5(g)). Therefore, the Pt single atom is more likely to activate H_2 molecules with the decrease of the content of Pt–O, making its activity in hydrogenation reaction several times higher.

2.2 Coordination atoms

Precise control of the coordination environment of a single metal active center in $M–N_x$ can effectively alter the electronic structure, which can be achieved by two strategies: One is to adjust the type of atoms that directly coordinate with the metal active center, and the other is to influence the electronic structure by using long-range interactions of the metal active center with heterogeneous atoms on the support. Coordination species, such as N, O, P, and S with lone electron pairs, and B with vacant orbitals, can not only capture isolated metal centers, but also regulate their electronic structure [50]. In addition, recent studies have shown that Cl atoms with axial coordination can also regulate the activity of metal sites [41, 107, 108]. Therefore, regulating the type and structure of coordination atoms plays an important role in the activity, stability, and selectivity of SACs.

2.2.1 *Different properties of coordination N atoms*

The properties of N atoms have a great influence on the metal centers of $M–N_x$ as well as the catalytic performance [109–111]. In general, N 1s X-ray photoelectron spectroscopy (XPS) can be reflected into three different peaks at 398.3, 399.9, and 400.9 eV, corresponding to pyridine-N, pyrrole-N, and graphite-N, respectively [112, 113]. Different types of N have different characteristics, resulting in different catalytic behaviors of metal centers [114–116]. Due to geometric effects, pyridine-N and pyrrole-N anchor single atoms more easily than graphite-N. However, since nitrogen doping in NC is usually random, fine control of the type of nitrogen doping is required to reveal its effect on the performance of SACs. Changing the doping temperature of different nitrogen source molecules, using metal

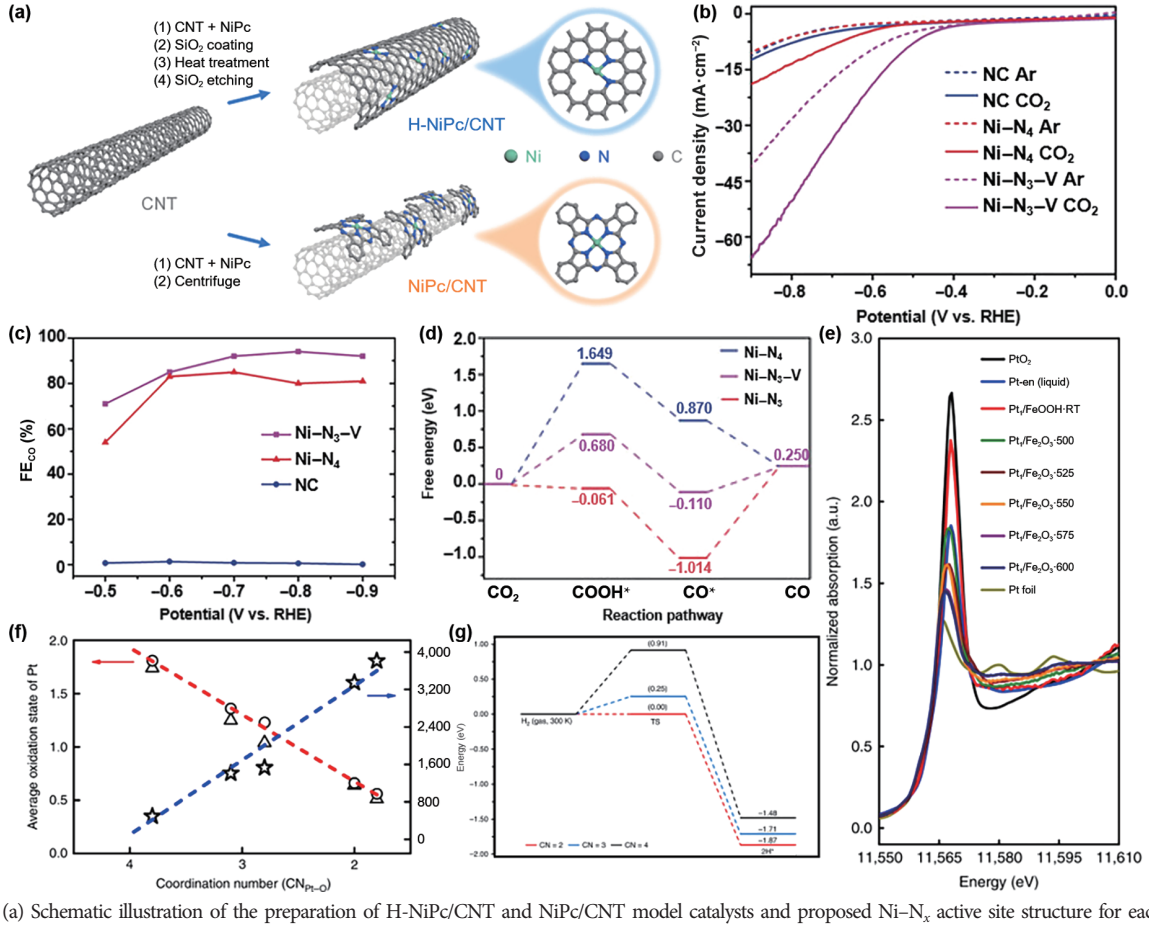

Figure 5 (a) Schematic illustration of the preparation of H-NiPc/CNT and NiPc/CNT model catalysts and proposed Ni–N_x active site structure for each catalyst. Reproduced with permission from Ref. [105], © American Chemical Society 2020. (b) Linear sweep voltammetric curves in N_2 or CO_2-saturated 0.5 M $KHCO_3$ electrolyte, with a scan rate of 1 mV·s^{-1}, and a stirring rate of 550 rpm using a magnetic stirring bar. (c)Faradaic efficiencies for CO. (d) Calculated free-energy diagram for the conversion of CO_2 to CO. Reproduced with permission from Ref. [106], © Wiley-VCH Verlag GmbH & Co. KGaA, Weinheim 2020. (e) The normalized XANES spectra of the structure evolution of Pt species in different stages of preparation. (f) The correlation between coordination structure and catalytic performance. The star, triangle, and circle represent TOF, average oxidation state of Pt determined from XPS, and XANES, respectively. (g) Energy profiles of H_2 dissociation on Pt_1/Fe_2O_3-T catalysts at 300 K. Reproduced with permission from Ref. [88], © Ren, Y. J. et al. 2019.

salts as modifiers during pyrolysis, and applying special physical techniques such as laser irradiation have been used to customize doped N species in NC materials [117–119]. Therefore, we used pyridine-N and pyridine-N as representatives to reveal their potential effects on the performance of supported SACs.

Many theoretical studies have compared the coordination effects of pyridine-N and pyrrole-N. Huang et al. constructed two possible models of pyridine-N_4–Fe and pyrroe-N_4–Fe on hierarchically N-doped porous carbon (FeSA/HNPC) [120]. As shown in Fig. 6(a), OOH* formation is the RDS of the pyrrole-N_4–Fe model. It is found that RDS on pyridine-N_4–Fe is the last electron transfer step in the formation of OH^-. The free energy of pyrrole-N_4–Fe (0.16 eV) is lower than that of pyrrole-N_4–Fe (0.28 eV), indicating that ORR occurs preferentially on pyrrole-N_4–Fe rather than on pyridine-N_4–Fe in FeSA/HNPC. In addition, Cao et al. proposed the coordination model of Fe@pyridinic N and Fe@pyrrolic N with Fe–N_4 in order to reveal the source of the high ORR activity of SA-Fe/NG [121]. The theoretical onset potential of Fe@pyrrolic N(Fe) was higher than that of Pt (111), while that of Fe@pyridinic N(Fe) was lower than that of Pt (111). The results revealed that the high ORR activity of SA-Fe catalyst is derived from Fe@pyrrolic N species. Moreover, pyridine-N is also sometimes more advantageous than pyrrole-N. For example, Li et al. prepared three metal-pyridine N single atoms fixed on a nitrogen-doped carbon matrix (M–N–C, M = Fe, Co, Ni) and investigated their performance as CO_2RR catalysts [122]. A single metal atom with four pyrrole N atoms coordination (M–pdN_4) was calculated as a catalyst model and compared with M–pdN_4. The *COOH free energy on Ni–pdN_4 and Co–pdN_4 is significantly lower than that on Ni–poN_4 and Co–poN_4, indicating that Ni and Co single atoms with four pyridine N coordination have higher activity. Although *COOH is more easily formed on Fe–pdN_4 than Fe–poN_4, the desorption of *CO on Fe–pdN_4 is more difficult than that on Fe–poN_4.

Differences in the properties of single atoms coordinated with pyridine N or pyrrole N have been observed experimentally. For example, Hu et al. reported a dispersed single-atom Fe site catalyst that generated CO at an overpotential as low as 80 mV [123]. As shown in Fig. 6(b), the local current density reached 94 mA/cm^{-2} at 340 mV overpotential. For Fe 0.5d and Fe–N–C, active sites for Fe ion coordination with four pyridine N are proposed. For Fe^{3+}–N–C, XPS spectra and X-ray absorption near-edge structure (XANES) indicate coordination of Fe ion with pyrrole N (Figs. 6(c) and 6(d)). Pyrrole N coordination stabilizes Fe^{3+} relative to Fe^{2+}, while pyridine N coordination does the opposite. *Operando* X-ray absorption spectra show that pyrrole ligands are very important for keeping the Fe site in the oxidation state of +3 and thus maintaining the high activity and stability of the Fe^{3+} site during CO_2 electroreduction (Fig. 6(e)). Li et al. proposed a complex metal oxide strategy to efficiently change the N-doping type as pyrrole-N and pyridine-N, respectively, in supported SA Cu catalyst to optimize the performance in transfer hydrogenation of quinoline [124]. The main pyrrole-N increases the activity of SA Cu catalyst by about 2 times compared with pyridine-N, and can produce 1,2,3,4-tetrahydroquinoline. The hydrogenation of quinoline over SA Cu catalyst was achieved with 99% selectivity in

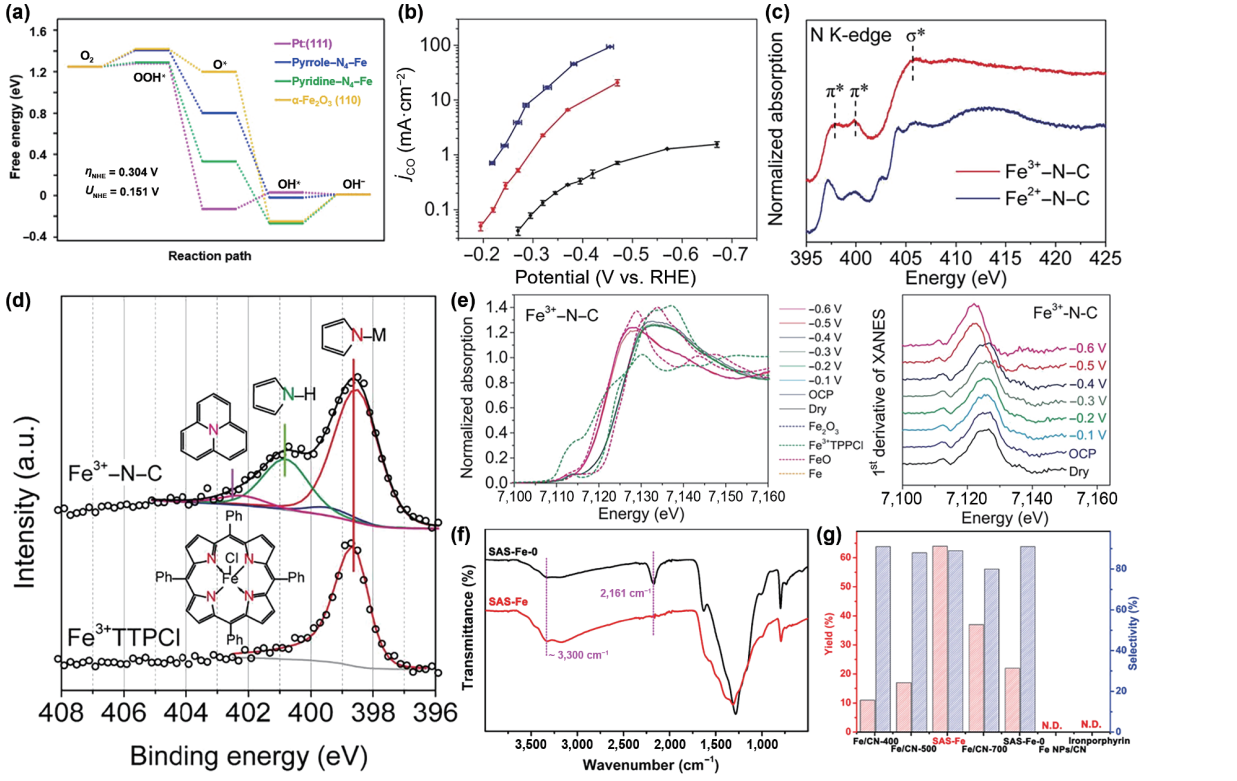

Figure 6 (a) Free energy diagrams for 4e⁻ transfer ORR on Pt (111), pyrrole-N_4–Fe, pyridine-N_4–Fe, and α-Fe_2O_3 (110) at U of 0.151 V under 0.1 M KOH solution. Reproduced with permission from Ref. [120], © Wiley-VCH GmbH 2021. (b) j_{CO} of Fe^{3+}–N–C in an H-cell (red) and on a GDE (blue), and of Fe^{2+}–N–C in an H-cell (black). (c) N K-edge XANES spectra of Fe^{3+}–N–C (red) and Fe^{2+}–N–C (blue). The dashed vertical lines indicate the energy of π^* and σ^* features of a reported metal porphyrin derivative (2,8,12,18-tetraethyl-5,15-diethynyl-3,7,13,17-tetramethylporphyrinatozinc(II)). (d) N 1s XPS spectra of Fe^{2+}–N–C, ferroin sulfate ($Fe^{2+}(phen)_3SO_4$), and ferric-phenanthroline bis(trifluoromethylsulfonyl)imide ($Fe^{3+}(phen)_3(Tf_2N)_3$). Red, blue, green, pink, and cyan peaks are assigned to uncoordinated pyridinic N, pyridinic N coordinated to metals, protonated pyridinic N, graphitic N, and oxidized N, respectively. (e) Fe K-edge XANES spectra (left) and the first derivative of the spectra (right) of Fe^{3+}–N–C loaded on glassy carbon electrodes at open circuit potential (OCP) (blue), −0.1 V (light blue), −0.2 V (green), −0.3 V (dark green), −0.4 V (dark blue), −0.5 V (red), and −0.6 V (pink) versus RHE, with the spectra of Fe_2O_3 (blue dashed), Fe^{3+}TPPCl (green dashed), FeO (pink dashed), and Fe foil (orange dashed) as references. Reproduced with permission from Ref. [123], © Gu, J. et al. 2019. (f) FT-IR spectra of SAS-Fe and SAS-Fe-0. (g) The catalytic performance of different catalysts. Reproduced with permission from Ref. [74], © WILEY-VCH Verlag GmbH & Co. KGaA, Weinheim 2020.

mild conditions (60 °C, 2 h) using ammonia-borane as hydrogen source through controlled pyrrole-N coordination. The presence type of nitrogen is related to the pH of the composite metal oxides. In addition, Sun et al. used three carbon nanotubes with different N types as carbon supports for single atomic layer deposition (ALD) of platinum [125]. The ratio of pyrrole N to pyridine N in high N-content CNT (HNCNT) is close to 1:1, but only about 1:3 in NCNT. These results indicate that pyrrole N is widely present in HNCNT structures. With the increase of pyrrole N content in the carbon nanotube support, the HER activity of Pt catalyst also increased. First-principles calculations show that the d_{yz} orbital and s orbital of H interact with sp^3 hybrid orbital of N under the induction of H adsorption orbital, resulting in high HER activity.

In addition to directly regulating the types of coordination N atoms, the electronegativity of coordination N atoms can be changed by regulating the properties of the groups on the support, thus affecting the valence states of the active metal centers. Wang et al. investigated the effects of pyrolysis temperature (Fe/CN-400, Fe/CN-500, and Fe/CN-700) and reduction treatment on single atom dispersion or aggregation [74]. Interestingly, after reduction in H_2/Ar atmosphere, SAS-Fe exhibits a higher oxidation state. Fourier transform infrared spectroscopy (FT-IR) (Fig. 6(f)) showed that the characteristic peak of cyan group (2,161 cm^{-1}) disappeared and the intensity of amine group (3,300 cm^{-1}) increased, indicating that the cyan group was reduced to amine group. This transition affects the electronegativity of coordination nitrogen and further increases the Fe oxidation state. When the pyrolysis temperature is increased to 700 °C, Fe nanoparticles inside the carbon nanotubes can be seen. As shown in Fig. 6(g), SAS-Fe with pyrolysis temperature of 600 °C had a high yield (64%) within 3 h and excellent selectivity (89%) for styrene oxide, indicating excellent catalytic performance of SAS-Fe in styrene oxidation. SAS-Fe-0, Fe/CN-400, Fe/CN-500, and Fe/CN-700 showed low performance, indicating that the appropriate oxidation state is the key factor of the reaction.

2.2.2 *Direct coordination of heteroatoms*

The standard symmetric plane four-coordination structure may be the most favorable catalytic site for M–N_4 catalysts, but some recent studies have also indicated that the greater electronegativity of adjacent symmetric nitrogen atoms around the metal site can lead to the large Gibbs free energy of the reaction and slow down the kinetic process [126, 127]. It is obvious that non-optimal adsorption of intermediates seriously reduces the kinetics and hinders the improvement of performance. Fortunately, the substitution of N atom in M–N_4 with other less electronegative atoms with larger atomic radius, such as P and S, is a hopeful strategy to optimize the coordination environment of the active site and improve the catalytic performance [27]. Doped atoms can also break the symmetry of the active site, providing more possibilities for improving catalytic performance.

P and N belong to the same group, but P is less electronegative than N, resulting in the adjustment of electronic structure of P coordination metal atoms [128]. Wang et al. prepared Co-SA/P-*in situ* through a combination of wet chemistry and pyrolysis by *in situ* phosphating process (Figs. 7(a)–7(c)) [129]. At the current density of 10 mA·cm^{-2}, Co-SA/P-*in situ* site showed the best activity, requiring an overpotential of only 98 mV, much lower

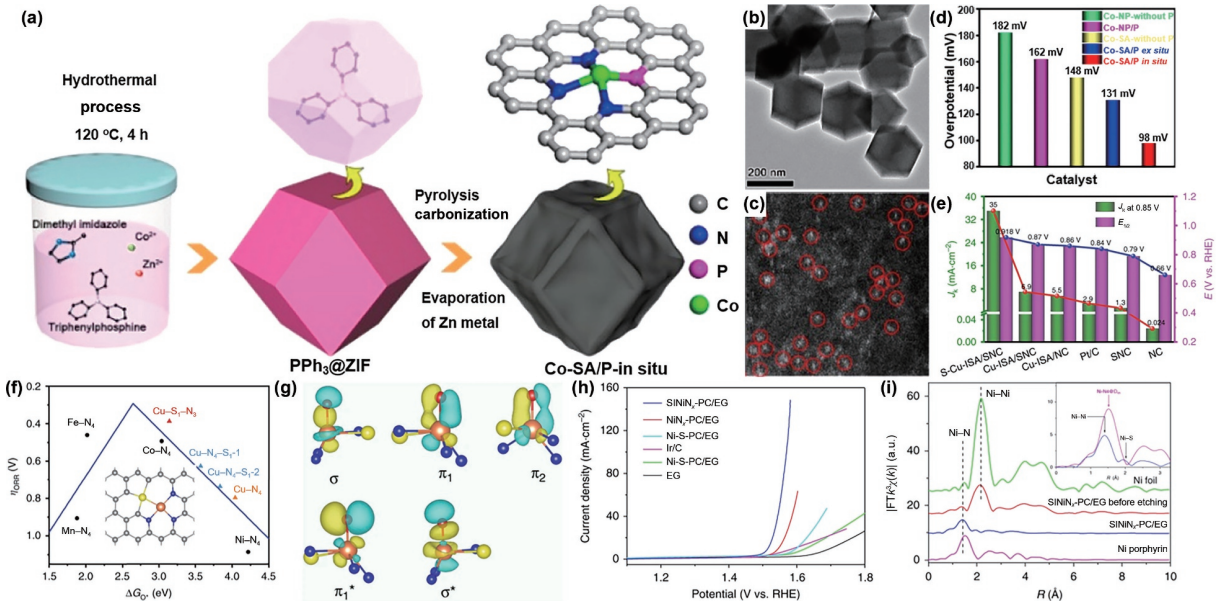

Figure 7 (a) Scheme of the formation of Co-SA/P-*in situ*. (b) TEM characterizations of Co-SA/P-*in situ*. (c) Aberration-corrected STEM image of Co-SA/P-*in situ*. (d) Overpotentials of Co-SA/P-*in situ* and other compared catalysts. Reproduced with permission from Ref. [129], © American Chemical Society 2020. (e) The contrast between S–Cu-ISA/SNC and the references for J_k (0.85 V) and $E_{1/2}$. (f) ORR overpotential (η_{ORR}) as a function of O* adsorption free energy (ΔG_{O^*}) on different Cu-centered moieties. Gray, blue, orange and yellow balls represent C, N, Cu and S atoms, respectively. (g) Molecular orbitals of O* adsorbed on Cu–S_1N_3 in S–Cu-ISA/SNC. Reproduced with permission from Ref. [134], © Shang, H. S., et al. 2020. (h) Polarization curves of EG, NiN_x–PC/EG, Ni–S–PC/EG, N–S–PC/EG, S|NiN_x–PC/EG, and Ir/C for OER. (i) Ni K-edge k^3-weighted EXAFS spectrum of S|NiN_x–PC/EG; data for the Ni foil, NiO, Ni porphyrin, and S|NiN_x–PC/EG before etching are also shown. Reproduced with permission from Ref. [135], © Hou, Y., et al. 2019.

than Co-SA/P-*ex situ* (131 mV), Co-SA-without P (148 mV), Co-NP/P (162 mV), and Co-NP-without P (182 mV) (Fig. 7(d)). The Tafel slope of Co-SA/P-*in situ* was 47 mV·dec^{-1}, which was significantly smaller than other control samples. Co_1N_4 and $Co_1P_1N_3$ models were established to study the synergistic effect of N and P. The ΔG_H* value of $Co_1P_1N_3$ is 0.022 eV, which is lower than that of Co_1N_4 (0.306 eV). When Co is stabilized by both P and N, more charge depletion occurs on P, while more charge accumulation occurs on the surrounding carbon. This charge transfer plays an important role in improving the electrochemical activity of catalysts. Furthermore, P species play a key role in facilitating electron tunneling from the substrate to the enzyme active center. Li et al. used P as precursor to anchor metal active center and adjust local coordination structure in the synthetic system [69]. The designed FeN_3P-SAzyme has good geometric and electronic structure, and exhibits catalytic performance corresponding with Michaelis–Menten kinetics. Compared with the most widely used Fe_3O_4 nano-enzyme or FeN_4-SAzyme without P coordination, FeN_3P-SAzyme had higher catalytic activity. FeN_3P-SAzyme had a specific activity of 316 U·mg^{-1}, more than 30 times higher than that of Fe_3O_4 nano-enzyme, and nearly 10 times higher than that of FeN_4-SAzyme. The catalytic efficiency and selectivity of FeN_3P-SAzyme against peroxidase substrate 3,3′ ,5,5′ -tetramethylbenzidine (TMB) were equivalent to the natural horseradish peroxidase (HRP) enzyme. According to DFT calculation, FeN_3P-SAzyme has a higher catalytic activity since the potential barrier for O and OH formation is lower (< 0.5 eV), while FeN_4-SAzyme is difficult to complete the catalytic process under acidic conditions. For FeN_4-SAzyme, the surface OH species has difficulty to convert into H_2O molecules (1.05 eV), so it will inhibit the entire catalytic process by sticking to the active center of Fe atoms. In addition, Zhang et al. developed a template-free method to construct cross-linked polyphosphazene nanospheres with tunable hollow structures [130]. The uniform dispersion of the N and P coordination single-atom site ($Co–N_2P_2$) was confirmed by structural characterization. Electrochemical measurements and theoretical simulations reveal the ORR performance. Chen et al. developed Fe–N/P–C active sites on carbon nanosheets for ORR [38]. Fe–N/P–C-700 showed the maximum diffusion-limiting current density (J_L = 5.66 mA·cm^{-2}), the maximum positive onset potential (E_{onset} = 0.941 V), and the maximum half-wave potential ($E_{1/2}$ = 0.867 V).

Due to its low electronegativity, S doping seems to be an attractive method to adjust the electronic structure of the active site and achieve improved catalytic performance [131–133]. Zhang et al. proposed a practical strategy for the rational design of multilayer porous carbon derived from a metal-organic framework (MOF) in which single Cu atoms coordinate with S and N atoms (S–Cu-ISA/SNC) [134]. The atomic interface configuration of the copper site in S–Cu-ISA/SNC was found to be asymmetric Cu–S_1N_3 by *in situ* X-ray absorption fine structure test. From 1.05 to 0.75 V, the valence state of Cu in S–Cu-ISA/SNC decreased during ORR. The average oxidation state of Cu species decreased from about +2 to +1, suggesting that Cu (+1) site may be the active center of ORR. When the applied potential was restored from 0.75 to 1.05 V, the Cu XANES edge moved back to higher energy with the increase of the white line peak. The reversible change of Cu valence state reflected its significant contribution to the catalytic activity of ORR. In addition, the low-price Cu–N bond shrank during ORR. As shown in Fig. 7(e), the catalyst had good oxygen reduction activity and half-wave potential is 0.918 V. According to Sabatier's principle (Fig. 7(f)), the best catalyst, located at the apex of a volcanic region, is neither too strongly nor too weakly bound to the reaction intermediates. Due to the introduction of coordination S, the Cu atom in the Cu–S_1N_3 site has more electrons occupying the d_{x2-y2} orbital than the Cu–N_4 site (Fig. 7(g)). The π bond formed by Cu d_{x2-y2} orbital enhances the weak bonding ability of ORR intermediates, thus improving the ORR performance of Cu centers. Because of the asymmetric Cu–S_1N_3 site, the O* intermediate of ORR is not completely on top of the Cu atom, so the O p orbital can interact with the Cu d_{x2-y2} orbital. For the symmetric Cu–N_4 site, the O* intermediate of ORR is located at the top of Cu due to symmetry limitation, and there is no interaction between O p orbital and Cu

d_{x2-y2} orbital. In addition, Feng et al. reported atomically dispersed Ni with N and S species on porous carbon nanosheets as electrocatalysts, showing excellent OER activity and durability [135]. As shown in Fig. 7(h), in alkaline medium, the onset potential of S|NiN_x–PC/EG was 1.50 V, which was better than that of NiN_x–PC/EG (1.53 V). XANES spectra show that compared with the reference Ni porphyrin, the FT peak of S|NiN_x–PC/EG can be attributed to Ni–N and Ni–S, with the bond length of 1.85 and 2.33 Å, respectively (Fig. 7(i)). Using EXAFS fitting, the coordination numbers of Ni–N and Ni–S in S|NiN_x–PC/EG are 2.8 and 0.8, respectively. In the D_{4h} local structure, the larger S replaces one N, resulting in the shortening of the Ni–N bond length and slight local deformation of the ideal square planar symmetric structure. The results showed that the energy barrier of the third step is significantly lower. Because of the presence of the hybrid state of the adjacent C atom and Ni atom, the presence of S atoms gives it a high positive charge density, and optimizes the state density distribution, thus enhancing the electronic transfer ability in the Ni–N_3S model.

P and S co-doped active sites have also been reported. Under the guidance of DFT calculation, as shown in Fig. 8(a), Wang et al. designed and synthesized MOFs derived single-atom Co catalysts supported by hollow carbon polyhedron (Co_1–N_3PS/HC) with the best active part of Co_1–N_3PS [136]. Different single-atom Co structure models were constructed and optimized by DFT simulation in order to study the relationship between four-electron ORR reaction energetics and coordination structure-induced electron density. Among them, CoN_3PS@PS model has the best ORR performance. The prepared Co_1–N_3PS/HC has good alkaline ORR performance, and the half-wave potential is 0.920 V. In addition, the kinetic current density (J_k) of Co_1–N_3PS/HC catalyst at 0.900 V is 28.0 mA·cm^{-2}, and the Tafel slope is 31 mV·dec^{-1}. The best Co_1–N_3PS/HC fitting results clearly show that the main peak at 1.4 Å and a shoulder peak at 1.8 Å can be attributed to the superposition of first-shell Co–N, Co–P, and Co–S coordination. The coordination numbers of N, P, and S are 3.1, 0.9, and 1.1, respectively, and the average bond lengths are 1.97, 2.32, and 2.34 Å, respectively, indicating that the compound is a single atom site of Co_1–N_3PS. The coordination number and average bond length of the synthesized Co_1–N_3PS/HC are in keep with the DFT model of CoN_3PS@PS, indicating that the best active part of Co_1–N_3PS is obtained.

In contrast, the electronegativity of B is significantly reduced. Active sites coordinated with electron-deficient B can carry different charge and break the electrical neutrality of the matrix [137]. Mu et al. used the soft-template self-assembly pyrolysis method to obtain the B-doped Co–N–C active site confined in hierarchical porous carbon sheets (Co–N,B–CSs) (Figs. 8(b)–8(d)) [138]. The half-wave potential of the catalyst was 0.83 V, and the limiting current density was about 5.66 mA·cm^{-2}, which had higher durability than Pt/C catalyst. The Co oxidation state in Co–N,B–CSs is lower because its edge transition energy is lower than that of Co–N–Carbon. The density of unoccupied states in Co–N,B–CSs is less than that in Co–N–Carbon due to the electron donor properties of B. Since positive polarization of C atoms can be induced by N atoms, while low electronegativity B atoms can be positively polarized, the adsorption of O_2 molecules in the O_2 reaction process can be promoted by the positively polarized N–C and C–B bonds, which thus improves the ORR and OER performance. Co–N,B–CSs show downtrend in each step of ORR process when the potential is 0.24 V, which is significantly lower than Co–N_4–CSs (0.48 V).

However, O is more electronegative, capturing more electrons from the central metal atom than N, thus modulating catalytic selectivity. By adjusting the coordination environment of the catalytic center, the ORR path at the atomically dispersed Zn site can be flexibly changed to highly selective ORR [70]. Atomically dispersed Zn catalysts with unique O and C coordination

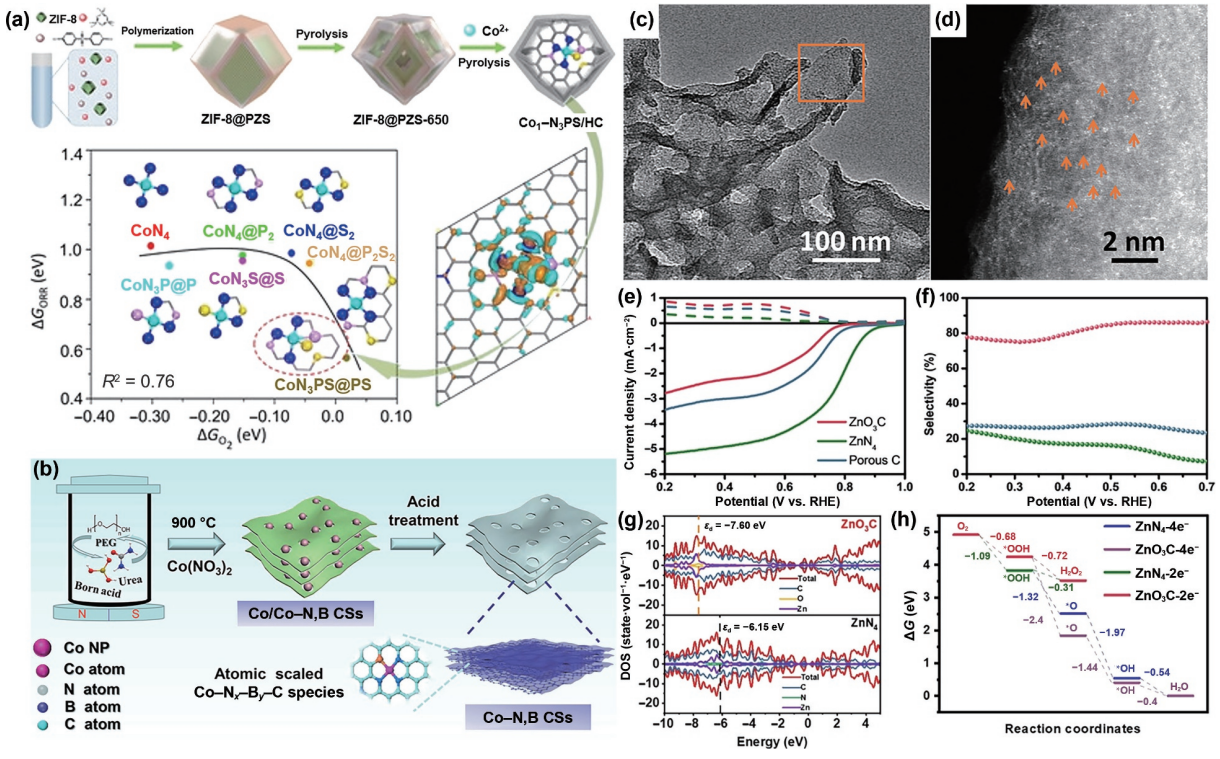

Figure 8 (a) Scheme of the synthesis and the charge density difference of Co atom of Co_1–N_3PS/HC and the linear relationship for ORR activity as a function of the O_2* adsorption energy at U_{RHE} = 1.23 V. Reproduced with permission from Ref. [136], © Wiley-VCH GmbH 2020. (b) Synthetic procedure of the Co/N–B-doped carbon nanosheet (Co–N,B–CSs). (c) TEM and (d) HAADF-STEM images for Co–N,B–CSs. Reproduced with permission from Ref. [138], © American Chemical Society 2018. (e) LSV curves and (f) selectivity of ZnO_3C and ZnN_4 in 0.1 M KOH. (g) Calculated DOS of ZnN_4 and ZnO_3C; the d-band center is marked with the black dotted line. (h) Free energy diagram of 2e$^-$ and 4e$^-$ ORR on ZnO_3C and ZnN_4 at 0 V. Reproduced with permission from Ref. [70], © Wiley-VCH GmbH 2021.

structures (ZnO_3C) or N coordination structures (ZnN_4) can be prepared by changing the functional groups of the precursors. ZnN_4 catalyst generates H_2O through the 4e ORR pathway. However, in 0.1 M KOH, ZnO_3C catalyst can regulate the coordination environment of Zn atoms and generate H_2O_2 through 2e ORR pathway, with an overpotential close to zero and high selectivity (Figs. 8(e) and 8(f)). Compared with ZnN_4, the d-band center of ZnO_3C descends and shifts away from the Fermi level (Fig. 8(g)). H_2O_2 is produced by the hydrogenation of *OOH and H_2O by the dissociation of *O–OH. At 0 V, the ΔG_{*OOH} of ZnO_3C is 4.24 eV, which is located near the volcanic peak of 2e ORR, indicating that OOH* adsorbed on ZnO_3C is preferentially hydrogenated to H_2O_2 rather than dissociated (Fig. 8(h)). This is because the adsorption strength of ZnO_3C for OOH* is significantly reduced, which inhibits the dissociation of OOH* from O*. In addition, Zhou et al. prepared Ta catalysts for nitrogen reduction reaction (NRR) by photodeposition method (Ta–GO) and impregnation method (Ta–NC), respectively [139]. The ammonia yield of Ta–GO catalyst is 19.97 $\mu g_{NH3} \cdot h^{-1} \cdot mg_{cat.}^{-1}$, and the Faraday efficiency is 8.52%. In contrast, Ta–NC has a lower atomic efficiency (17.71 $\mu g_{NH3} \cdot h^{-1} \cdot mg_{cat.}^{-1}$), but a higher selectivity (FE = 17.86%). Using quantum chemical calculations, the most likely structure for NRR process is Ta–O_6-a. The potential barrier of Ta–GO is low (0.83 eV). The barrier of Ta–O_6-a center for HER process (0.89 eV) is slightly higher than that for NRR process. However, the HER process is entropically more advantageous than the NRR, and therefore more competitive. Compared with the NRR reaction at Ta–O_6-a, the reaction energy at Ta–N_6-a is poor, which is manifested by a higher potential barrier formed by the initial N–H bond (0.97 eV) and a higher energy required for nitrogen adsorption. However, on the other hand, there is a higher NRR selectivity at Ta–N_6-a due to the higher barrier (2.43 eV) of HER process at Ta–N_6-a. In addition, Wang et al. reported that the coordination structure of single-atom Pt active center significantly affects its performance in anti-Markovnikov hydroboration of alkenes [140]. The catalytic activity of Pt single-atom catalyst with three O atoms (Pt–O_3) is higher, and the conversion number of the hydroboration reaction to alkylboronic esters can reach 3,288, superior to the other two coordination structures (Pt–N_4 and Pt–O_2).

2.2.3 *High-shell coordination of heteroatoms*

Heteroatoms with different electronegativity on the support can also adjust the electronic properties of the directly coordinated atoms and the metal atom through the long-range interaction to improve the performance [132, 141]. Although the modification of activity by doping in this case is indirect and limited, heteroatoms of this regulatory type regulate and enhance their kinetic activity by regulating the electron-attracting/electron-donating properties of the M–N_4 site [142, 143]. Thus, such high shell doping may allow for finer and more precise regulation of the electronic structure.

The presence of P may alter the electronic structure of the single metal site through its 3p lone pair electrons, thus adjusting its electrochemical activity. Li et al. developed a new synthesis strategy by constructing bimetallic organic framework (BMOFs) and polymer core–shell composition, and prepared single-atom Co catalyst, with Co atoms dispersed on nitrogen and phosphorus co-doped carbon (Co_1/P–NC) [144]. On the EXAFS FT curve of Co_1/P–NC, only one peak at 1.5 Å is detected, which is attributed to Co–N coordination. From FT curve, Co_1/P–NC catalyst does not show higher shell peak near 2.0 Å, which confirmed that Co_1/P–NC catalyst does not have Co–P contribution. Co_1/P–NC catalyst had a 99% conversion rate and 99% selectivity for the selective oxidation of benzyl alcohol due to the high reactivity of single atom and modification of support. In addition, Wang et al. introduced single P atoms into nitrogen-doped carbon supported single Fe atom catalyst mainly in the form of P–C bond (Fe-SAC/NPC) for CO_2 reduction to CO [145]. Interestingly, the oxidation degree of Fe-SAC/NPC was lower than that of Fe-SAC/NC, suggesting that the presence of P reduced the oxidation state of Fe in Fe-SAC/NPC. The catalyst has a FE_{CO} of 97% at overpotential of 320 mV and a Tafel slope of only 59 $mV \cdot dec^{-1}$, comparable with the most advanced catalysts. In the O adsorption condition, compared with FeN_4O, the contribution of electron density near Fermi level of FeN_4OCP_3 from Fe center is more significant. Therefore, enhanced electron interaction increases the adsorption energy of *COOH at FeN_4OCP_3 site, resulting in a lower energy barrier for the formation of *COOH intermediates. The ΔG required to generate *COOH on FeN_4O is 0.53 eV, while for FeN_4OCP_3, FeN_4OCP_4, and FeN_4OCP_5, it is 0.32, 0.47, and 0.46 eV, respectively. In addition, Zhang et al. added P to rich edge FeN_4 loaded on N, P-doped carbon (Fe–N–C–P/N,P–C) [146]. A strong peak belonging to Fe–N interaction at 1.50 Å can be seen in the FT-EXAFS spectra of Fe–N–C–P/N,P–C (Fig. 9(a)), forming the structure of four N atoms surround the Fe atom. Fe atoms in Fe–N–C–P/N,P–C coordinate with four N atoms by two nearest neighbor bonds as shown in the EXAFS fitting curve (Fig. 9(b)). In the formation process of Fe–N–C at carbon edges, the P atoms would take priority of replacing the partial C atom at the edge next to the hole to form the stable FeN_4P_2-(2,4)-DC structure. As shown in Fig. 9(c), the prepared catalyst showed significantly improved acidic ORR activity with a half-wave potential of 0.80 V.

The larger atomic radius of S may lead to defects on the carbon supports, while the lower electronegativity of S may change the electronic structure of the active center. Li et al. proposed an atom interface strategy to construct a single atom copper catalyst (Cu-SA/SNC), which exhibited strong ORR activity in alkaline medium with a half-wave potential of 0.893 V [37]. In addition, XAFS studies based on synchrotron radiation (Fig. 9(d)) and DFT calculations show that the isolated bond-contraction low-valence Cu (+1)–N_4–C_8S_2 atom interface site is the active site during ORR. In the S L-edge XANES spectrum of Cu-SA/SNC (Fig. 9(e)), the peaks in the shadows represent the formation of C–S–C coordination. At the same time, compared with the spectra of CuS and Cu foils, no peak from Cu–S and Cu–Cu coordination was observed (Fig. 9(f)). This means that Cu atoms are connected by four N atoms in the first coordination layer with a bond length of 1.95 Å and no Cu–S bonds (Fig. 9(g)). The Cu species in Cu-SA/NC are present in the formation of Cu–N_4C_{10} without S, but the bond length of Cu–N (2.00 Å) is longer than that of Cu–$N_4C_8S_2$. The charge density difference and Mulliken charge analysis show that S doping can effectively regulate the charge of Cu through the atomic interface and reduce the positive charge of Cu in Cu-SA/SNC, resulting in a better ORR performance. In addition, a novel pyrrole thiophene co-polymer was designed for the synthesis of Fe isolated single atoms on sulfur-nitrogen co-doped carbon (Fe-ISA/SNC) by pyrolysis under controlled S and N doping (Figs. 9(h) and 9(i)) [147]. FT-EXAFS of Fe-ISA/SNC have only one main peak at about 1.5 Å, which is due to the scattering of Fe–N. As shown in Fig. 9(j), the fitting curves show that Fe atoms coordinate with four N atoms in Fe-ISA/SNC, but the four Fe–N bonds differentiate into two groups of Fe–N bond lengths, one with 1.86 Å and the other with 1.97 Å. The Fe-ISA/NC samples without S doping only show one group of Fe–N bonding length. The catalytic efficiency of Fe-ISA/SNC shows a volcanic curve with the increase of sulfur doping amount. The half-wave potential of optimized Fe-ISA/SNC was 0.896 V, which was higher than that of Fe-ISA/NC (0.839 V). As shown in Fig. 9(k),

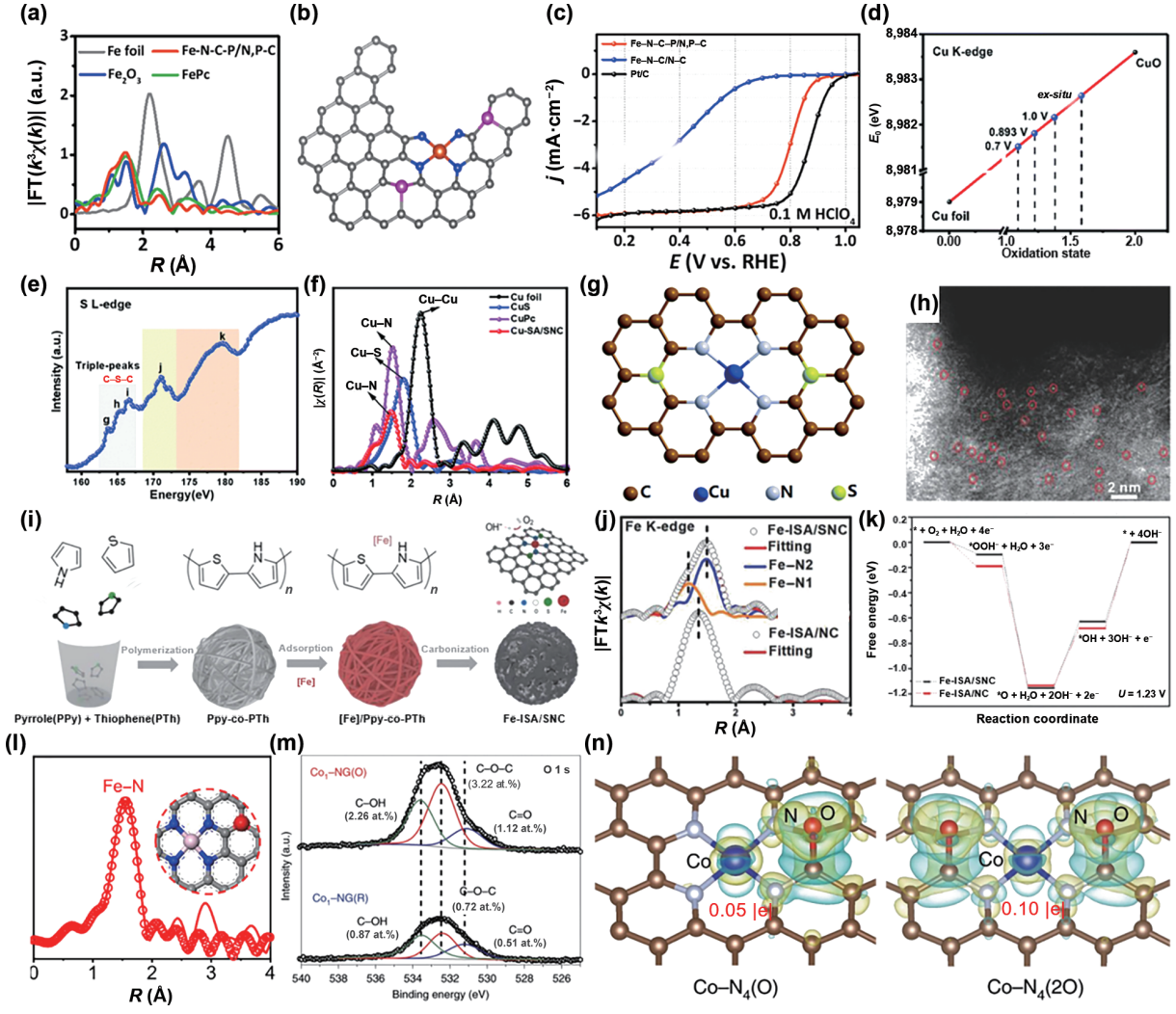

Figure 9 (a) FT-EXAFS curves at the Fe K-edge of Fe–N–C–P/N,P–C and reference materials. (b) Structure of Fe–N–C–P/N,P–C. (c) LSV curves of ORR in O_2-saturated 0.1 M $HClO_4$ at 1,600 rpm for Fe–N–C–P/N,P–C, Fe–N–C/N–C and Pt/C. Reproduced with permission from Ref. [146], © American Chemical Society 2021. (d) The average oxidation states of Cu from XANES spectra. (e) S L-edge XANES spectrum of the Cu-SA/SNC. (f) The *ex situ* FT k^3-weighted Cu K-edge EXAFS spectra of Cu-SA/SNC and references. (g) Schematic interfacial model of Cu-SA/SNC. Reproduced with permission from Ref. [37], © The Royal Society of Chemistry 2019. (h) HAADF-STEM image of the Fe-ISA/SNC. Single Fe atoms highlighted by red circles. (i) Illustration of the synthetic process of Fe-ISA/SNC. (j) Comparison of the quantitative EXAFS fittings between Fe-ISA/SNC and Fe-ISA/NC. (k) Fe energy diagram for the Fe-ISA/SNC and Fe-ISA/NC systems during the ORR under alkaline conditions at and equilibrium potential of U = 1.23 V. Reproduced with permission from Ref. [147], © WILEY-VCH Verlag GmbH & Co. KGaA, Weinheim 2018. (l) Fourier transformed EXAFS spectra (lines) of the FeNC+B sample and the corresponding simulation curves (circles) on the basis of models (insets), k = 1. Reproduced with permission from Ref. [151], © Tsinghua University Press and Springer-Verlag GmbH Germany 2020. (m) Deconvoluted oxygen 1*s* spectra of Co_1–NG(O) and Co_1–NG(R). (n) Differential charge densities of Co–N_4/graphene after O* or 2O* was adsorbed near the cobalt atom. Yellow and cyan isosurfaces (±0.003 $Bohr^{-3}$) show the electron gain and electron loss, respectively. Reproduced with permission from Ref. [152], © Jung, E., et al. 2020.

the final step of ORR (*OH reduction) is the most endothermic and is the RDS for both catalysts. Compared with Fe-ISA/NC, the ORR overpotential on Fe-ISA/SNC decreased by 0.05 V. This may be due to the negative charge induced by S on N repelling *OH, thus promoting the reduction release of *OH. Chen et al. proposed a strategy for the synthesis of single atom Fe on N and S co-doped hierarchical porous carbon (Fe_1/N,S–PC) based on coordination polymers [148]. The half-wave potential of Fe_1/N,S–PC (0.904 V) was better than that of commercial Pt/C (0.86 V), Fe_1/N–PC without S-doped (0.85 V), and other non-noble metal catalysts in alkaline media. When N and S are co-doped into the carbon structure, Fe_1/N,S–PC showed a higher d-band than pure graphite powder, indicating that there are a lot of defects in these porous carbon structures. Lv et al. synthesized a flexible independent carbon fiber film and fixed it on atomically dispersed Fe–N_4/C catalyst (Fe/SNCFS–NH_3) as the air cathode of Zn–air batteries [149]. The modification of local atomic configurations in Fe/SNCFs–NH_3 catalyst by S doping results in excellent ORR and enhanced OER activity. The catalyst designed by Wang et al. is composed of a single Fe atom site and supported by a hollow carbon polyhedron (Fe-SAS/NPS–HC) co-doped with N, P, and S, showing excellent ORR performance in alkaline media [150]. The high efficiency and satisfactory kinetics of Fe-SAS/NPS–HC are attributed to the dispersion of N-coordination Fe atoms and the electronic effects of surrounding S and P atoms. It can contribute electrons to the single-atom Fe center and reduce the positive charge of Fe, thus weakening the binding of adsorptive OH species.

The coordination type of B dopant plays a key role in regulating the catalytic activity and selectivity of Fe sites. Li et al. studied a novel catalyst composed of Fe–N_4 centers and uncoordinated B heteroatoms (FeNC+B) [151]. The Fourier transform EXAFS of FeNC+B (Fig. 9(l)) is similar to that of bare FeNC, and there is a strong Fe–N peak at 1.45 Å, which is in good agreement with the fitting results of Fe–N_4 structure simulation model. FeBNC samples with a higher concentration of B exhibit a new EXAFS peak at 1.7 Å, which is attributed to the Fe–B bond and confirmed by simulations based on the FeB_1N_3 model. Benzylamine can be

completely converted to benzonitrile under fixed conditions by FeNC+B samples with considerable surface area and uncoordinated B doping. The yield of benzonitrile in FeBNC sample was only 26.5% after the reverse conversion of benzonitrile to imine on FeBNC samples. In the FeNC+B model, the ΔG of the two dehydrogenation paths is slightly reduced compared with that of the undoped FeNC model. The process of dehydrogenation to nitrile is performed automatically only on FeNC+B model, which well explained the ultra-high selectivity of true FeNC+B catalyst to benzonitrile. In contrast, in the FeBNC model, the direct coordination between the B atom and the Fe site makes the imine more favorable on the coupling path.

The more electronegative O can increase the oxidation state of the central metal atom by long-range effect. Hyeon et al. designed and synthesized a single-atom electrocatalyst that included an optimized Co–N_4 site and added it to nitrogen-doped graphene for the production of H_2O_2 [152]. The catalytic performance of Co–N_4 can be adjusted by fine-tuning the configuration of the surrounding atoms. The optimal kinetic current density is 2.8 mA·cm^{-2} at 0.65 V, and the mass activity is 155 A·g^{-1}. The activity loss is negligible within 110 h. O K-edge near-edge X-ray absorption fine structure spectra (Fig. 9(m)) show that Co_1–NG(O) SAC has stronger and sharper peaks at 535 and 540.4 eV, which can be designated as the transition from the O 1s core level of the carbon–oxygen bond to the antibonding π* and σ* states. The comprehensive analysis of XPS, XAFS, and FT-IR shows that the Co center has relatively few electrons when it is close to the C–O–C structure. When O* absorbs in the vicinity of Co–N_4 (Co–N_4(O)), G_{OOH^*} increases from 3.9 to 4.1 eV, which is very close to the optimal value of H_2O_2 generation. When two O* adsorb near Co–N_4(Co–N_4(2O)), The G_{OOH^*} can be further increased to 4.5 eV. As shown in Fig. 9(n), in the case of Co–N_4(O) and Co–N_4(2O), the positive charge states of Co atoms increase by 0.05 e$^-$ and 0.10 e$^-$, respectively.

2.2.4 *Axial coordination of heteroatoms*

Cl atoms with axial coordination can also regulate the activity of metal sites. Wang et al. designed and synthesized the Zn/Fe bimetallic metal-triazolate framework as the precursor and prepared SACs (Fig. 10(a)) [108]. Fe single atoms were dispersed in a layered porous N-doped carbon matrix with high metal loading (2.78 wt.%) and FeN_4Cl_1 configuration with mesoporous (FeN_4Cl_1/NC). In 0.1 M KOH and 0.1 M $HClO_4$, its ORR activity was 0.91 and 0.79 V, respectively, superior to most reported MOF-derived SACs. As shown in Fig. 10(b), DFT calculation confirms that for FeN_4/NC, the last step of electron transfer is endothermic, ΔG is 0.30 eV, indicating that FeN_4 has a strong adsorption on *OH, limiting the desorption rate of *OH. However, for FeN_4Cl_1/NC, all electron transfer steps are downhill, indicating that Cl coordination helps to optimize the adsorption energy with *OH, so as to achieve a more favorable thermodynamic ORR process. The axial electron transfer of Fe and Cl will affect the charge of Fe in FeN_4Cl_1/NC, leading to the weakening of the binding strength of Fe and OH*. In addition, by adjusting the short-range coordination environment and the long-range interaction with the heteroatoms in the active center, the electronic structure of the active center can be changed simultaneously, and the catalytic performance can be significantly improved. Li et al. prepared atomically dispersed $FeCl_1N_4$/CNS catalysts by thermal transfer method for ORR [107]. The FT-EXAFS spectra of $FeCl_1N_4$/CNS only have a main peak at 1.66 Å, which is considered to correspond to the first coordination shell of Fe–N/Cl (Figs. 10(c) and 10(d)). The peak shows a slight migration compared to FePy (1.52 Å), which is related to the coordination of Fe–Cl in $FeCl_1N_4$/CNS. As shown in Fig. 10(e), in 0.1 M KOH solution, its half-wave potential was 0.921 V, which

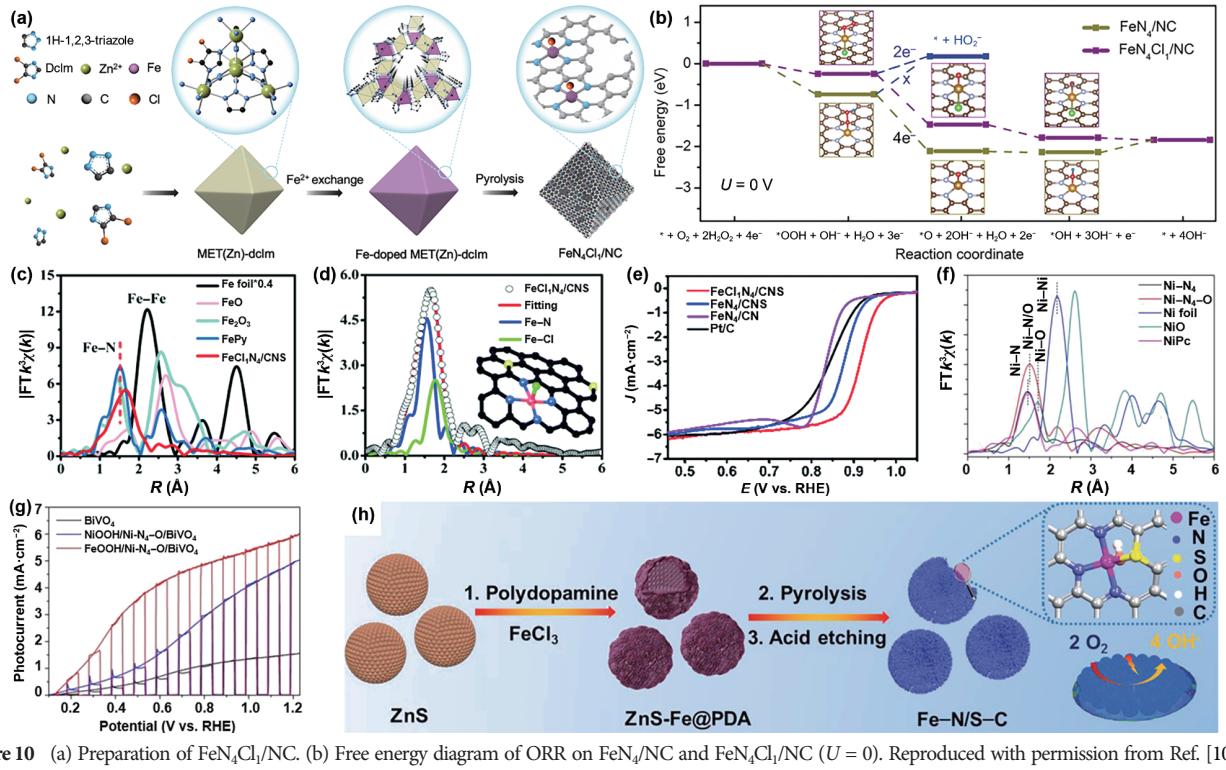

Figure 10 (a) Preparation of FeN_4Cl_1/NC. (b) Free energy diagram of ORR on FeN_4/NC and FeN_4Cl_1/NC (U = 0). Reproduced with permission from Ref. [108], © Wiley-VCH GmbH 2021. (c) Fourier transform at the Fe K-edge of the $FeCl_1N_4$/CNS, FePy, FeO, Fe_2O_3 sample, and Fe foil. (d) The corresponding EXAFS fitting curves of the $FeCl_1N_4$/CNS in R space. Inset: Schematic model of $FeCl_1N_4$/CNS: Fe (red), Cl (green), S (yellow), N (blue), and C (gray). (e) ORR polarization curves in O_2-saturated 0.1 M KOH. Reproduced with permission from Ref. [107], © The Royal Society of Chemistry 2018. (f) Fourier transformed k^3-weighted $\chi(k)$ function of the EXAFS spectra for Ni K-edge. (g) chopped J–V curves of $BiVO_4$, NiOOH/Ni–N_4–O/$BiVO_4$, FeOOH/Ni–N_4–O/$BiVO_4$ photoanodes. Reproduced with permission from Ref. [153], © American Chemical Society 2021. (h) Schematic illustration of the overall synthetic procedure for Fe–N/S–C sample. Reproduced with permission from Ref. [155], © Wiley-VCH GmbH 2021.

was 79 mV higher than that of commercial Pt/C (0.842 V). DFT calculation shows that the overpotential of $FeCl_1N_4$/CNS (0.44 V) was much lower than FeN_4/CN, indicating that $FeCl_1N_4$/CNS had the highest ORR activity. The analysis of state density also shows that the d-bands of FeN_4/CN and FeN_4/CNS are relatively narrow, and the occupied states are closer to the Fermi level, resulting in higher binding energy of O_2. FeO_1N_4/CN has the widest d-band, resulting in the weakest binding energy of O_2. $FeCl_1N_4$/CNS is moderately charged and exhibits the greatest ORR activity.

Coordination patterns for axial O atoms or OH have also been reported. Hou et al. developed a multifunctional coupling strategy to design atomically dispersed M–N_4 sites (M = Ni, Co, and Fe) with an axial oxygen atom (M–N_4–O) in an oxygen evolution assisted catalyst and $BiVO_4$ photoanode to promote photogenerated electron hole separation, thereby enhancing photoelectrochemical activity [153]. Compared with the main peak of Ni–N_4 at 1.46 Å, the position and intensity of Ni–N/O in Ni–N_4–O change simultaneously (Fig. 10(f)). The main peak center of Ni–N_4–O is between Ni–N (1.46 Å) and Ni–O (1.71 Å), indicating that Ni–N and Ni–O bonds exist at the same time. This advanced OEC/Ni–N_4–O/$BiVO_4$ photoanode exhibited a record high photocurrent density of 6.0 mA·cm^{-2} at a 1.23 V, approximately 3.97 times that of $BiVO_4$, achieving excellent long-term photostability (Fig. 10(g)). Under the equilibrium potential (U = 1.23 V), the η of the surface of the Ni–N_4–O photoanode decreases to 0.4 eV with the transition from *OH to *O of RDS. The potential barriers of *OH (1.57 eV), *O (3.2 eV), and *OOH (4.57 eV) intermediates are reduced. Zhou et al. found that hydroxyl (OH) ligand was the active part that enhanced ORR performance through microkinetic model [154]. Because axial OH coordination regulates the electronic structure of the central atom, ORR occurring on Fe–(OH)N_4 is more favorable for limiting steps than on Fe–N_4. In addition, the axial OH coordination of Fe–N_4 increases the adsorption free energy of anions and reduces the H_2O_2 yield of ORR, thus improving the stability of Fe–NC catalyst. A self-sacrificing strategy was proposed to synthesize asymmetric N,S coordination single-atom Fe with axial pentahydroxy (OH) coordination (Fe–N_3S_1OH) embedded in N,S co-doped porous carbon nanospheres (Fe–N/S–C) (Fig. 10(h)) [155]. The obtained Fe–N/S–C exhibited excellent catalytic ORR activity with a half-wave potential of 0.882 V, which was higher than the reference Pt/C. In addition, theoretical calculations confirm that axial OH can optimize the three-dimensional orbit of the Fe center and enhance the adsorption and activation of O_2 at the Fe site, thus reducing the ORR barrier and accelerating the ORR dynamics.

2.3 Chemical bonds at the active sites

In heterogeneous catalysts, the active metal center is usually surrounded by neighboring atoms, and the catalytic performance of the catalyst is obviously determined by the property of the chemical bonds between the central metal and the neighboring atoms to a large extent. Even if several materials have the same support and loaded metal atoms, their properties may differ greatly due to the different dispersion states of the active site on the support [156]. The length, angle, and polarity of the covalent bond formed by metal atoms and coordination atoms affect the electronic properties of the active site and may break the symmetry of the transition stable structure, thus affecting the molecular adsorption [86, 157]. In addition, compared with flat surfaces, curved surfaces with high curvature tend to produce non-planar bending structures and introduce strain effects, which can adjust the d-band center and change the spin polarization state [158–160]. Single metal atoms can also be fixed more strongly on high curvature supports, thus affecting catalytic activity. Therefore, the strain (compressive or tensile strain) has an important effect on the bond lengths and bond angles of the nanocrystals. Understanding the coordination bonds of single atoms, their electronic states, and their dynamic changes in the reaction condition, is considerable to reveal the precise relationship between structure and functional of SACs [161, 162].

2.3.1 *Bond length*

Changes in local coordination on oxide supports have a strong influence on chemical reactions and can be used to control catalytic performance. Li et al. reported an atomically dispersed Pt as an efficient ethanol gas sensor on a one-dimensional porous γ-Fe_2O_3 nanoparticle composite (Fig. 11(a)) [76]. At 2.5 Å, Pt_1–Fe_2O_3 and Pt_1–Fe_2O_3-ox showed no peak corresponding to Pt–Pt contribution, but a prominent peak corresponding to Pt–O contribution (Fig. 11(b)). The peak position of Pt_1–Fe_2O_3-ox is about 1.6 Å, which is the same as that of the standard sample. However, the position of Pt_1–Fe_2O_3 changes slightly, indicating that the Pt–O bond in Pt_1–Fe_2O_3 is longer than that in Pt_1–Fe_2O_3-ox. The valence state of Pt in sample Pt_1–Fe_2O_3-ox is close to +2, while that in sample Pt_1–Fe_2O_3-ox is close to +4, indicating that the Pt species changes to a higher oxidation state after heat treatment. The results show that only high-valence single-atom Pt sites can effectively improve the adsorption capacity of ethanol by changing the electrical structure of Fe_2O_3 support, thus improving the sensitivity of the sensing process. In addition, single-atom Pt_1/CeO_2 catalysts with asymmetric Pt_1O_4 coordination environment formed by atom trapping (AT) have excellent thermal stability (800 °C), but in highly symmetrical square plane Pt_1O_4 coordination environment, due to the excessive stability of Pt^{2+}, it is not suitable for CO oxidation at low temperature [163]. This excessive stabilization results in a greatly reduced ability of isolated Pt^{2+} to activate gas phase molecules (such as CO and H_2), making them almost inactive for CO oxidation below 200 °C. Wang et al. demonstrated that a highly active and thermally stable Pt_1/CeO_2 catalyst can be obtained by adjusting the local environment of isolated Pt^{2+} through TS synthesis (Fig. 11(c)) [164]. In an inert atmosphere, ultrafast shock waves induced CeO_2 surface reconstruction to form Pt single atoms in asymmetric Pt_1O_4 structure. In the process of CO oxidation, the partially reduced Pt_1O_{4-x} coordination forms active $Pt_1^{\delta+}$ species, and the low temperature activity is greatly enhanced. As shown in Fig. 11(d), at high space velocity of 200 L·g^{-1}·h^{-1}, the temperature when CO conversion reaches 50% decreases by about 140 °C. It is worth noting that the white line strength of Pt_1/CeO_2_TS is slightly lower than that of Pt_1/CeO_2_AT (Fig. 11(e)), indicating that the valence state or coordination symmetry of the Pt^{2+} is slightly reduced. More importantly, a rising edge feature appears above the XANES absorption edge of Pt_1/CeO_2_TS, as demonstrated by a bulge on the first derivative curve. The presence of this rising edge is thought to be associated with a decrease in local coordination symmetry around the Pt site. Three shorter Pt–O_S distances are 1.979 Å and one longer Pt–O_L distance is 2.051 Å.

The local three-dimensional structure of metal sites is highly related to the surface morphology and geometric structure of the supports. The catalytic activity can be mediated by regulating bond lengths at metal sites through strain effects. Wu et al. obtained helical carbon structures with rich high-curvature surfaces by templating helical polypyrrole with self-assembled chiral surfactants, introducing compressive strains on Fe–N_4 matrix [56]. In alkaline medium, the dynamic current density of curved Fe–N_4 site at 0.9 V is 7.922 mA·cm^{-2}, which is 31 times that of planar Fe–N_4 site (Fig. 11(f)). The bent structure results in the Fe–N bond shortening by about 1.5%. As illustrated in Figs. 11(g) and 11(h), The Bader charge of Fe in curved Fe–N_4 (1.13 e) is larger than that in planar Fe–N_4 (1.08 e), showing more obvious charge transfer. In addition, projected density of states (PDOS)

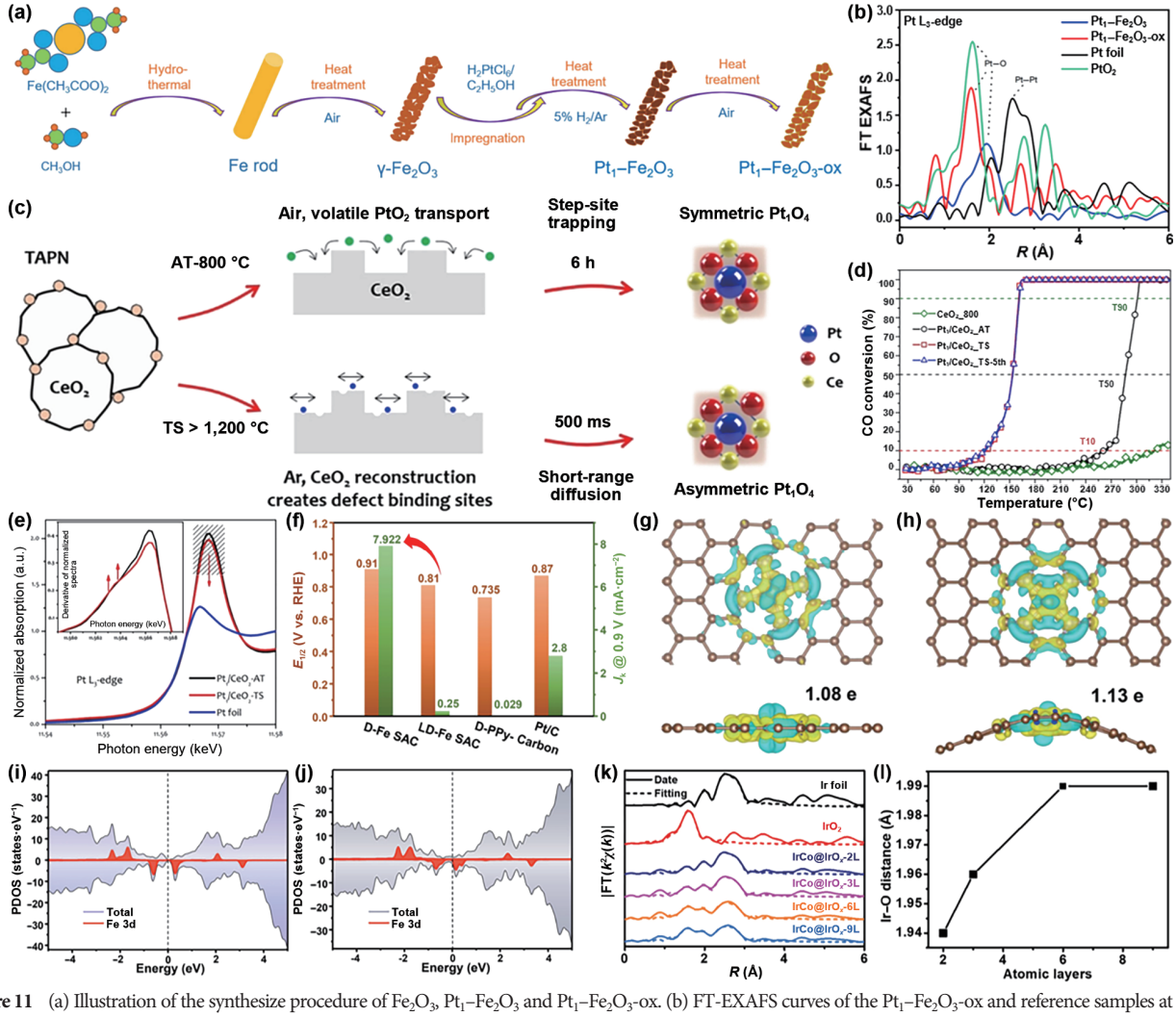

Figure 11 (a) Illustration of the synthesize procedure of Fe_2O_3, Pt_1–Fe_2O_3 and Pt_1–Fe_2O_3-ox. (b) FT-EXAFS curves of the Pt_1–Fe_2O_3-ox and reference samples at Pt L_3-edge. Reproduced with permission from Ref. [76], © Tsinghua University Press and Springer-Verlag GmbH Germany, 2020. (c) AT and TS synthesis of single-atom 1 wt.% Pt_1/CeO_2 catalysts showing the symmetric (near-perfect) and asymmetric (distorted square-planar) Pt_1O_4 coordination in Pt_1/CeO_2_AT and Pt_1/CeO_2_TS, respectively. (d) CO light-off curves collected over as-synthesized Pt_1/CeO_2_AT, Pt_1/CeO_2_TS, and bare CeO_2 calcined at 800 °C in air. Reaction conditions: 1 % CO, 10 % O_2, with N_2 balance, GHSV of 200 $L·g^{-1}·h^{-1}$. (e) Pt L_3-edge XANES of as-synthesized Pt_1/CeO_2 catalysts and the Pt foil reference. Inset is the first derivative of the normalized XANES. Reproduced with permission from Ref. [164], © Wiley-VCH GmbH 2021. (f) Half-wave potentials and kinetic current densities (0.9 V vs. RHE) of the catalysts. Charge density difference diagrams (yellow: electron accumulation, cyan: electron depletion) of planar (g) Fe–N_4 and (h) curved Fe–N_4. PDOS of (i) planar Fe–N_4 and (j) curved Fe–N_4. Reproduced with permission from Ref. [56], © Wiley-VCH GmbH 2021. (k) EXAFS fitting curves for Ir L_3-edge of IrCo@IrO_x-nL NDs (the plots are not corrected for phase shift). (l) Ir–O bond lengths of the IrCo@IrO_x-nL NDs with different atomic layers of IrO_x. Reproduced with permission from Ref. [166], © WILEY-VCH Verlag GmbH & Co. KGaA, Weinheim 2019.

analysis (Figs. 11(i) and 11(j)) shows that the d-band center of curved Fe–N_4 (−1.25 eV) was lower than that of planar Fe–N_4 (−1.18 eV), indicating that the adsorption of the intermediate was weakened. The results show that bending the Fe–N_4 site avoids excessive bonding between the oxygen-containing intermediate, which is the main reason for limiting the inherent ORR activity of the Fe–N_4 site. In addition, Wu et al. found that the evolution of the activity and stability of Fe–N_4 site during thermal activation produced strains that affected the bond length [55, 165]. According to XAS analysis results, Fe atoms in Fe–N_4 configuration after calcination at 700 °C have lower symmetry and shorter Fe–N bond length. With the increase of calcination temperature, out-of-plane ripple occurs in the carbon layer embedded with Fe–N_4 site, and local contraction strain occurs in Fe–N bond. In the ORR process, the small compression of Fe–N bond is favorable to the adsorption of O_2 and the subsequent bond breaking of O=O bond, while the large compression of Fe–N bond makes the ORR thermodynamics of Fe–N_4 site unfavorable. In addition, the structural evolution and enhanced activity of Co–N_4 sites at different temperatures were also observed [51]. The active site Co–N_4 with 2% compression strain formed at high temperature is a distorted non-planar configuration, and the Co–N bond is shortened. Central Co atoms exhibit more positive charge accumulation, resulting in stronger binding with O_2 and the intermediates. The method of constructing atomic layer IrO_x on IrCo nanodendrites with adjustable Ir–O bond length under acidic environment by compression strain effect is demonstrated [166]. *In situ* EXAFS showed that a growing IrO_x layer formed with the potential cycling, and the average Ir valence state increased gradually. As shown in Figs. 11(k) and 11(l), with the growth of atomic layers (IrO_x increases from 2 atomic layers to 9 atomic layers), the compression strain of IrO_x layer on IrCo nanodendrites decreases from 2.51% to strain-free state, and the length of Ir–O bond decreases from 1.94 Å to normal 1.99 Å. Compared with high strain (2.51%, 2 atomic layers) and no strain (> 6 atomic layers), the 3 atomic layers with Ir–O bond length of 1.96 Å (1.51% strain) on IrCo nanodendrites showed the best OER activity and the overpotential was only 247 mV to achieve a current density of 10 $mA·cm^{-2}$.

The change of bond length in different reactions has been

observed by *in situ* XAS [167]. Wang et al. reasonably designed a carbon based Mn–N_2C_2 bifunctional electrocatalyst [73]. The half-wave potential of ORR is 0.915 V and the overpotential of OER is 350 mV at 10 mA·cm^{-2} under alkaline condition. Through *operando* X-ray absorption fine structure measurement, it is found that the atom interface site of Mn^{2+}–N_2C_2 with extended bond length is the active center in ORR process, while the high-valence Mn^{4+}–N_2C_2 site with shortened bond length is the catalytic site of OER. As shown in Fig. 12(a), the average bond lengths of Mn–N and Mn–C are 1.99 and 1.95 Å, respectively. In the ORR process, the bond length of Mn–N increases from 1.99 to 2.03 Å and Mn–C increases from 1.95 to 1.99 Å at 0.78 V, while in the OER process, the bond lengths of Mn–N and Mn–C shorten to 1.96 and 1.91 Å at 1.70 V, respectively (Figs. 12(b) and 12(c)). During the ORR process, the fitting Mn value of the catalyst decreased from 2.9 to 2.2 (approximately from +3 to +2). However, during OER, the valence state changes from 3.1 to 3.8 (approximately +3 to +4). In addition, Chen et al. constructed a sulfur-modified Mn–N–C single-atom catalyst, which showed excellent ORR activity in alkaline medium with a half-wave potential of 0.916 V [168]. The local environmental evolution of single Mn site in MnSAs/S–NC was detected by *operando* EXAFS spectroscopy. According to the fitted structural parameters, the average bond length of Mn–N under catalytic conditions increases from 1.99 to 2.02 Å (0.916 V), which may be caused by oxygen chemisorption.

2.3.2 *Bond angle*

When the support is changed from graphene or large-diameter carbon nanotubes to small-diameter carbon nanotubes, curvature increases even though they have the same sp^2 hybrid carbon composition. The increase of curvature leads to the protrusion of sp^2 hybrid C atom and the misalignment of p orbital, which

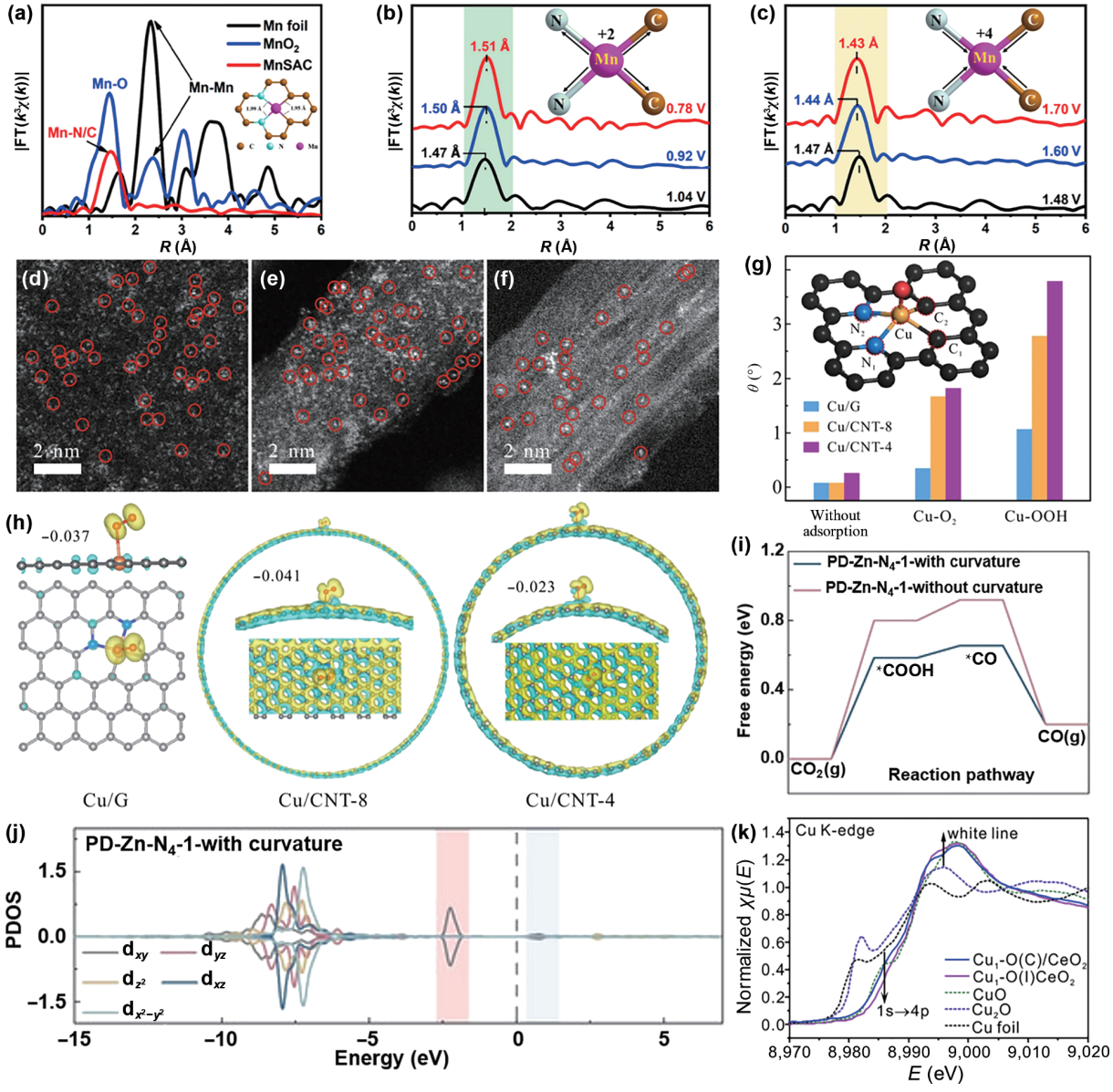

Figure 12 (a) Mn K-edge FT EXAFS spectra of MnSAC and the references. Inset is the atomic structure model for MnSAC. EXAFS spectra of MnSAC during (b) ORR and (c) OER. Reproduced with permission from Ref. [73], © American Chemical Society 2020. Spherical aberration corrected HAADF-STEM images of (d) Cu/G, (e) Cu/CNT-8, and (f) Cu/CNT-4. (g) Geometric descriptor θ of CuN_2C_2 active site at various stages of ORR for the three models (inset: illustration of the model used for geometry analysis). (h) Side view and top view of the charge density difference for three models with O_2^*, where yellow and blue areas represent higher and lower charge density, respectively. Reproduced with permission from Ref. [169], © Han, G. K., et al. 2021. (i) Free energy diagram for the conversion of CO_2 into CO at $U = 0$ V versus RHE on the PD-Zn–N_4-1-without and with curvature. (j) PDOS of d orbital in Zn atom for PD-Zn–N_4-1-with curvature. Reproduced with permission from Ref. [170], © Wiley-VCH GmbH 2020. (k) XANES spectra at the Cu K-edge of Cu_1–O(C)/CeO_2 and Cu_1–O(I)/CeO_2 with reference spectra of CuO, Cu_2O, and Cu foil. Reproduced with permission from Ref. [171], © Elsevier Inc. 2019.

enhances the torsional strain of carbon frame, resulting in the change of bond angle and affecting the reaction pathway. Du et al. demonstrated the dynamic behavior of the CuN_2C_2 site in *operando* ORR, revealing the geometric distortion of the active site regulated by substrate strain and its correlation with the activity [169]. In the spherical aberration corrected (AC) high-angle annular dark-field scanning transmission electron microscopy (HAADF-STEM), the bright spots are observed, which proves the atomic dispersion of Cu (Figs. 12(d)–12(f)). In order to maximize the activity of CuN_2C_2 SACs, it is critical to select different sp^2 hybrid carbon frameworks to regulate the structural distortion to an equilibrium point, with strong hybridization of Cu and O, while not over-breaking the original bonds of Cu–N/Cu–C. The best CuN_2C_2 site was found on carbon nanotubes with a diameter of 8 nm, which showed a six-fold increase in activity relative to that on graphene. Ideally, there is no geometric distortion for the CuN_2C_2 active site embedded in the planar sp^2 hybrid carbon framework. Distortion occurs with changes with coordination asymmetry, support curvature, or the induction of adsorbed species. As shown in Fig. 12(g), when O_2 is adsorbed on Cu, the adsorption deformation of Cu/CNT-8 on O_2 is more obvious, and its θ variation ($\Delta\theta$) is much larger than that of Cu/G (1.59° vs. 0.26°). High strains tend to be released by twisting the conjugated frame into a lower energy structure. According to the bond angle analysis, the geometric deformation of the newly formed axial Cu–O bond will cause the relaxation of adjacent bonds, thus reducing the local curvature, which is a thermodynamic advantage. The structure deformation of Cu/G is the least among the three models, and the lack of electron density change between Cu and O atoms indicates that the Cu–O hybridization is weak, which is not conducive to the charge transfer to $*O_2$ (Fig. 12(h)). However, the deformation of Cu/CNT-4 is so severe that the Cu–N bond after adsorption of $*O_2$ is too long, which weakens the conjugation of Cu 3d orbital with C/N p_z orbital and weakens the interaction between Cu–C/Cu–N, thus reducing the ability of N/C atoms to transfer electrons to the adsorption of $*O_2$ through the shared Cu atom. Compared with Cu/CNT-4 (−0.023) and Cu/G (−0.037), Cu/CNT-8 (−0.041) transfers more negative charges to $*O_2$, leading to more protonation of $*O_2$. Sufficient electron transfer promotes further reduction of adsorbed material.

Song et al. used onion-like nanospheres of carbon (OLC) to anchor stable atomically dispersed Pt as a catalyst for HER (Pt_1/OLC) [52]. In acidic medium, Pt_1/OLC catalyst (0.27 wt.% Pt) performed low overpotential (38 mV at 10 $mA·cm^{-2}$) and high TOF (40.78 H_2 s^{-1} at 100 mV), better than graphene-supported single-atom catalyst with similar Pt loading. At equilibrium potential, a strong *in situ* local electric field forms around the Pt site and protrudes the curved OLC surface like a tip. Proton is enriched significantly around Pt (> 1.99 $mol·L^{-1}$), which can improve the proton transfer of subsequent HER. In addition, Lin et al. constructed low-cost Zn single atoms on bent nitrogen-doped carbon nanofibers (Zn SAs/N–C) through a simple non-covalent self-assembly method [170]. At a low overpotential of only 330 mV, Zn SAs/N–C exhibited a high current density of 121.5 $mA·cm^{-2}$ and 94.7% FE_{CO} (Fig. 12(i)). DFT calculation shows that Zn–N_4 with curvature has a lower free energy barrier in the RDS of *COOH formation compared with Zn–N_4 without curvature, indicating that curvature does improve its catalytic activity of CO_2 electroreduction to CO. The calculated Bader charge results show that Zn atoms on Zn–N_4 with curvature show a lower positive charge than that without curvature, indicating that the curvature causes the increase of electron density of Zn atoms. With the introduction of curvature, the d_{x2-y2} orbital electrons of Zn atom at Zn–N_4 disappear from Fermi level region and transfer to the lower energy region between −10 and −5 eV (Fig. 12(j)), indicating that the d_{x2-y2} orbital electrons are released back to Zn atom from Zn–N bond, thus increasing the electron density of Zn atom.

2.3.3 *Bond polarity*

The polarity of chemical bonds at the active site has an effect on heterogeneous catalysis. Li et al. used an efficient strategy to increase the polarity of the Cu–O bond in the single-atom Cu catalyst to facilitate additive-free hydroboration of alkynes to produce a variety of important vinylboronate compounds [171]. By controlling the synthesis process, ionic Cu_1–O(I)/CeO_2 and covalent Cu_1–O(C)/CeO_2 single atom site Cu catalysts can be obtained. As shown in Fig. 12(k), the XANES spectra of Cu_1–O(I)/CeO_2 and Cu_1–O(C)/CeO_2 are close to CuO, which means that the Cu atoms in these two single-atom Cu catalysts are in a valence state close to +2. However, compared with Cu_1–O(C)/CeO_2, the white line peak of Cu_1–O(I)/CeO_2 is stronger, indicating that the Cu center in Cu_1–O(I)/CeO_2 has a lower electron density and a more distorted coordination structure. The low electron density of Cu and the high electron density of O atoms essentially mean that the Cu–O bond in Cu_1–O(I)/CeO_2 is more ionic and more polar than the Cu–O bond in Cu_1–O(C)/CeO_2. The increased ionic properties of the Cu–O bond promote the formation of copper ethoxide species through the dissociation of ethanol molecules and enable Cu_1–O(I)/CeO_2 to selective hydroboration of many alkynes without additives with much higher activity than Cu_1–O(C)/CeO_2.

3 Spacing of active atoms

The remarkable geometric and electronic structure and great flexibility of NPs provide a vast space to influence the breaking and formation of chemical bonds, essentially driving the development of nanocatalysts for decades [59, 172–174]. The compressive or tensile arrangement of the surface atoms will change the lattice strain, thus changing the atomic spacing at the atomic scale and regulating the adsorption configuration of the reactants. Recent studies have shown that adjusting the lattice strain of metal catalysts can affect catalytic activity because the lattice strain can alter the electronic structure of the catalyst, which thus affects the adsorption of reactants [174–177]. For example, Cui et al. reported a method using battery electrode materials to directly and continuously control the lattice strain of Pt catalysts and thus regulate the catalytic activity of ORR [174]. The volume changes can be precisely controlled by electrochemical switching between the charge and discharge states of the battery electrodes to induce compressive or tensile strains on the loaded catalyst, with layer spacing varying from 4.69 to 4.82 Å. ORR activity was observed to be increased by 90% or inhibited by 40% under compression or tension, respectively, which is consistent with theoretical predictions. Therefore, the spacing of active metal atoms in nanocatalysts is very important for catalytic reaction. Ideally, changing the atomic spacing of monolayer active metals by doping other atoms is a valuable model for understanding the relationship between atomic spacing and catalytic performance at the atomic scale. This section will discuss the adjustment of the spacing of active metal atoms in intermetallic compounds and metal layers respectively, the effect of which is gradually enhanced.

3.1 Intermetallic compounds

Intermetallic compounds have attracted extensive attention in the field of heterogeneous catalysis due to their high ratio of surface atoms and their potential to improve catalytic performance by changing the geometric and electronic structure of the active

metal [178–180]. Intermetallic compounds have uniform crystal structure and highly ordered atomic arrangement. To date, a variety of methods have been developed to adjust the electronic structure of metals, such as using surface organic ligand modifiers and creating metal–support interactions [181–184]. Among them, another atom doped can effectively adjust the spacing of active atoms, so as to better adapt to the requirements of catalytic reaction and improve selectivity without changing the composition of active sites.

For example, the lattice strain of Ru catalysts can greatly affect their selectivity [185]. Compared with the original Ru, Ru with 3% lattice compression showed a high catalytic selectivity (99% vs. 66%) for the hydrogenation of 4-nitrostyrene to 4-aminostyrene. The AC-HAADF-STEM (Fig. 13(a)) shows that Co causes the compressive lattice strain of Ru, and the lattice fringe at both ends is 2.08 Å, smaller than the original Ru (0001) (2.14 Å). In addition, in Fig. 13(b), there is a shoulder peak of Ru K-edge FT-EXAFS at about 2.1 Å, which can be attributed to Ru–Co scattering, and its intensity becomes stronger with the increase of Co content. The above results indicate that there is a strong interaction between Co core and Ru shell, and the Ru–Ru bond gradually shrinks with the increase of Co component in Co–Ru NPs. The total reaction pathway of ethylene hydrogenation is $C_2H_4^* + H^* \rightarrow C_2H_5^*$ and $C_2H_5^* + H^* \rightarrow C_2H_6^*$. In the absence of strain, the activation barriers of the first step and the second step are 29.25 and 12.64 kcal·mol^{-1}, respectively, indicating that the hydrogenation of the first step is the RDS. When the lateral strain is 3%, the first activation barrier increases slightly, while the second activation barrier increases significantly compared with the system without lateral strain, making the second activation become the RDS. When the lateral compressive strain increases to 6%, the first activation barrier decreases to 17.25 kcal·mol^{-1}, which is favorable for the hydrogenation of ethylene to ethyl.

3.2 Metal atomic layer

For core–shell structure of metal nanocatalysts, the inner core will change the spacing of metal atoms in the outer shell. Miller et al. synthesized a series of SiO_2-supported Pt@Pt_1Sn_1 nanoparticles on Pt nanoparticles with highly ordered hexagonal Pt_1Sn_1 intermetallic shell for propane dehydrogenation [186]. In typical Pt_1Sn_1 intermetallic compounds, the Pt–Sn bond distance (2.73 Å) is close to the Pt–Pt bond distance (2.72 Å). However, in bimetallic samples, the Pt–Sn bond distance is significantly smaller than Pt–Pt bond distance due to the effect of the micro-strain between Pt and Pt_1Sn_1. The surface geometry of bimetallic nanoparticles is basically the same (hexagonal Pt_1Sn_1), but their surface electronic structure is different, resulting in similar selectivity of propylene and different activity of propane dehydrogenation. Compared with single metal Pt catalyst, Pt_1Sn_1 phase reduces the Pt–Pt coordination number and Pt ensembles. The high propene selectivity of the Pt–Sn catalysts is due to the geometric effect of Sn on Pt that isolates surface Pt atoms. The

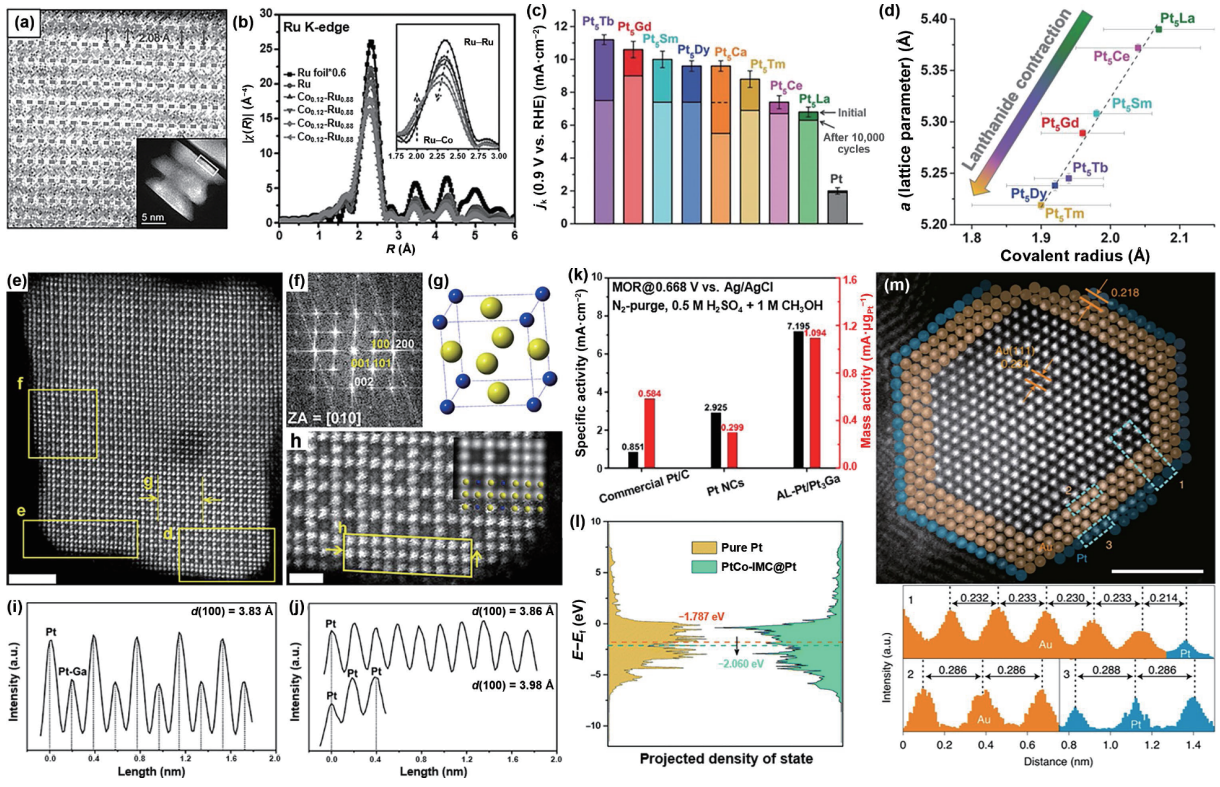

Figure 13 (a) Atomic-resolution HAADF-STEM images of Co–Ru NPs. (b) XAFS spectra for the Ru K-edge. Reproduced with permission from Ref. [185], © Wiley-VCH Verlag GmbH & Co. KGaA, Weinheim 2017. (c) Kinetic current density, j_k, of Pt_5M and Pt at 23 °C, 1,600 revolutions per minute in O_2-saturated 0.1 M $HClO_4$, before and after a stability test consisting of 10,000 cycles between 0.6 and 1.0 V versus RHE at 100 mV·s^{-1}. (d) Relation between the lattice parameter a of Pt_5M measured by XRD and the covalent radius of the lanthanide atoms. Reproduced with permission from Ref. [188], © American Association for the Advancement of Science 2016. (e) HAADF-STEM image of an individual 10 nm AL-Pt/Pt_3Ga viewed along the [010] zone axis. Scale bar: 2 nm. (f) FFT pattern of the AL-Pt/Pt_3Ga shown in (e). (g) Unit cell of the intermetallic Pt_3Ga phase. Yellow and blue spheres represent Pt and Ga atoms, respectively. (h) Enlarged high-resolution HAADF images taken from the selected areas indicated by yellow rectangles in (e). Scale bar: 0.5 nm. (i) and (j) The line intensity profiles taken along the atomic layers marked by the yellow arrows in (e) and yellow rectangle in (h), respectively. (k) Specific activity and mass activity of the three catalysts at 0.668 V vs. Ag/AgCl. Reproduced with permission from Ref. [189], © American Chemical Society 2018. (l) PDOS of Pt on two model structures. Reproduced with permission from Ref. [190], © The Royal Society of Chemistry 2022. (m) Representative atomic-resolution HAADF-STEM images of Au@1ML-Pt with the corresponding line intensity profiles along the numbered dashed rectangles to show the interplanar distance and the lattice distance. The atoms in the outer layers are shown as light yellow and blue spheres to highlight the gold core and platinum shell. Reproduced with permission from Ref. [193], © Guan, Q. Q., et al. 2021.

electron effect of Sn on Pt results in a higher XANES energy level, indicating that the unfilled state level of Pt 5d is higher, and the adsorption energy of hydrocarbons on Pt is reduced. Face-centered cubic Pt–Cu random alloy shells were deposited on the PdCu B_2 intermetallic compound seeds in a face-dependent manner, resulting in a faceted core@shell NPs with high surface strain [187]. These core@shell NPs provided higher specific surface area and larger scale activity for ORR compared to traditional Pt–Cu NPs. In addition, ORR on eight Pt–lanthanides and Pt–alkaline earth electrodes Pt_5M was studied, with a 3- to 6-fold increase in activity (Fig. 13(c)) [188]. The active phase is composed of Pt shell formed by acid leaching. Lattice parameters *a* and Pt–Pt distance decrease from left to right in the lanthanide series (Fig. 13(d)). Pt_5Tb is the most active electrocatalyst and shows compression of about 3%, close to the optimal OH binding energy of Sabatier volcano.

Li et al. reported a tensile-strain Pt with 2–3 atomic layers on intermetallic compound Pt_3Ga (AL-Pt/Pt_3Ga) as an active electrocatalyst for methanol oxidation reaction (MOR) [189]. As shown in Figs. 13(e)–13(j), the result of atomic-resolution HAADF-STEM indicates that the tensile strain of AL-Pt along the direction [001] is 3.2%, while the tensile strain along the direction [100]/[010] is negligible. For MOR, the specific activity (7.195 mA·cm^{-2}) and mass activity (1.094 mA·μg_{Pt}^{-1}) of AL-Pt electrocatalyst under tensile strain were significantly higher than those of unstretched Pt/C catalyst and commercial Pt/C catalyst (Fig. 13(k)). All electron transfer element steps are exothermic on the tensile surface. This is due to the tensile strain that makes all intermediates bind more strongly, especially CO* + OH*. The stronger OH* binding indicates that water is more easily activated, thus removing CO*. The high reactivity of the tensile catalyst was consistent with the rise of the d-band center on the tensile surface (−2.54 eV) as compared to the unstrained surface (−2.77 eV). In addition, Yang et al. proposed a cobalt oxide assisted thermal migration strategy to ensure efficient structural evolution from ultrafine Pt nanocrystals to a sub-6 nm high-loaded (about 44.7 wt.%) Pt_1Co_1 intermetallic core–shell structure containing 2–3 Pt shell atomic layers (Pt_1Co_1-IMC@Pt/C) [190]. The prepared catalysts not only showed excellent ORR activity and durability, but also recorded high power density and exceptional stability in H_2-air/O_2 fuel cells, indicating that excellent activity can be expressed efficiently under proton exchange membrane fuel cell (PEMFC) operating conditions. FT-EXAFS spectra and the fitting results of Pt L_3-edge indicate that the Pt–Pt bond length (0.269 Å) of 700-Pt_1Co_1-IMC@Pt/C-2.5 is significantly shortened compared to the Pt foil (0.276 Å). This is because smaller Co atoms are added to the Pt lattice. As shown in Fig. 13(l), Pt_1Co_1-IMC@Pt shows a lower d-band center than pure Pt, indicating that the antibonding orbital is filled with more electrons and oxygen adsorption is weakened. Compared with pure Pt structure, the adsorption energy of the intermediates in Pt_1Co_1-IMC@Pt model is obviously weakened, indicating that the ligand effect between Pt and Co atoms caused by the electron transfer from Co to Pt greatly affects the adsorption behavior of the intermediates at the Pt site. In addition, Abruña et al. described a novel Pt–Co nanocatalyst consisting of an ordered Pt_3Co intermetallic core and a 2–3 atom thick platinum shell [191]. Compared with disordered Pt_3Co/C alloy, these nanoparticles have stronger activity and durability. Pt shells strain on ordered intermetallic compound core with 0.8% smaller lattice constants than those of disordered alloys. At +0.9 V, the specific activity of Pt_3Co/C-700 is 1.1 mA·cm_{Pt}^{-2}, which is much higher than that of pure Pt.

If the active metal atoms can be arranged into ideal monolayer and other spaced atoms can be inserted into it, the spacing of the active metal atoms can be flexibly adjusted, thus affecting the electronic structure and catalytic performance. At this point, the adjustment of atomic spacing will be more efficient and clearer, and will be more powerful for understanding the effect of atomic spacing on catalytic reactions. Corma et al. reported that the activity of PtAu bimetallic catalysts was much higher than that of Au NPs, but still much lower than that of Pt single metal catalysts [192]. In contrast, Lu et al. precisely controlled platinum monolayers deposited on large gold NPs to break its activity-selectivity balance for particle size, resulting in significant activity with a selectivity of 99% for haloanilines under mild conditions [193]. As shown in Fig. 13(m), the lattice distance within the platinum layer is 2.86 Å, close to the underlying gold lattice, expanding 3.2% compared to the bulk platinum (2.77 Å). This lattice expansion and orbital hybridization between platinum cause the of the 5d-band center of Pt to rise by 0.69 eV toward the Fermi level, which makes the exposed Pt layer more reactive. In fact, the binding strength of all reactants and intermediates for hydrogenation of *para*-chloronitrobenzene at 1ML-Pt/Au (111) is improved. On the other hand, on 1ML-Pt/Au (111) plate, the reaction barrier of *para*-chloroaniline dechlorination is still considerable at 0.60 eV, and the reaction energy is thermally neutral (−0.12 eV), similar to Pt (111) but different from Pt (211), with a large exothermic reaction energy of −0.79 eV.

4 Synergistic effect of different metal atoms

Single-atom sites have only a single active metal atom and can catalyze only simple elementary reactions, which makes them difficult to break the linear relationship between the adsorption energy of reaction intermediates and ineffective for some reactions. Compared with single metal NPs, intermetallic compounds have the potential to bring synergistic effect between the two metals by forming atom-pair sites, resulting in alteration of the catalytic active sites. Further, by precise design, metal atoms can be inserted into an inert metal in order to be separated into isolated atoms [194–196]. These materials are called single-atom alloys, and interactions between isolated metal atoms are negligible compared to intermetallic compounds. Among them, the synergistic effect between the support and the single atom is clearer, which plays a key role in the realization of high-performance catalysis. In addition, dual-atom catalysts are a new frontier in the field of heterogeneous catalysis because synergistic effect between adjacent metal atoms can improve their catalytic activity while maintaining the advantages of single-atom catalysts [197–200]. This is helpful to break the inherent linear relationship between the adsorption energies of the reaction intermediates and further improve the catalytic performance. Although DACs have many unique advantages, the synthesis of such materials remains a significant challenge, mainly due to the difficulty of controlling the configurational uniformity of the active sites at the atomic scale [201, 202]. In addition, the role of other atomic catalysts including trinary-atom catalysts in changing catalytic mechanism and catalytic performance is still worth studying [111, 203–205]. In this section, we will discuss the synergistic effect between dual-atom sites, including intermetallic compounds, SAAs, and DACs, as well as polyatomic sites, emphasizing how they affect reactant adsorption and catalytic processes.

4.1 Intermetallic compounds

When metal atoms are separated by other metal atoms, the active site may change from one metal to two, and the synergistic effect will occur. For example, for CO_2RR to produce CO, the stability of the intermediate COOH* and the desorption of CO* are two key steps. Pd is easy to stabilize COOH*, but strong CO* binding on

Pd surface leads to severe poisoning, which reduces the catalytic activity and the stability of CO_2 reduction. However, on the Ag surface, CO* is easy to desorption, while COOH* requires a higher formation energy, resulting in a higher overpotential. In view of the above problems, Chen et al. successfully designed PdAg bimetallic catalyst to overcome the shortcomings of Pd and Ag single metal catalysts [206]. The overpotential of Ag terminated PdAg catalyst (−0.55 V) is much lower than that of Ag (−0.76 V) when the CO current density is 1 mA·cm^{-2}, and the CO/H_2 ratio is 18 times higher than that of Pd at 0.75 V.

As an effective strategy to optimize the selectivity of Pt catalyst by isolating neighboring Pt atoms, Pt–Zn intermetallic compound nanoparticles were formed on hollow nitrogen-doped carbon nanotubes (PtZn/HNCNT) (Figs. 14(a) and 14(b)) [71]. On Pt (111) surface, the first energy barrier for hydrogenation of nitryl group and acetylene group is 239 and 117 kJ·mol^{-1}, respectively (Fig. 14(c)), indicating that the kinetic process of hydrogenation of nitryl group is unfavorable. As shown in Fig. 14(d), on the surface of PtZn (022), hydrogen atoms tend to adsorb on the Pt–Zn bridge. The relative vertical distance between H* and its hydrogenation target atom (oxygen on nitro group or carbon on alkyne group) is close (0.897 vs. 0.978 Å). For 4-NPA@PtZn (022), hydrogenation on the nitro group follows the hydrogen diffusion path from Pt–Zn(bridge) to Zn–Pt(bridge). The construction of Pd–Zn dual sites with good and uniform exposure can significantly improve the efficiency of ethanol oxidation reaction (EOR) (Fig. 14(e)) [72]. Compared with Pd–Pd site and single Pd site, the activity of ethanol electrooxidation at Pd–Zn site was much higher, and about 24 times higher than that of commercial Pd/C (Fig. 14(f)). Theoretical studies show that for a single Pd site,

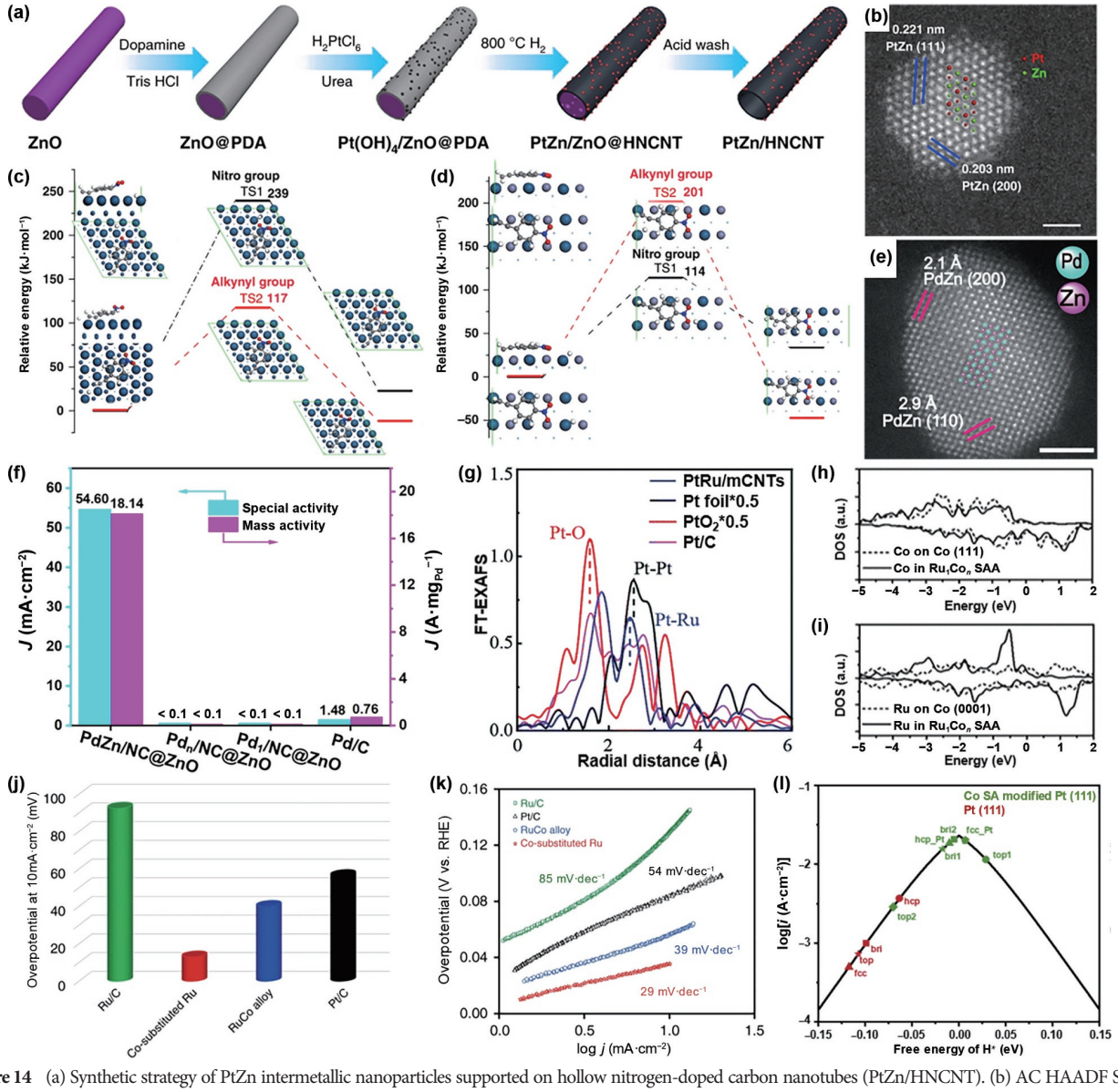

Figure 14 (a) Synthetic strategy of PtZn intermetallic nanoparticles supported on hollow nitrogen-doped carbon nanotubes (PtZn/HNCNT). (b) AC HAADF STEM image of a PtZn IMC nanoparticle. Scale bar, 1 nm. The first elementary hydrogenation reaction steps on both nitro and alkynyl groups over (c) Pt (111) and (d) PtZn (022$^-$) surface. Reproduced with permission from Ref. [71], © Han, A. J., et al. 2019. (e) AC-HAADF-STEM elemental mappings of one PdZn nanoparticle in PdZn/NC@ZnO. Scale bar: 2 nm. (f) Mass and specific activities of PdZn/NC@ZnO and commercial Pd/C. Reproduced with permission from Ref. [72], © Qiu, Y. J., et al. 2021. (g) The FT k^2-weighted EXAFS spectra of PtRu/mCNTs, Pt/mCNTs, Pt foil, and commercial Pt/C and PtO_2. Reproduced with permission from Ref. [209], © The Royal Society of Chemistry 2022. (h) PDOS on d orbitals of the surface Co atom on Co (111) (dashed line) and in Ru_1Co_n SAA that bonds to the Ru atom (solid line). (i) PDOS on d orbitals of the surface Ru atom on Ru (0001) (dashed line) and in Ru_1Co_n SAA (solid line). Reproduced with permission from Ref. [210], © American Chemical Society 2021. (j) Overpotentials at 10 mA·cm^{-2} of Ru/C, Pt/C, RuCo and Co-substituted Ru. (k) Tafel plots of Ru/C, Pt/C, RuCo and Co-substituted Ru in 1 M KOH. Reproduced with permission from Ref. [212], © Mao, J. J., et al. 2018. (l) Exchange current i_0 for HER as a function of *H adsorption free energy for the adsorption sites in Pt (111) and Co SA modified Pt (111). Reproduced with permission from Ref. [216], © Elsevier Ltd. 2021.

when CH_3CH_2O is formed, the EOR process will be interrupted due to the exclusive hydrogen bond formed. For the Pd–Pd site on Pd NPs, ethanol adsorbs on Pd atoms during EOR and is prior to methylene C–H bonds. In contrast, for PdZn NPs, the presence of Zn atoms is more conducive to the adsorption of ethanol on Pd–Zn dual sites than Pd atoms, and it is easier to destroy hydrogen bonds rather than methylene C–H bonds in ethanol dehydrogenation process, adjusting the EOR process into a favorable path. The results showed that the initial dehydrogenation of ethanol at the Pd–Zn site is easier than that at the Pd–Pd site (−37.88 vs. −35.38 kcal·mol^{-1}). At the same time, the desorption process of acetic acid at the Pd–Zn dual site was much easier than that at the Pd–Pd dual site (1.27 vs. 7.72 kcal·mol^{-1}).

4.2 Single atom alloys

In general, the host metal can optimize the electronic structure of the isolated metal atoms on the nanocrystals, thus changing the activation barrier of the reactants and the binding strength of the intermediates, thus regulating the catalytic performance [207]. The principle behind this phenomenon is to understand how the molecule matches the active site of the catalyst at the atomic level. Interestingly, it is possible that the single atoms in SAAs is not the active site but is used to regulate the electronic properties of the host metal [208]. Therefore, the single atom and the support can be mutually optimized to meet the requirements of high activity and selectivity. In addition, the introduction of other isolated atoms on the support can form the active site of dual metal atoms, at which time the adsorption mode of the reactants may change, thus affecting the catalytic performance more significantly.

The electronic structure of isolated single atoms can be regulated by nano metal supports. Yao et al. synthesized PtRu alloy with uniform platinum atoms anchored on the surface of Ru matrix by laser irradiation in liquid method [209]. PtRu alloy NPs exhibited excellent pH-universal HER performance, extremely low overpotential, and good stability. As shown in Fig. 14(g), FT k^2-weighted EXAFS spectra of PtRu/mCNTs show a Pt-metal coordination peak at 2.47 Å, which is shorter than the nearest coordination shell of Pt atoms in Pt foils and can be attributed to the Pt–Ru bond. In addition, the geometric structure of PtRu/mCNTs and electronic structure (d-band center up-shift) are self-optimized under operating conditions, ensuring excellent HER performance under wide pH conditions. Li et al. designed a Ru_1Co_n SAA catalyst to anchor isolated Ru atoms on the surface of Co NPs through a two-dimensional confinement strategy, which greatly increased Fischer–Tropsch synthesis activity (2.6 $mol_{CO}·mol_M^{-1}·h^{-1}$) and long-chain hydrocarbon selectivity (C_{5+}: 86.0%) [210]. Compared with 1.81 and 1.39 eV on Co (111) and Ru (0001) surfaces, Ru_1Co_n SAA system has the lowest reaction barrier (1.22 eV), leading to the highest Co conversion activity. As shown in Figs. 14(h) and 14(i), the PDOS of Ru atoms in Ru_1Co_n SAA show much higher electron densities near the Fermi level than that of Ru (0001). Therefore, there is a stronger interaction between Ru atoms and the reactants, thus improving the catalytic performance. In addition, Wang et al. reported that some noble metal modifiers can adjust the crystal phase and surface structure of Co particles, thus adjusting the chemisorption of reactants, which is conducive to CO dissociation and hinders the formation of CH_4 [211]. The single-atom alloy Ir–Co nanoparticles on CNT (Ir–Co/CNT) in the hexagonal close-packed (hcp)-phase not only showed high CO conversion activity, but also showed good selectivity for C_{5+} hydrocarbons (95%). Ir–Co/CNT catalyst had good stability of 1,300 h. In addition to the advantages of hcp-phase, the presence of isolated Ir on Co particles promoted CO dissociation and C–C coupling, and increased the water oxidation resistance of Co particles in Fischer–Tropsch reaction. As for non-noble metals, Wang et al. reported a highly active and stable hydrogen evolution of Co-substituted Ru nanosheets in which Co atoms are isolated in a Ru lattice ($RuCo_1$) [212]. Impressively, $RuCo_1$ required only a very low overpotential of 13 mV to achieve a current density of 10 mA·cm^{-2} and a very low Tafel slope of 29 mV·dec^{-1} in 1 M KOH medium (Figs. 14(j) and 14(k)). Compared with Ru, the dissociation barrier of water decreases significantly after Co single atom replace. Sykes et al. prepared NiAu SAA catalyst for selective non-oxidative dehydrogenation of ethanol to acetaldehyde and hydrogen [213]. Isolated Ni atoms in Au NPs are active and 100% selective for conversion of ethanol to acetaldehyde and hydrogen at low temperature. In addition, Ni atoms cycle their charge states during the reaction in a manner similar to that of homogeneous catalysts. Ni_3Ga catalyst mainly has π-adsorption and weakened σ-adsorption, showing high ethylene selectivity [214]. Duan et al. prepared NiGa intermetallic catalysts with completely isolated Ni sites to optimize the semi-hydrogenation of acetylene [215]. These Ni sites not only showed preferential adsorption of acetylene π, but also showed enhanced desorption of ethylene.

Isolated single atoms can in turn affect the electronic structure of nano supports. Sun et al. reported single-atom Co modified Pt catalysts by ALD [216]. Compared with commercial Pt/C catalysts, the prepared catalysts showed higher mass activity and excellent stability in HER and ORR. Compared with Pt NPs and Pt foils, the white line of Co modified Pt catalyst is strongest, indicating a reduction in the number of electrons in the occupied d-band. The Pt–Pt bond distance of Co-modified Pt NPs is reduced to 2.73 Å, which is also lower than that of Pt foil 2.76 Å. These results indicate that the electronic structure of Pt is tuned and the surface of Pt is reconstructed with the deposition of Co atoms on Pt. In general, the hydrogen bonds on Pt (111) are strong and concentrated to the left of the volcano (Fig. 14(l)). The calculation of Co SA modified Pt (111) showed that ΔG_{H^*} decreased to the optimal region of HER activity. In addition, the d-band centers of Pt (111) (−1.94 eV) and Co SA modified Pt (111) (−2.04 eV, −2.30 eV) also indicate that Co SA can change the electronic structure of Pt surface atoms by lowering the d-band. Therefore, the adsorption strength of hydrogen is weakened, leading to optimal HER activity. In addition, Zeng et al. proposed a single-atom Pd alloy Cu catalyst (Pb_1Cu) that can convert CO_2 to formate (about 96% Faraday efficiency) and has a high activity of over 1 A·cm^{-2} [208]. Pb_1Cu electrocatalyst converts CO_2 to formate on modulated Cu rather than isolated Pb.

Isolated metal atoms and nano metal supports can act as reaction sites simultaneously, thus showing synergistic effect. Zeng et al. developed highly active and selective catalysts for selective hydrogenation by embedding Pt single atoms on the surface of Ni nanocrystals (Pt_1/Ni) [217]. In the hydrogenation process of 3-nitrostyrene, the TOF value of Pt atoms on the surface of Pt_1/Ni nanocrystals reached 1,800 h^{-1} at 40 °C and 3 atm, which is much higher than that of Pt single atoms supported by activated carbon, TiO_2, SiO_2, and ZSM-5 (Fig. 15(a)). H atoms generally add to substrate molecules only on the top of the active metal atoms. In this case, the H atom diffuses from the middle empty site to the top site. As shown in Figs. 15(b) and 15(c), in Pt_1/Ni (111), Pt single atom acts as the active site because Pt single atom has a lower diffusion energy barrier than Ni atom. The Ni nanocrystals act as a support to fix Pt single atoms in Pt_1/Ni (111) and as a reservoir to provide active H atoms to facilitate hydrogenation reactions. Therefore, the high activity of Pt_1/Ni nanocrystals comes from an adequate supply of hydrogen. In addition, Hong et al. successfully synthesized the anisotropic superstructures (ASs) of single-atom Pt encapsulated hcp Ni nanosheets, exhibiting an

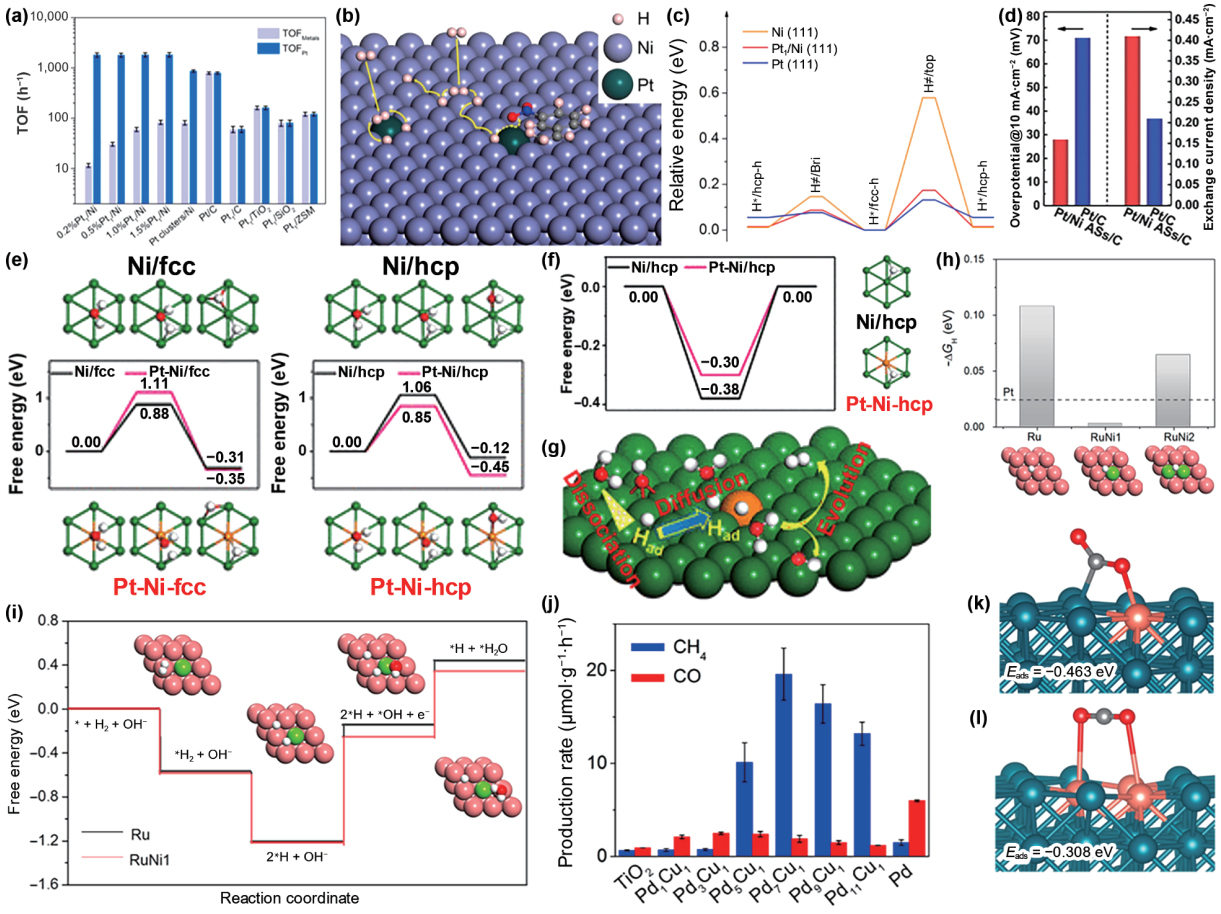

Figure 15 (a) Comparison of TOF numbers for different Pt single-atom catalysts, Pt clusters/Ni nanocrystals, and Pt/C under 3 atm of H_2 at 40 °C. (b) Schematic illustration of H_2 dissociation and H diffusion on Pt_1/Ni (111). (c) Diffusion paths of H atoms on Ni (111), Pt_1/Ni (111), and Pt (111). Reproduced with permission from Ref. [217], © American Chemical Society 2018. (d) Exchange current densities and overpotentials to reach 10.0 mA·cm^{-2}. (e) Water dissociation kinetics on Ni-fcc and Ni-hcp with and without monoatomic Pt. (f) Hydrogen adsorption free energies on Ni-hcp and Pt–Ni-hcp. (g) Proposed hydrogen generation pathways on monoatomic Pt embedded hcp Ni, namely the dissociation-diffusion-desorption mechanism. Reproduced with permission from Ref. [218], © American Chemical Society 2021. (h) Calculated hydrogen adsorption energies on pure Ru, single-atomic Ni and biatomic Ni dispersed on Ru catalysts and corresponding structure model of Ru, $RuNi_1$, and $RuNi_2$. The dashed line represented the optimized calculated hydrogen adsorption energy of Pt. (i) Free energy diagrams of the elementary processes of HOR on Ru and $RuNi_1$ including atomic configurations of each state on various metal surfaces. Color: orange, Ru; green, Ni; red, O; white, H. Reproduced with permission from Ref. [219], © American Chemical Society 2020. (j) Average production rates of CH_4 and CO in photocatalytic CO_2 reduction with H_2O by bare TiO_2, Pd_1Cu_1–TiO_2, Pd_3Cu_1–TiO_2, Pd_5Cu_1–TiO_2, Pd_7Cu_1–TiO_2, Pd_9Cu_1–TiO_2, $Pd_{11}Cu_1$–TiO_2, and Pd–TiO_2 hybrid structures under ultraviolet (UV)-light (λ < 400 nm) irradiation with a power density of 2 mW·cm^{-2}. The catalysts are 5 mg of TiO_2 loaded with 0.01 mmol of metal atoms. Most favorable configurations and adsorption energies of CO_2 at (k) an isolated Cu atom (i.e., a Cu–Pd pair), and (l) two neighbored Cu atoms (i.e., a Cu–Cu pair). Reproduced with permission from Ref. [220], © American Chemical Society 2017.

efficient mechanism for hydrogen evolution [218]. As shown in Fig. 15(d), the overpotential of Pt/Ni ASs was 28.0 mV to reach the specific current density of 10 mA·cm^{-2}, which was much lower than that of conventional Pt/C catalyst (71.0 mV). As illustrated in Fig. 15(e), the metastable hcp Ni (001) surface plays a dominant role in water activation. Single-atom Pt is not a suitable dissociation site because of the high dissociation energy barrier on it. The delocalization of electrons on metal surfaces is beneficial to the free diffusion of H. For single-atom Pt, the free energy of hydrogen adsorption at the adjacent site is −0.30 eV, while that at the intrinsic pure Ni-hcp site is −0.38 eV (Fig. 15(f)). It shows that H is more likely to combine the second proton–electron pair to carry out Heyrovsky process when adsorbed H moves around single-atom Pt. Therefore, the catalyst shows synergistic effect of Pt and hcp Ni ASs, and has good HER activity (Fig. 15(g)).

When the active site changes from one metal to two metal atoms, the synergistic effect is even more pronounced. Wang et al. reported a novel hydrogen oxidation reaction (HOR) catalyst ($RuNi_1$) in which Ni atoms were dispersed on Ru nanocrystals [219]. It is noteworthy that the prepared $RuNi_1$ catalyst shows good catalytic activity and stability in alkaline medium, superior to RuNi bimetallic nanocrystals, primitive Ru, and commercial Pt/C catalysts. DFT calculations show that the preferred hydrogen adsorption sites on the surface are all concave sites formed by three atoms. As shown in Fig. 15(h), for pure Ru, the adsorption capacity of hydrogen is too strong and the adsorption energy is −0.11 eV. The adsorption affinity of Ru catalyst decreases significantly when Ni atoms are added. After the separation of single Ni atoms, the free energy of the water formation step decreases significantly from 1.067 to 0.966 eV (Fig. 15(i)). Xiong et al. developed highly selective sites for CO_2 photocatalytic conversion to CH_4 by isolating Cu atoms in palladium lattices [220]. As shown in Fig. 15(j), the CH_4 yield of Pd_7Cu_1–TiO_2 photocatalyst was 19.6 μmol·g_{cat}^{-1}·h^{-1}, and the selectivity was 96%. When Cu atoms are completely isolated by Pd lattice, the optimal adsorption configuration of CO_2 occurs on the adjacent Cu–Pd pair, and the adsorption energy is −0.463 eV (Fig. 15(k)). In sharp contrast, the adsorption of CO_2 to adjacent Cu–Cu pairs is significantly weaker (−0.308 eV) (Fig. 15(l)). The Cu d-band center of Pd_7Cu_1 was significantly higher than that of Pd_1Cu_1 (−1.161 vs. −1.452 eV). When Cu atoms are surrounded by more Pd atoms, the electronic structure of Cu atoms is more

influenced by Pd atoms, so that the d-band center of Cu atoms is better improved.

4.3 Dual-atom catalysts

The two metal atoms in dual-atom sites can interact and stabilize each other, which is beneficial to improve the stability of the catalyst. The active center of SACs contains only one metal atom, and molecules can only be adsorbed in end-on or side-on configurations. However, the active site of DACs consists of two metal atoms, and bridge adsorption can occur in addition to top adsorption. Therefore, the adsorption of reactants on the catalyst can be more flexible, which is conducive to the activation of reactant molecules, stretching and weakening the relatively stable double or triple bond, thus contributing to the improvement of reaction activity [221]. In addition, in SACs, the structure of the active center is relatively simple, which is conducive to improving the reactivity of simple steps, but has limited ability to improve the reactivity of multi-proton and electron transfer reactions. DACs can optimize the interaction between the reactant or intermediate and the active site and more effectively adjust the location of the d-band center through the interaction between two metal atoms, thereby lowering the energy barrier of the RDS and dynamically accelerating the reaction. In general, depending on the catalytic center, DACs can be divided into two types: binuclear homologous dual-atom pairs and binuclear heterogeneous dual-atom pairs.

Wang et al. synthesized loaded Pd_2 DAC and applied it for the first time in electrochemical CO_2RR [5]. At 0.85 V, the CO catalytic efficiency of Pd_2 DAC is 98.2%, which is much higher than that of Pd_1 SAC, and has long-term stability. DFT calculations show that the intrinsic reason for the high activity of Pd_2 DAC is the electron transfer between Pd atoms at the dual Pd site. Therefore, the adsorption strength of Pd_2 DAC for CO* is moderate, which is conducive to the generation of CO in CO_2RR.

In addition, the mesoporous graphite-carbon nitride (mpg-C_3N_4) supported dual-atom Pt_2 catalyst was successfully prepared by wet chemical method (Fig. 16(a)), which showed good catalytic performance for highly selective hydrogenation of nitrobenzene to aniline [222]. As shown in Fig. 16(b), the conversion of > 99% is significantly better than that of mpg-C_3N_4 supported single Pt atom and ultra-small Pt nanoparticles. First-principles calculations show that the excellent and unique catalytic performance of Pt_2 catalyst is due to the H_2 dissociation induced by Pt dual atoms properties and the easy desorption of aniline products.

For non-noble metals, Kim et al. synthesized Co-based atom site catalyst with Co_2–N coordination structure and applied it in photodriven CO_2 reduction (Fig. 16(c)) [223]. The obtained CoDAC has the best CO_2RR performance with a selectivity of 65.0% for CH_4, far exceeding Co-based single-atom catalyst (CoSAC) (Fig. 16(d)). The low absorption energy of CO_2 molecules at the SACs site results in the formation of CO rather than hydrocarbons (CH_4, HCOOH, or C_2 products) in conventional SACs. As illustrated in Fig. 16(e), in the DACs system, both C and O atoms in CO_2 molecules can be adsorbed on bimetallic sites at the same time, and form highly stable intermediates with the help of strong hybridization of CO_2 molecules and bimetallic sites. The intrinsic reason for the high activity of CoDAC is that CoDAC has better adsorption strength for CO_2 and CO* intermediates on the active site of dimer Co, which is more favorable for the generation of CH_4. In addition, experimental results and theoretical calculations show that the unique chemical structure of binuclear Ni bridging with N and C atoms (Ni_2–N_4–C_2) determines the electronic properties of the d-states, which is conducive to the optimal adsorption of CO_2 and intermediates in CO_2RR [224]. As shown in Fig. 16(f), the optimized Ni_2–N_4–C_2 had an ideal coordination structure, with a maximum Faraday efficiency of 96.6% at 0.8 V and a TOF value of 4.6 × 10^3 h^{-1} at 1.0 V. In the *CO desorption stage, the free

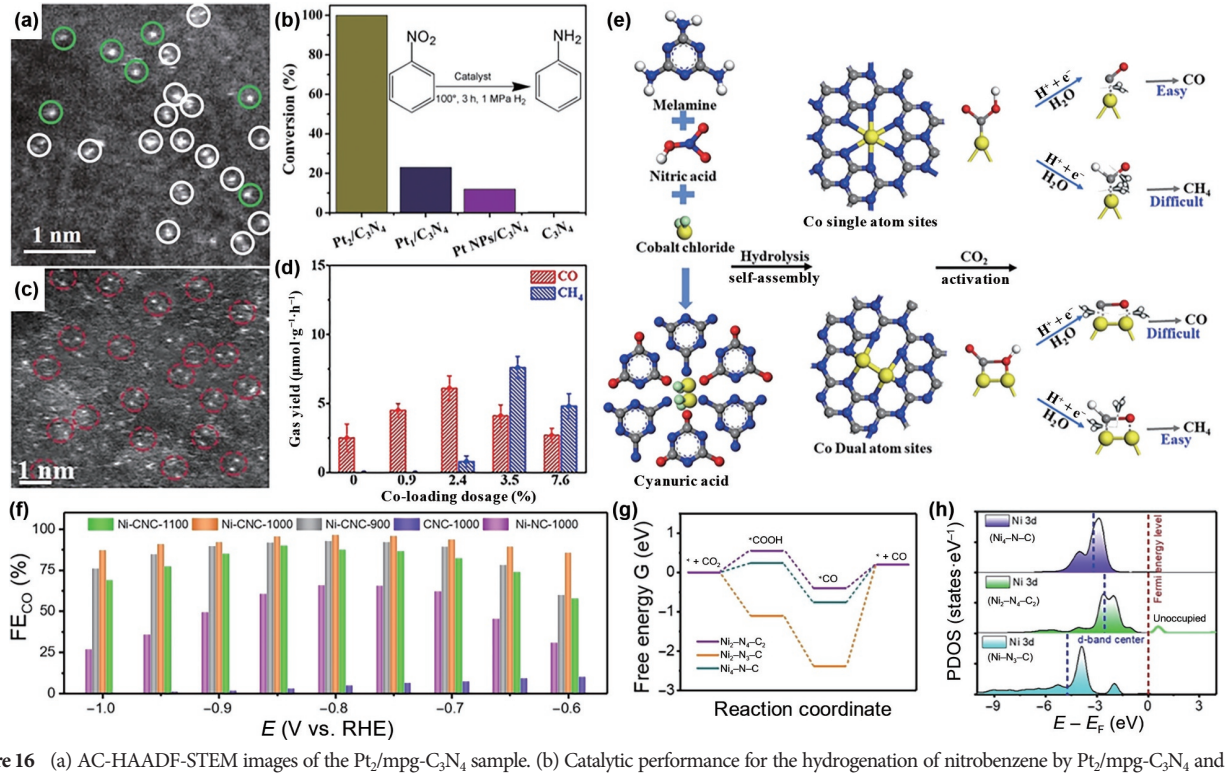

Figure 16 (a) AC-HAADF-STEM images of the Pt_2/mpg-C_3N_4 sample. (b) Catalytic performance for the hydrogenation of nitrobenzene by Pt_2/mpg-C_3N_4 and other reference samples. Reproduced with permission from Ref. [222], © Tian, S. B., et al. 2021. (c) AC-HAADF-STEM images CoDAC-3.5. (d) Photocatalytic CO/CH_4 production rates of Co-based materials with different Co-atom content. (e) Synthesis and CH_4-selective mechanism of CoDAC. Reproduced with permission from Ref. [223], © Wiley-VCH GmbH 2021. (f) FEs of CO at different applied potentials. (g) Free-energy diagram of CO_2RR to CO. (h) PDOS for the Ni 3d orbital over Ni_2–N_4–C_2, Ni–N_3–C and Ni_4–N–C models. Reproduced with permission from Ref. [224], © Wiley-VCH GmbH 2021.

energy gaps of Ni–N_3–C and Ni_4–N–C are 2.59 and 0.97 eV, respectively, which are larger than that of Ni_2–N_4–C_2 (0.60 eV), indicating that the desorption of *CO to CO is thermodynamic more favorable (Fig. 16(g)). The PDOS of the three models show that the d-band center of Ni_2–N_4–C_2 is closest to the Femi energy level (Fig. 16(h)), suggesting that improved adsorption of CO_2 and the presence of unoccupied orbitals appropriately modulate orbital hybridization of the intermediate transition.

For heteronuclear dual-atom pairs, Fu et al. proposed an effective plasma engineering strategy to densely disperse Fe/Co dual atoms on porous nitrogen-doped carbon nanofibers (Fe,Co SA–PNCF) with a mass loading of 9.8% without any acid leaching [198]. The catalyst showed excellent ORR performance in both alkaline and acidic medium. *In situ* XAS showed that when the potential changed from 1.01 to 0.61 V, the Fe and Co K-edge XANES spectra shifted to the lower energy direction, indicating that the oxidation states of Fe and Co decreased during ORR process. In addition, the length of the Co–N bond was slightly elongated from 1.27 to 1.34 Å. The calculated limit potential of Fe, Co SAs-V is 0.89 V, which is higher than that of Fe,Co SAs (0.81 V) and NCF (0.278 V), indicating that Fe,Co SAs-V has higher catalytic activity. According to the d-band center theory, charge can be transferred from the three-dimensional orbitals of TM atoms to the 2p anti-bonding orbitals of oxygen atoms, resulting in electron aggregation and further acceleration of oxygen reduction (Fig. 17(a)). Bu et al. proposed a pre-constrained metal twin strategy to prepare contiguous FeN_4 and CoN_4 DACs with uniform conformation in N-doped graphite carbon (FeCo-DACs/NC) (Figs. 17(b)–17(d)) [225]. A programmable phthalocyanine dimer was used as a structural moiety to anchor the bimetallic sites in MOF to achieve delocalized dispersion prior to pyrolysis. The synthesized FeCo-DACs/NC showed good electrochemical performance in oxygen electrocatalysis, with better onset potential (0.984 V) and half-wave potential (0.877 V). Theoretical calculations show that the synergistic effect of adjacent metals optimizes the d-band center of the metal center, balances the free energy of *O intermediate, and improves the electrocatalytic activity of oxygen. In addition, Lee et al. developed a simple strategy to obtain single-atom-dimer on N-doped carbon (NiCo-SAD–NC) by trapping metal ions *in situ* and then precisely controlling pyrolysis of the N-group [226]. Synergistic effect at the NiCo-SAD atom interface can move the d-band center upward, thus promoting rapid dissociation of water and optimal proton adsorption, accelerating alkaline/acidic HER dynamics. Jiang et al. accurately constructed a novel Fe_1–Ni_1–N–C catalyst modified by Fe and Ni single atom pairs on a nitrogen-doped carbon support through direct pyrolysis of MOFs assembled by Fe and Ni doped ZnO nanoparticles (Fig. 17(e)) [227]. Due to the synergistic effect of adjacent Fe and Ni single-atom pairs, the electrocatalytic reduction of CO_2 by Fe_1–Ni_1–N–C was significantly improved, which was far superior to Fe_1–N–C and Ni_1–N–C with Fe or Ni single atom alone (Fig. 17(f)). Theoretical simulations show that in Fe_1–Ni_1–N–C, a single Fe atom can be activated by a neighboring single Ni atom through non-bonding, significantly promoting the formation of COOH* intermediates and thus globally accelerating the reduction of CO_2. Recently, SACs composed of Fe–N_4 sites have shown encouraging activity due to their lowest cost and extremely high metal utilization [228, 228]. However, the well-defined structure of Fe–N_4 imparts a symmetric electron distribution, resulting in inadequate adsorption energy for oxygen intermediates such as OOH*, O*, and OH* compared to the reference Pt/C catalyst [230]. The adjacent Pt–N_4 site can enhance the catalytic activity of Fe–N_4 group through modulation effect, in which the Pt–N_4 site acts as a modulator to regulate the three-dimensional electron orbital of Fe–N_4 active site and optimize the ORR activity [150, 231]. Fe–N_4/Pt–N_4 dispersed in a nitrogen-doped carbon matrix (Fe–N_4/Pt–N_4@NC) showed a half-wave potential of 0.93 V in 0.1 M KOH, and the active degradation ($\Delta E_{1/2}$ = 8 mV) was negligible after 10,000 cycles.

Based on the parallel theoretical calculation of DFT and machine learning techniques, Huang et al. proposed the Ln–TM DACs system as a candidate for long-term application with high electrical activity and durability [232]. Compared with the highly unstable TM DACs, Ln metals are introduced into SAC to realize the electronic self-balance effect in the Ln–TM DACs system through the f–d coupling effect. Experimentally, they synthesized a series of single-atom and dual-atom catalysts on carbon nitride nanosheets [205]. Syngas with a wide range of CO/H_2 ratios can be produced by adjusting the ratio of La and Zn atomic sites. ZnLa-1/CN electrocatalyst can generate syngas with CO/H_2 = 0.5 in a wide potential range, and the total FE of CO_2RR reaches 80%, indicating good stability. In addition, they revealed the possibility of introducing alkaline/alkaline earth metals, post-transition metals, and metalloids to form stable graphdiyne-based DACs [233]. The main group elements can not only be used as promising separators to increase the loading of DACs, but also activate the alkyl chain to promote the electrical activity. Most importantly, the main group elements do not affect the electrical activity of transition metals or lanthanides, and can even finely modulate the electronic structure.

Loading noble metal single atoms on oxides is an effective method to improve catalytic performance by taking advantage of the synergistic effect of dual-atom sites. The theoretical overpotential of ORR on single-atom Pt has a strong linear relationship with the binding energy of the intermediates and cannot be optimized separately on SACs [234, 235]. However, Zou et al. constructed dispersed Pt–Fe pairs with relatively high activity and stability by loading Pt onto α-Fe_2O_3, and the dual-atom sites of O_2 activation and *OH desorption on the catalyst can go beyond the linear relationship [236]. Under alkaline conditions, the onset potential and half-wave potential of the catalyst are 1.15 and 1.05 V, respectively (Fig. 17(g)), and the mass activity of the catalyst is 14.9 A·mg_{Pt}^{-1} at 0.95 V (Fig. 17(h)). As illustrated in Figs. 17(i) and 17(j), O_2 molecule is adsorbed on single-atom Pt through end-on configuration, the adsorption energy is −0.482 eV, O=O length is extended from 1.23 to 1.31 Å. This indicates that single-atom Pt is not active in O_2 dissociation, resulting in low activity and selectivity. On Pt_1–Fe/Fe_2O_3 (012), the Pt–Fe pair synergically adsorbed O_2 through the side-on configuration, and the adsorption energy increased to −0.832 eV. The O=O of length 1.42 Å promotes the formation of *OOH, and the O=O bond is liable to break. In addition, Pd was also loaded onto α-Fe_2O_3 (012) to construct a highly active and stable Pd–Fe pair for the semi-hydrogenation of alkyne [237]. At 353 and 393 K, the conversion of the catalyst was 99.6% and 100%, and the selectivity was 96.7% and 94.7%, respectively. At 200 h, the catalyst showed good stability and minimal activity attenuation. As shown in Fig. 17(k), the strong electron coupling between Pd and Fe induces a rich d-electron advantage near the Fermi level, indicating that Pd ensembles promote H_2 activation, while Pd single atoms accelerate C–C intermediate desorption. Therefore, Pd–Fe pair can break the balance between catalytic activity and selectivity in semi-hydrogenation. In addition, Li et al. synthesized Ru-SA/H_xMoO_{3-y} hybrids with rich Mo^{n+} species through H-spillover process [238]. The Ru-SA/H_xMoO_{3-y} hybrids can produce NH_3 quantitatively from N_2 and H_2 through the synergistic effect of Ru SA and Mo^{n+}. Ru SA promotes the activation and migration of H_2, and Mo^{n+} acts as the trapping site of localized electrons and the dissociation point of N_2. Finally, NH_3 is synthesized on Mo^{n+}–OH. The formation rate of NH_3 is as high as 4.0 mmol·h^{-1}·g^{-1}, and the apparent

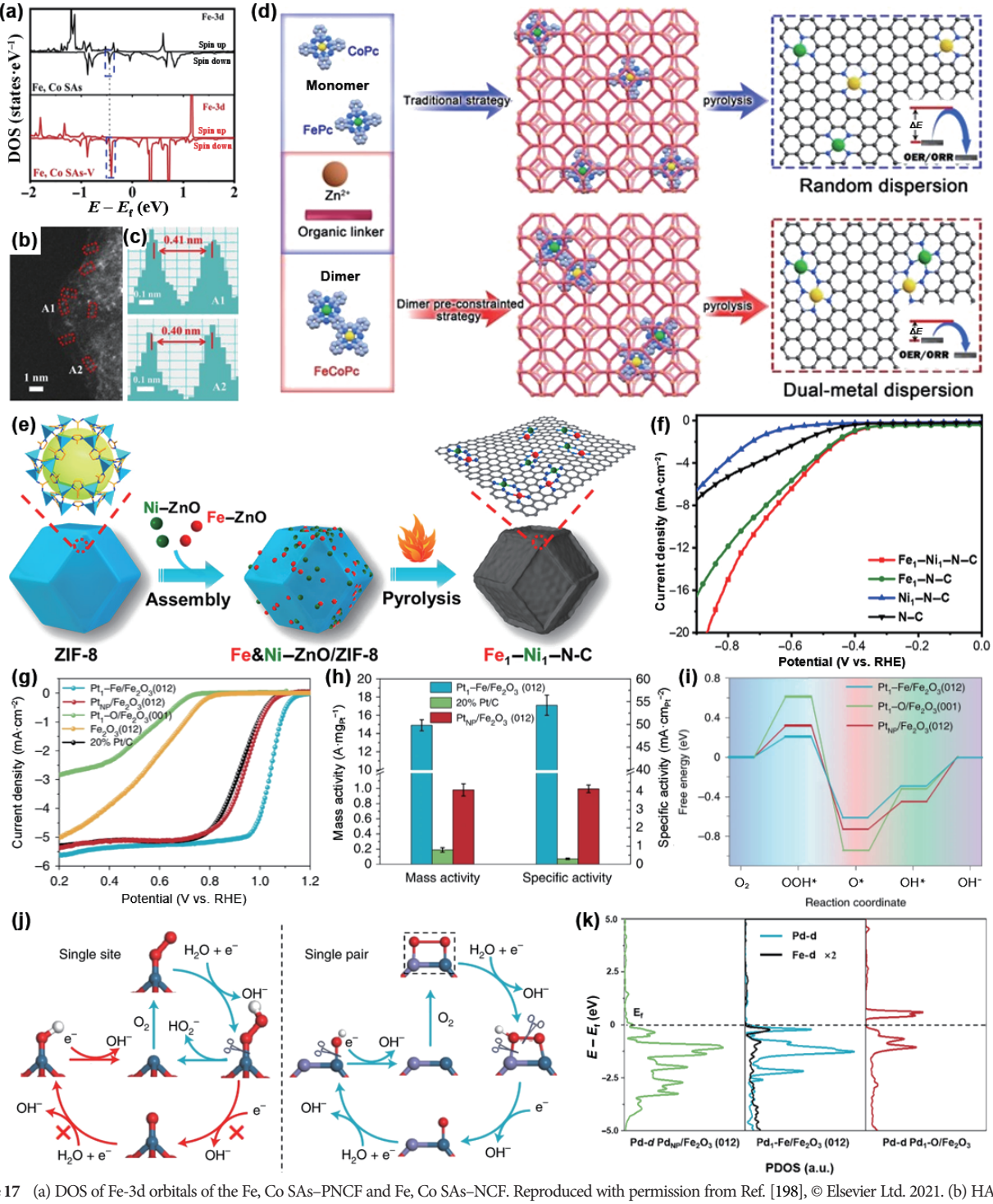

Figure 17 (a) DOS of Fe-3d orbitals of the Fe, Co SAs–PNCF and Fe, Co SAs–NCF. Reproduced with permission from Ref. [198], © Elsevier Ltd. 2021. (b) HAADF-STEM images of FeCo-DACs/NC. (c) Intensity profiles obtained for two metals. (d) Schematic illustration of the traditional strategy and "pre-constrained metal twins" strategy for fabricating DACs. Reproduced with permission from Ref. [225], © Wiley-VCH GmbH 2022. (e) Schematic illustration for construction of Fe_1–Ni_1–N–C with neighboring Fe and Ni single-atoms based on ZIF-8. (f) LSV tests for Fe_1–Ni_1–N–C, Fe_1–N–C, Ni_1–N–C, and N–C in 0.5 M $KHCO_3$. Reproduced with permission from Ref. [227], © American Chemical Society 2021. (g) Oxygen reduction reaction polarization curves with a scanning rate of 5 $mV·s^{-1}$ at a rotating speed of 1,600 r.p.m. (h) A comparison of mass activity and specific activity at 0.95 V. (i) Gibbs free energy diagram of ORR. (j) The proposed ORR mechanism on single-site platinum and Pt–Fe pairs (violet, iron; red, oxygen; dark blue, platinum; white, hydrogen). Reproduced with permission from Ref. [236], © Gao, R. J. et al. 2021. (k) PDOS for the total d orbitals of Pd and Fe. Reproduced with permission from Ref. [237], © American Chemical Society 2021.

quantum efficiency exceeds 6.0% at 650 nm.

4.4 Synergistic effect of multiatom

When atomic catalysts are extended to DACs with two metal atoms as active sites, it is easy to think of further extensions to trinary-atom catalysts with three atoms as active sites. TACs have the smallest hollow site and the adsorption conditions can be further expanded. In addition, the three metal atoms can form different shapes, such as linear, triangular, or other three-dimensional structures, further increasing the flexibility of the active site.

Li et al. prepared homogeneous Ru_3 clusters by a cage-separated precursor preselection and pyrolysis strategy (Figs. 18(a) and 18(b)) [239]. It was found that Ru_3/CN had good catalytic activity (conversion rate 100%), high chemical selectivity (conversion rate 100% for 2-aminobenzaldehyde), and remarkably high TOF

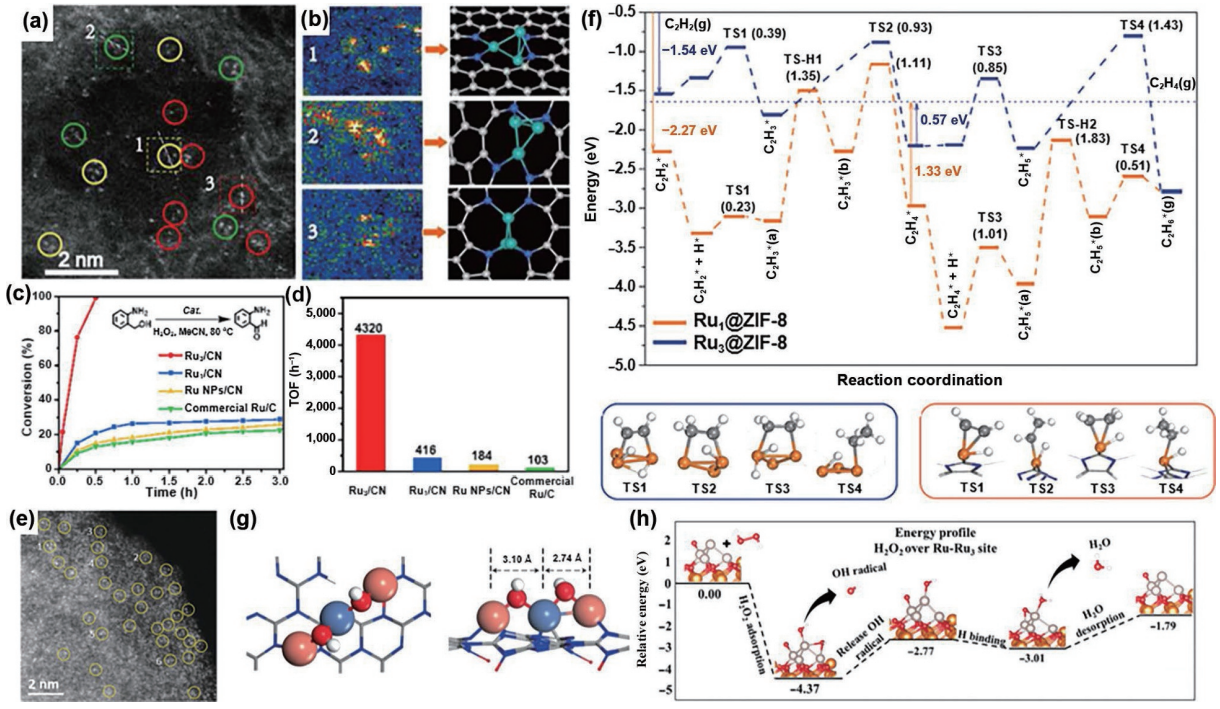

Figure 18 (a) AC-HAADF-STEM images of Ru_3/CN. (b) Corresponding intensity maps (left) and models (right) and (f) intensity profiles obtained in areas labeled 1, 2, and 3 in (a). (c) Conversion (%) of 2-aminobenzyl alcohol vs time for Ru_3/CN (red), Ru_1/CN (blue), Ru NPs/CN (yellow), and commercial Ru/C (green). The inset shows the scheme of oxidation of 2-aminobenzyl alcohol to 2-aminobenzaldehyde. (d) Corresponding TOFs obtained at 20% conversion of 2-aminobenzyl alcohol. Reproduced with permission from Ref. [239], © American Chemical Society 2017. (e) AC-HAADF-STEM images of Ru_3@ZIF-8. (f) Step-by-step hydrogenation mechanism of acetylene to ethane on the Ru_1@ZIF-8 and Ru_3@ZIF-8. Structures of transition states of C_2H_2 hydrogenation on Ru_3@ZIF-8 (blue line) and Ru_1@ZIF-8 (yellow line). Ru orange, C gray, H white. Reproduced with permission from Ref. [240], © Wiley-VCH Verlag GmbH & Co. KGaA, Weinheim 2019. (g) Top view (left), side view (middle) and charge density difference (right) of the DFT-optimized structures of Ni_1Cu_2/g-C_3N_4 after reduction, where the Cu–Ni distances are highlighted. The orange, cyan, red and white balls denote copper, nickel, oxygen and hydrogen atoms, respectively. Reproduced with permission from Ref. [242], © Gu, J., et al. 2021. (h) Energy profiles for H_2O_2 reduction over Ru–Ru_3 site, computed by DFT. Orange for Mg, red for O, and white for H. Reproduced with permission from Ref. [244], © Wiley-VCH GmbH 2021.

(4,320 h^{-1}), which was superior to single-atom and small particle Ru catalysts (Figs. 18(c) and 18(d)). First-principles calculations show that the difference in their TOFs is due to a change in the bonding mode between reactant molecules and Ru species. Of the various adsorption configurations, those that bind only by the amino group are not expected to be effective because in aerobic oxidation, the amino group acts as a bystander and needs to be kept away from the active site. On Ru_1/CN, this structure is 0.58 eV more stable than the one bound by hydroxyl groups, which means that the reactants are more inclined to adopt invalid configurations, blocking the active site of Ru_1. In contrast, on Ru_3/CN, the reactants can take a different geometry, in which a Ru atom is linked to both hydroxyl and amino groups. The adsorption energy of this configuration is close to that of the invalid configuration and is also efficient for the reaction. In addition, single Ru and triatomic Ru_3 clusters are constructed and sealed in functionalized ZIF-8 (Ru_1@ZIF-8, Ru_3@ZIF-8) by cage-controlled encapsulation and reduction strategies (Fig. 18(e)) [240]. Ru_3@ZIF-8 showed good catalytic activity in the semi-hydrogenation of phenylacetylene with a conversion rate of 360 h^{-1} and 97% chemical selectivity to styrene. At Ru_3@ZIF-8, the desorption energy of C_2H_4 at 500 K is 0.57 eV, which is smaller than its further hydrogenation barrier (0.85 eV), indicating that ethylene tends to desorption rather than further hydrogenation in the subsequent process. As shown in Fig. 18(f), at Ru_1@ZIF-8, the potential barrier for further hydrogenation of C_2H_4 to C_2H_5 is 1.01 eV, which is lower than the desorption energy of C_2H_4 (1.33 eV). In addition, the effective barrier of Ru_1@ZIF-8 catalyst is much larger than that of Ru_3@ZIF-8 (2.17 vs. 1.43 eV) during the entire hydrogenation process. In addition, Ma et al. reported an atomically dispersed and fully exposed Cu_3 cluster stabilized on a defective-rich nanodiamond–graphene hybrid support (Cu_3/ND@G) [241]. The catalytic rate constant Cu_3/ND@G (K_{cat} = 1.474 × 10^{-1} s^{-1}) is higher than previously reported single-atom copper oxidase mimics (0.5 × 10^{-3} s^{-1}) and even commercial Pt/C mimics (1.01 × 10^{-2} s^{-1}). DFT calculation shows that Cu_3 clusters provide adjacent adsorption sites during O_2 adsorption process, which promotes the adsorption and dissociation of O_2, and the adsorption energy is −1.64 eV.

For heteronuclear trinary atoms, Lu et al. produced high-loading atomic Ni (3.1 wt.%) and dense atomic Cu grippers (8.1 wt.%) on graphite carbon nitride support through synergistic metal–support interaction and spatial constraints [242]. As shown in Fig. 18(g), the Ni–Cu complex has been identified as a chained Cu–OH–Ni–OH–Cu structure. The Ni atoms bond to the N_{py} and C atoms of g-C_3N_4 and are bounded by the Cu atom on both sides by bridging the OH group. Cu atom is further anchored to g-C_3N_4 by a strong Cu–N_{py} bond. The formation of linear trimer Ni_1Cu_2 is energetically favorable, exothermic by 0.79 eV. The active site is highly adaptable to both reactant adsorption and product desorption, resulting in improved catalyst activity (11 times higher than traditional Ni_1/g-C_3N_4 catalyst) and ethylene selectivity. The dynamics of the Ni atom not only ensures a simple structural shift that facilitates acetylene adsorption by breaking the Ni–N/C bond, but also ensures high chemical/thermal stability without aggregation of catalysts. Compared with the sequential high hydrogenation barrier of 1.38 eV from ethylene to ethane, the weakly bonded ethylene with 0.67 eV increases the ethylene desorption rate, which is a key step for the high selectivity of Ni_1Cu_2/g-C_3N_4.

Single-atom nanozymes (SAzymes) still show OH radical mediated pathway like most traditional nanozymes. Since the

electron density at the center of these metals is strongly influenced by their local coordination, they tend to be positively charged due to negatively charged oxygen/nitrogen chelations [42, 243]. This may reduce the active site of the reduction reaction. Clusters of metal-like chemical states of Ru can greatly promote reductive formation of metallic carbonyl groups, thus providing better atomic efficiency than their single-atom counterparts [244]. For samples with low Ru concentration (0.36 wt.%), the Ru atom on MgO is surrounded by three O atoms and one Mg atom at distances of about 2 and 2.7 Å, respectively. Ru clusters grow at high Ru concentration. $Ru–O_3$ configuration of positively charged single atom (+1.25 |e|) not only hinders the reduction of H_2O_2, but also the desorption of product (H_2O), leading to a lower peroxidase activity. Instead, these two steps in $Ru–Ru_3$ configuration on Ru atomic clusters can be promoted, with a Bader charge near 0 |e| (Fig. 18(h)).

5 Summary and prospect

With the development of single-atom catalysts, it is increasingly important to understand the structure–performance relationship of catalysts at atomic scale. In this paper, we have systematically discussed the fundamental factors affecting the catalytic active sites and try to reveal how to rationally design catalysts at atomic scale by using these descriptors. We have discussed the coordination effects of active sites, including coordination number, atoms and structure, chemical bonds at the active sites, spacing of active atoms, and the synergistic effect of atoms on catalytic performance. We have demonstrated that the binding structure and electronic structure of the active sites have a significant effect on the activity and selectivity of the catalyst through typical examples. Based on the above discussion, we can reasonably design the catalysts required for the target reaction at the atomic scale according to the following points (Fig. 19):

(1) When carbon-based materials are used as the support, the coordination effect of metal active center has a significant influence on the catalytic performance. On the one hand, the change of the coordination number of coordination atoms, namely the value of x and y in $M–N_xC_y$ structure, can break the symmetry of the active site, change the valence state of metal atoms, and increase the chance of substrate adsorption. Among them, the catalytic performance may be improved by designing

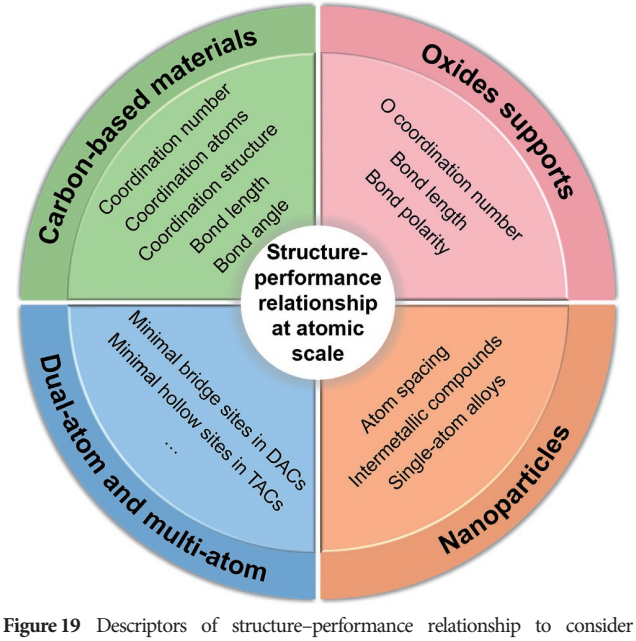

Figure 19 Descriptors of structure–performance relationship to consider when designing different types of catalysts at atomic scale.

coordination vacancy in the supports. On the other hand, doping by different atoms can not only capture isolated metal atoms, but also effectively adjust the electronic structure of metal centers, resulting in the redistribution of charge density and change of catalytic performance. Even if the coordination structure is the same, different N properties will cause the central metal to exhibit different catalytic behaviors. Other coordination atoms with lone electron pairs, such as N, P, S, Cl, and B with vacant orbitals, are expected to optimize the coordination environment more effectively and provide more possibilities for reactions. In addition, direct coordination, high-shell coordination, or even axial coordination of the doped atoms can change the electronic structure of the central atom. Moreover, the curvature of the carbon-based supports can be adjusted to change the bond length and bond angle between metal atoms and coordination atoms, which affects the position of the d-band center. Therefore, the coordination number, atoms and structure of single atoms on carbon-based materials, as well as the bond length and bond angle of coordination bonds are the descriptors to be considered when designing catalysts.

(2) For the catalysts supported by oxides, the coordination effect between metal single atom and O atom can also be exploited to change the catalytic behaviors. The change of O coordination number can adjust the charge loading at the metal site, thus changing the reactivity. In addition, without changing the coordination structure, changing the bond length or bond polarity between metal and O atoms can change the valence state or electron density of the active atoms, and may also change the local symmetry, thus changing the adsorption behavior. Although the environment of the active site is difficult to adjust due to the strong rigidity of the oxide supports, O coordination number, bond length, and bond polarity are key factors affecting catalytic behaviors.

(3) As for nanoparticle catalysts, some intermetallic compounds have uniform active sites. By adding another metal to bring lattice strain, the spacing of the active metal atoms can be changed, which changes the electronic structure of the catalyst and affects the adsorption of the reactants. When the addition of another metal has little effect on the host metal, the active site is still only composed of the host metal, and the change of catalytic performance can be attributed to the change of the spacing of the active metal atoms. However, when this effect becomes larger, the active site can be composed of two metal atoms together, and the synergistic effect between the two becomes apparent. In addition, changing the atomic spacing of monolayer active metals by doping other atoms is a valuable model for understanding the relationship between atomic spacing and catalytic performance at the atomic scale. Further, if the metal atoms are separated into isolated sites, the interactions between the isolated metal atoms are negligible and single-atom alloys are formed. On the one hand, the host metal can optimize the electronic structure of guest isolated metal atoms, thus changing the activation barrier of the reactant and the binding strength of the intermediates. On the other hand, it is possible that single atoms are not the active sites but are used to regulate the electronic properties of the host metal. Therefore, the synergistic effect in SAAs is more obvious, and even dual-atom sites can be formed. At this point, the adsorption mode of the reactants may change, thus affecting the catalytic performance more significantly. Therefore, for the nanoscale catalyst composed of two metals, the adjustment of atomic spacing at the active site, and the synergistic effect between the two atoms are beneficial to meet the requirements of catalytic activity and selectivity.

(4) Dual-atom catalysts provide a good model for understanding the structure-activity relationship at the atomic scale because they have minimal bridge active sites. DACs are

expected to break the relationship between the adsorption energy of reactants and intermediates, thereby catalyzing more complex reactions. The synergistic effect between two atoms can stabilize the active sites, change the adsorption configuration of reactants and intermediates, thus reducing the reaction energy barrier, optimizing the reaction path, and finally improving the catalytic performance. In addition, the adsorption of reactants becomes more flexible as the number of atoms at the active site increases. Trinary-atom catalysts with minimal hollow sites can form different shapes, such as linear, triangular, or other three-dimensional structures, further increasing the flexibility of the active site. Therefore, the catalytic performance of atomic catalysts with more than one active metal atoms is expected to be improved through the synergistic effect between the atoms.

Researchers have done a lot to explore the structure–performance relationship at the atomic scale, but current research is still limited and faces many challenges:

(1) In the synthesis process, the heterogeneous cavity and defect of the supports make it difficult to form the definite configuration with the ideal atomic site. Moreover, many characterization methods such as XAS reflect the average results of the fine structure of active sites. We can obviously find that in many reports, the coordination number of the active site or the valence state of the metal atom are often not integer, indicating the heterogeneity of the catalytic active site. As a result, metal atoms in different environments often co-exist in a synthetic catalyst. When the active site is not uniform, we should be careful to relate the relationship between structure and performance.

(2) The physical basis for the formation of different coordination environments is not clear, so how to prepare SACs with ideal coordination environments is still challenging. Although many studies have synthesized single atom sites in different coordination environments by controlling calcination temperature or feeding ratio, these synthesis strategies are still subject to trial and error. Due to the lack of research on the formation mechanism of catalytic sites during synthesis, it is difficult to effectively construct catalysts in specific coordination environments.

(3) The stability of SACs is an important part of evaluating catalyst performance. Even though existing preparation methods can guarantee the atomic distribution of metal species, SACs still face the risk of loss, aggregation, or reconstruction of active sites during catalysis, especially when the high temperature and reducing atmosphere in industrial catalysis. Industrial catalysis requires the stability of the catalyst for several months or even years to avoid the economic loss caused by frequent replacement of the catalyst. Therefore, researchers should further explore ingenious synthesis strategies to construct SACs with long-term thermodynamic stability. Furthermore, we should balance the stability and activity of the catalysts, since saturated metal atom coordination does improve the stability of the catalyst, but inevitably at the expense of the intrinsic activity of the catalysts.

(4) With the development of *in situ* and *operando* XAS techniques, it is possible to monitor the changes in the structure and electronic properties of the active sites during catalytic reactions. For many complex catalytic reactions, adsorption of reactants and intermediates and charge transfer can be better characterized by these new techniques. The actual environment of the metal center may be different from that of the *ex situ* characterization, which deserves further study.

Acknowledgements

This work was supported by the National Natural Science Foundation of China (Nos. 22171157, 21871159, and 21890383), Science and Technology Key Project of Guangdong Province of China (No. 2020B010188002), and the National Key R&D Program of China (No. 2018YFA0702003).

References

[1] Studt, F.; Abild-Pedersen, F.; Bligaard, T.; Sørensen, R. Z.; Christensen, C. H.; Nørskov, J. K. Identification of non-precious metal alloy catalysts for selective hydrogenation of acetylene. *Science* **2008**, *320*, 1320–1322.

[2] Abe, H.; Liu, J.; Ariga, K. Catalytic nanoarchitectonics for environmentally compatible energy generation. *Mater. Today* **2016**, *19*, 12–18.

[3] Han, A. L.; Zhou, X. F.; Wang, X. J.; Liu, S.; Xiong, Q. H.; Zhang, Q. H.; Gu, L.; Zhuang, Z. C.; Zhang, W. J.; Li, F. X. et al. One-step synthesis of single-site vanadium substitution in 1T-WS_2 monolayers for enhanced hydrogen evolution catalysis. *Nat. Commun.* **2021**, *12*, 709.

[4] Liu, Y. W.; Wu, X.; Li, Z.; Zhang, J.; Liu, S. X.; Liu, S. J.; Gu, L.; Zheng, L. R.; Li, J.; Wang, D. S. et al. Fabricating polyoxometalates-stabilized single-atom site catalysts in confined space with enhanced activity for alkynes diboration. *Nat. Commun.* **2021**, *12*, 4205.

[5] Zhang, N. Q.; Zhang, X. X.; Kang, Y. K.; Ye, C. L.; Jin, R.; Yan, H.; Lin, R.; Yang, J. R.; Xu, Q.; Wang, Y. et al. A supported Pd_2 dual-atom site catalyst for efficient electrochemical CO_2 reduction. *Angew. Chem., Int. Ed.* **2021**, *133*, 13500–13505.

[6] Li, Z. J.; Wei, W.; Li, H. H.; Li, S. H.; Leng, L. P.; Zhang, M. Y.; Horton, J. H.; Wang, D. S.; Sun, W. W.; Guo, C. M. et al. Low-temperature synthesis of single palladium atoms supported on defective hexagonal boron nitride nanosheet for chemoselective hydrogenation of cinnamaldehyde. *ACS Nano* **2021**, *15*, 10175–10184.

[7] Qin, R. X.; Liu, P. X.; Fu, G.; Zheng, N. F. Strategies for stabilizing atomically dispersed metal catalysts. *Small Methods* **2018**, *2*, 1700286.

[8] Liu, J. Y. Catalysis by supported single metal atoms. *ACS Catal.* **2017**, *7*, 34–59.

[9] Lang, R.; Du, X. R.; Huang, Y. K.; Jiang, X. Z.; Zhang, Q.; Guo, Y. L.; Liu, K. P.; Qiao, B. T.; Wang, A. Q.; Zhang, T. Single-atom catalysts based on the metal-oxide interaction. *Chem. Rev.* **2020**, *120*, 11986–12043.

[10] Yang, J. R.; Li, W. H.; Wang, D. S.; Li, Y. D. Electronic metal–support interaction of single-atom catalysts and applications in electrocatalysis. *Adv. Mater.* **2020**, *32*, 2003300.

[11] Yang, X. F.; Wang, A. Q.; Qiao, B. T.; Li, J.; Liu, J. Y.; Zhang, T. Single-atom catalysts: A new frontier in heterogeneous catalysis. *Acc. Chem. Res.* **2013**, *46*, 1740–1748.

[12] Jeong, H.; Shin, S.; Lee, H. Heterogeneous atomic catalysts overcoming the limitations of single-atom catalysts. *ACS Nano* **2020**, *14*, 14355–14374.

[13] Lu, X. F.; Xia, B. Y.; Zang, S. Q.; Lou, X. W. D. Metal-organic frameworks based electrocatalysts for the oxygen reduction reaction. *Angew. Chem., Int. Ed.* **2020**, *59*, 4634–4650.

[14] Wang, X.; Zhang, Y. W.; Wu, J.; Zhang, Z.; Liao, Q. L.; Kang, Z.; Zhang, Y. Single-atom engineering to ignite 2D transition metal dichalcogenide based catalysis: Fundamentals, progress, and beyond. *Chem. Rev.* **2021**, *122*, 1273–1348.

[15] Yang, J. R.; Li, W. H.; Wang, D. S.; Li, Y. D. Single-atom materials: Small structures determine macroproperties. *Small Struct.* **2021**, *2*, 2000051.

[16] Li, R. Z.; Wang, D. S. Superiority of dual-atom catalysts in electrocatalysis: One step further than single-atom catalysts. *Adv. Energy Mater.* **2022**, *12*, 2103564.

[17] Sun, M. Z.; Wong, H. H.; Wu, T.; Dougherty, A. W.; Huang, B. L. Entanglement of spatial and energy segmentation for C_1 pathways in CO_2 reduction on carbon skeleton supported atomic catalysts. *Adv. Energy Mater.* **2022**, *12*, 2103781.

[18] Qiao, B. T.; Wang, A. Q.; Yang, X. F.; Allard, L. F.; Jiang, Z.; Cui, Y. T.; Liu, J. Y.; Li, J.; Zhang, T. Single-atom catalysis of CO

oxidation using Pt_1/FeO_x. *Nat. Chem.* **2011**, *3*, 634–641.
[19] Chen, Y. J.; Ji, S. F.; Chen, C.; Peng, Q.; Wang, D. S.; Li, Y. D. Single-atom catalysts: Synthetic strategies and electrochemical applications. *Joule* **2018**, *2*, 1242–1264.
[20] Chen, S. H.; Li, W. H.; Jiang, W. J.; Yang, J. R.; Zhu, J. X.; Wang, L. Q.; Ou, H. H.; Zhuang, Z. C.; Chen, M. Z.; Sun, X. H. et al. MOF encapsulating N-heterocyclic carbene-ligated copper single-atom site catalyst towards efficient methane electrosynthesis. *Angew. Chem., Int. Ed.* **2021**, *61*, e202114450.
[21] Tian, S. B.; Hu, M.; Xu, Q.; Gong, W. B.; Chen, W. X.; Yang, J. R.; Zhu, Y. Q.; Chen, C.; He, J.; Liu, Q. et al. Single-atom Fe with Fe_1N_3 structure showing superior performances for both hydrogenation and transfer hydrogenation of nitrobenzene. *Sci. China Mater.* **2021**, *64*, 642–650.
[22] Li, W. H.; Yang, J. R.; Jing, H. Y.; Zhang, J.; Wang, Y.; Li, J.; Zhao, J.; Wang, D. S.; Li, Y. D. Creating high regioselectivity by electronic metal–support interaction of a single-atomic-site catalyst. *J. Am. Chem. Soc.* **2021**, *143*, 15453–15461.
[23] Parastaev, A.; Muravev, V.; Osta, E. H.; Van Hoof, A. J. F.; Kimpel, T. F.; Kosinov, N.; Hensen, E. J. M. Boosting CO_2 hydrogenation via size-dependent metal–support interactions in cobalt/ceria-based catalysts. *Nat. Catal.* **2020**, *3*, 526–533.
[24] Liu, Y. W.; Wang, B. X.; Fu, Q.; Liu, W.; Wang, Y.; Gu, L.; Wang, D. S.; Li, Y. D. Polyoxometalate-based metal-organic framework as molecular sieve for highly selective semi-hydrogenation of acetylene on isolated single Pd atom sites. *Angew. Chem., Int. Ed.* **2021**, *60*, 22522–22528.
[25] Cui, T. T.; Ma, L. N.; Wang, S. B.; Ye, C. L.; Liang, X.; Zhang, Z. D.; Meng, G.; Zheng, L. R.; Hu, H. S.; Zhang, J. W. et al. Atomically dispersed $Pt\text{-}N_3C_1$ sites enabling efficient and selective electrocatalytic C–C bond cleavage in lignin models under ambient conditions. *J. Am. Chem. Soc.* **2021**, *143*, 9429–9439.
[26] Han, Y. H.; Dai, J.; Xu, R. R.; Ai, W. Y.; Zheng, L. R.; Wang, Y.; Yan, W. S.; Chen, W. X.; Luo, J.; Liu, Q. et al. Notched-polyoxometalate strategy to fabricate atomically dispersed Ru catalysts for biomass conversion. *ACS Catal.* **2021**, *11*, 2669–2675.
[27] Ren, C. J.; Wen, L.; Magagula, S.; Jiang, Q. Y.; Lin, W.; Zhang, Y. F.; Chen, Z. F.; Ding, K. N. Relative efficacy of $Co\text{-}X_4$ embedded graphene (X = N, S, B, and P) electrocatalysts towards hydrogen evolution reaction: Is nitrogen really the best choice? *ChemCatChem* **2020**, *12*, 536–543.
[28] Yang, J. R.; Li, W. H.; Tan, S. D.; Xu, K. N.; Wang, Y.; Wang, D. S.; Li, Y. D. The electronic metal–support interaction directing the design of single atomic site catalysts: Achieving high efficiency towards hydrogen evolution. *Angew. Chem., Int. Ed.* **2021**, *60*, 19085–19091.
[29] Zhang, N. Q.; Zhang, X. X.; Tao, L.; Jiang, P.; Ye, C. L.; Lin, R.; Huang, Z. W.; Li, A.; Pang, D. W.; Yan, H. et al. Silver single-atom catalyst for efficient electrochemical CO_2 reduction synthesized from thermal transformation and surface reconstruction. *Angew. Chem., Int. Ed.* **2021**, *60*, 6170–6176.
[30] Zhuang, Z. C.; Kang, Q.; Wang, D. S.; Li, Y. D. Single-atom catalysis enables long-life, high-energy lithium-sulfur batteries. *Nano Res.* **2020**, *13*, 1856–1866.
[31] Wang, Y.; Wang, D. S.; Li, Y. D. Rational design of single-atom site electrocatalysts: From theoretical understandings to practical applications. *Adv. Mater.* **2021**, *33*, 2008151.
[32] Zheng, X. B.; Li, P.; Dou, S. X.; Sun, W. P.; Pan, H. G.; Wang, D. S.; Li, Y. D. Non-carbon-supported single-atom site catalysts for electrocatalysis. *Energy Environ. Sci.* **2021**, *14*, 2809–2858.
[33] Li, W. H.; Yang, J. R.; Wang, D. S.; Li, Y. D. Striding the threshold of an atom era of organic synthesis by single-atom catalysis. *Chem* **2022**, *8*, 119–140.
[34] Liu, Z. H.; Du, Y.; Zhang, P. F.; Zhuang, Z. C.; Wang, D. S. Bringing catalytic order out of chaos with nitrogen-doped ordered mesoporous carbon. *Matter* **2021**, *4*, 3161–3194.
[35] Huang, H. W.; Jung, H.; Li, S. F.; Kim, S.; Han, J. W.; Lee, J. Activation of inert copper for significantly enhanced hydrogen evolution behaviors by trace ruthenium doping. *Nano Energy* **2022**, *92*, 106763.
[36] Zhang, E. H.; Tao, L.; An, J. K.; Zhang, J. W.; Meng, L. Z.; Zheng, X. B.; Wang, Y.; Li, N.; Du, S. X.; Zhang, J. T. et al. Engineering the local atomic environments of indium single-atom catalysts for efficient electrochemical production of hydrogen peroxide. *Angew. Chem., Int. Ed.* **2022**, *61*, e202117347.
[37] Jiang, Z. L.; Sun, W. M.; Shang, H. S.; Chen, W. X.; Sun, T. T.; Li, H. J.; Dong, J. C.; Zhou, J.; Li, Z.; Wang, Y. et al. Atomic interface effect of a single atom copper catalyst for enhanced oxygen reduction reactions. *Energy Environ. Sci.* **2019**, *12*, 3508–3514.
[38] Yuan, K.; Lützenkirchen-Hecht, D.; Li, L. B.; Shuai, L.; Li, Y. Z.; Cao, R.; Qiu, M.; Zhuang, X. D.; Leung, M. K. H.; Chen, Y. W. et al. Boosting oxygen reduction of single iron active sites via geometric and electronic engineering: Nitrogen and phosphorus dual coordination. *J. Am. Chem. Soc.* **2020**, *142*, 2404–2412.
[39] Chen, W. M.; Jin, H. Q.; He, F.; Cui, P. X.; Cao, C. Y.; Song, W. G. Dynamic evolution of nitrogen and oxygen dual-coordinated single atomic copper catalyst during partial oxidation of benzene to phenol. *Nano Res.* **2022**, *15*, 3017–3025.
[40] Huang, Q. E.; Wang, B. L.; Ye, S.; Liu, H.; Chi, H. B.; Liu, X. Y.; Fan, H. J.; Li, M. R.; Ding, C. M.; Li, Z. et al. Relation between water oxidation activity and coordination environment of C, N-coordinated mononuclear Co catalyst. *ACS Catal.* **2021**, *12*, 491–496.
[41] Li, M.; Wang, M. M.; Liu, D. Y.; Pan, Y.; Liu, S. J.; Sun, K. A.; Chen, Y. J.; Zhu, H. Y.; Guo, W. Y.; Li, Y. P. et al. Atomically-dispersed NiN_4-Cl active sites with axial Ni-Cl coordination for accelerating electrocatalytic hydrogen evolution. *J. Mater. Chem. A* **2022**, *10*, 6007–6015.
[42] Li, X. Y.; Rong, H. P.; Zhang, J. T.; Wang, D. S.; Li, Y. D. Modulating the local coordination environment of single-atom catalysts for enhanced catalytic performance. *Nano Res.* **2020**, *13*, 1842–1855.
[43] Huang, Y. S.; Li, K.; Yang, G. H.; Aboud, M. F. A.; Shakir, I.; Xu, Y. X. Ultrathin nitrogen-doped carbon layer uniformly supported on graphene frameworks as ultrahigh-capacity anode for lithium-ion full battery. *Small* **2018**, *14*, 1703969.
[44] Peng, H.; Ma, G. F.; Sun, K. J.; Zhang, Z. G.; Yang, Q.; Ran, F. T.; Lei, Z. Q. A facile and rapid preparation of highly crumpled nitrogen-doped graphene-like nanosheets for high-performance supercapacitors. *J. Mater. Chem. A* **2015**, *3*, 13210–13214.
[45] Zhou, D. D.; Li, W. Y.; Dong, X. L.; Wang, Y. G.; Wang, C. X.; Xia, Y. Y. A nitrogen-doped ordered mesoporous carbon nanofiber array for supercapacitors. *J. Mater. Chem. A* **2013**, *1*, 8488–8496.
[46] Yang, M.; Zhou, Z. Recent breakthroughs in supercapacitors boosted by nitrogen-rich porous carbon materials. *Adv. Sci.* **2017**, *4*, 1600408.
[47] Cheong, W. C.; Yang, W. J.; Zhang, J.; Li, Y.; Zhao, D.; Liu, S. J.; Wu, K. L.; Liu, Q. G.; Zhang, C.; Wang, D. S. et al. Isolated iron single-atomic site-catalyzed chemoselective transfer hydrogenation of nitroarenes to arylamines. *ACS Appl. Mater. Interfaces* **2019**, *11*, 33819–33824.
[48] Zhang, H. N.; Li, J.; Xi, S. B.; Du, Y. H.; Hai, X.; Wang, J. Y.; Xu, H. M.; Wu, G.; Zhang, J.; Lu, J. et al. A graphene-supported single-atom FeN_5 catalytic site for efficient electrochemical CO_2 Reduction. *Angew. Chem., Int. Ed.* **2019**, *58*, 14871–14876.
[49] Jing, H. Y.; Zhu, P.; Zheng, X. B.; Zhang, Z. D.; Wang, D. S.; Li, Y. D. Theory-oriented screening and discovery of advanced energy transformation materials in electrocatalysis. *Adv. Powder Mater.* **2022**, *1*, 100013.
[50] Wang, Y.; Zheng, X. B.; Wang, D. S. Design concept for electrocatalysts. *Nano Res.* **2021**, *15*, 1730–1752.
[51] He, Y. H.; Shi, Q. R.; Shan, W. T.; Li, X.; Kropf, A. J.; Wegener, E. C.; Wright, J.; Karakalos, S.; Su, D.; Cullen, D. A. et al. Dynamically unveiling metal-nitrogen coordination during thermal activation to design high-efficient atomically dispersed CoN_4 active sites. *Angew. Chem., Int. Ed.* **2021**, *60*, 9516–9526.
[52] Liu, D. B.; Li, X. Y.; Chen, S. M.; Yan, H.; Wang, C. D.; Wu, C. Q.; Haleem, Y. A.; Duan, S.; Lu, J. L.; Ge, B. H. et al. Atomically dispersed platinum supported on curved carbon supports for efficient electrocatalytic hydrogen evolution. *Nat. Energy* **2019**, *4*, 512–518.
[53] Wang, X. L.; Xiao, H.; Li, A.; Li, Z.; Liu, S. J.; Zhang, Q. H.;

Gong, Y.; Zheng, L. R.; Zhu, Y. Q.; Chen, C. et al. Constructing $NiCo/Fe_3O_4$ heteroparticles within MOF-74 for efficient oxygen evolution reactions. *J. Am. Chem. Soc.* **2018**, *140*, 15336–15341.

[54] Ye, C. L. ; Peng, M. ; Cui, T. T. ; Tang, X. X. ; Wang, D. S. ; Jiao, M. L. ; Miller, J. T. ; Li, Y. D. Revealing the surface atomic arrangement of noble metal alkane dehydrogenation catalysts by a stepwise reduction-oxidation approach. *Nano Res.*, in press, https://doi.org/10.1007/s12274-021-3636-0.

[55] Mohd Adli, N.; Shan, W. T.; Hwang, S.; Samarakoon, W.; Karakalos, S.; Li, Y.; Cullen, D. A.; Su, D.; Feng, Z. X.; Wang, G. F. et al. Engineering atomically dispersed FeN_4 active sites for CO_2 electroreduction. *Angew. Chem., Int. Ed.* **2021**, *60*, 1022–1032.

[56] Yang, J.; Wang, Z. Y.; Huang, C. X.; Zhang, Y. D.; Zhang, Q. H.; Chen, C.; Du, J. Y.; Zhou, X.; Zhang, Y.; Zhou, H. et al. Compressive strain modulation of single iron sites on helical carbon support boosts electrocatalytic oxygen reduction. *Angew. Chem., Int. Ed.* **2021**, *60*, 22722–22728.

[57] Li, H. J.; Li, Y. D.; Koper, M. T. M.; Calle-Vallejo, F. Bond-making and breaking between carbon, nitrogen, and oxygen in electrocatalysis. *J. Am. Chem. Soc.* **2014**, *136*, 15694–15701.

[58] Sun, G. D.; Zhao, Z. J.; Mu, R. T.; Zha, S.; Li, L. L.; Chen, S.; Zang, K. T.; Luo, J.; Li, Z. L.; Purdy, S. C. et al. Breaking the scaling relationship via thermally stable Pt/Cu single atom alloys for catalytic dehydrogenation. *Nat. Commun.* **2018**, *9*, 4454.

[59] Calle-Vallejo, F.; Loffreda, D.; Koper, M. T. M.; Sautet, P. Introducing structural sensitivity into adsorption-energy scaling relations by means of coordination numbers. *Nat. Chem.* **2015**, *7*, 403–410.

[60] Hong, X.; Chan, K.; Tsai, C.; Nørskov, J. K. How doped MoS_2 breaks transition-metal scaling relations for CO_2 electrochemical reduction. *ACS Catal.* **2016**, *6*, 4428–4437.

[61] Hannagan, R. T.; Giannakakis, G.; Flytzani-Stephanopoulos, M.; Sykes, E. C. H. Single-atom alloy catalysis. *Chem. Rev.* **2020**, *120*, 12044–12088.

[62] Li, S. W.; Miao, P.; Zhang, Y. Y.; Wu, J.; Zhang, B.; Du, Y. C.; Han, X. J.; Sun, J. M.; Xu, P. Recent advances in plasmonic nanostructures for enhanced photocatalysis and electrocatalysis. *Adv. Mater.* **2021**, *33*, 2000086.

[63] Wang, Y.; Zheng, M.; Li, Y. R.; Ye, C. L.; Chen, J.; Ye, J. Y.; Zhang, Q. H.; Li, J.; Zhou, Z. Y.; Fu, X. Z. et al. p-d orbital hybridization induced by a monodispersed Ga site on a Pt_3Mn nanocatalyst boosts ethanol electrooxidation. *Angew. Chem., Int. Ed.* **2022**, *61*, e202115735.

[64] Hou, C. C.; Wang, H. F.; Li, C.; Xu, Q. From metal-organic frameworks to single/dual-atom and cluster metal catalysts for energy applications. *Energy Environ. Sci.* **2020**, *13*, 1658–1693.

[65] Liu, M. M.; Wang, L. L.; Zhao, K. N.; Shi, S. S.; Shao, Q. S.; Zhang, L.; Sun, X. L.; Zhao, Y. F.; Zhang, J. J. Atomically dispersed metal catalysts for the oxygen reduction reaction: Synthesis, characterization, reaction mechanisms and electrochemical energy applications. *Energy Environ. Sci.* **2019**, *12*, 2890–2923.

[66] Zhang, W. Y.; Chao, Y. G.; Zhang, W. S.; Zhou, J. H.; Lv, F.; Wang, K.; Lin, F. X.; Luo, H.; Li, J.; Tong, M. P. et al. Emerging dual-atomic-site catalysts for efficient energy catalysis. *Adv. Mater.* **2021**, *33*, 2102576.

[67] Cui, T. T.; Wang, Y. P.; Ye, T.; Wu, J.; Chen, Z. Q.; Li, J.; Lei, Y. P.; Wang, D. S.; Li, Y. D. Engineering dual single-atom sites on 2D ultrathin N-doped carbon nanosheets attaining ultra-low-temperature zinc-air battery. *Angew. Chem., Int. Ed.* **2022**, *134*, e202115219.

[68] Li, R. Z.; Luo, L.; Ma, X. L.; Wu, W. L.; Wang, M. L.; Zeng, J. Single atoms supported on metal oxides for energy catalysis. *J. Mater. Chem. A* **2022**, *10*, 5717–5742.

[69] Ji, S. F.; Jiang, B.; Hao, H. G.; Chen, Y. J.; Dong, J. C.; Mao, Y.; Zhang, Z. D.; Gao, R.; Chen, W. X.; Zhang, R. F. et al. Matching the kinetics of natural enzymes with a single-atom iron nanozyme. *Nat. Catal.* **2021**, *4*, 407–417.

[70] Jia, Y. L.; Xue, Z. Q.; Yang, J.; Liu, Q. L.; Xian, J. H.; Zhong, Y. C.; Sun, Y. M.; Zhang, X. X.; Liu, Q. H.; Yao, D. X. et al. Tailoring the electronic structure of an atomically dispersed zinc electrocatalyst: Coordination environment regulation for high selectivity oxygen reduction. *Angew. Chem., Int. Ed.* **2022**, *61*, e202110838.

[71] Han, A. J.; Zhang, J.; Sun, W. M.; Chen, W. X.; Zhang, S. L.; Han, Y. H.; Feng, Q. C.; Zheng, L. R.; Gu, L.; Chen, C. et al. Isolating contiguous Pt atoms and forming Pt-Zn intermetallic nanoparticles to regulate selectivity in 4-nitrophenylacetylene hydrogenation. *Nat. Commun.* **2019**, *10*, 3787.

[72] Qiu, Y. J.; Zhang, J.; Jin, J.; Sun, J. Q.; Tang, H. L.; Chen, Q. Q.; Zhang, Z. D.; Sun, W. M.; Meng, G.; Xu, Q. et al. Construction of Pd-Zn dual sites to enhance the performance for ethanol electro-oxidation reaction. *Nat. Commun.* **2021**, *12*, 5273.

[73] Shang, H. S.; Sun, W. M.; Sui, R.; Pei, J. J.; Zheng, L. R.; Dong, J. C.; Jiang, Z. L.; Zhou, D. N.; Zhuang, Z. B.; Chen, W. X. et al. Engineering isolated $Mn\text{-}N_2C_2$ atomic interface sites for efficient bifunctional oxygen reduction and evolution reaction. *Nano Lett.* **2020**, *20*, 5443–5450.

[74] Xiong, Y.; Sun, W. M.; Xin, P. Y.; Chen, W. X.; Zheng, X. S.; Yan, W. S.; Zheng, L. R.; Dong, J. C.; Zhang, J.; Wang, D. S. et al. Gram-scale synthesis of high-loading single-atomic-site Fe catalysts for effective epoxidation of styrene. *Adv. Mater.* **2020**, *32*, 2000896.

[75] Sun, T. T.; Li, Y. L.; Cui, T. T.; Xu, L. B.; Wang, Y. G.; Chen, W. X.; Zhang, P. P.; Zheng, T. Y.; Fu, X. Z.; Zhang, S. L. et al. Engineering of coordination environment and multiscale structure in single-site copper catalyst for superior electrocatalytic oxygen reduction. *Nano Lett.* **2020**, *20*, 6206–6214.

[76] Li, Q. H.; Li, Z.; Zhang, Q. H.; Zheng, L. R.; Yan, W. S.; Liang, X.; Gu, L.; Chen, C.; Wang, D. S.; Peng, Q. et al. Porous $\gamma\text{-}Fe_2O_3$ nanoparticle decorated with atomically dispersed platinum: Study on atomic site structural change and gas sensor activity evolution. *Nano Res.* **2021**, *14*, 1435–1442.

[77] Li, J. Z.; Li, H.; Xie, W. F.; Li, S. J.; Song, Y. K.; Fan, K.; Lee, J. Y.; Shao, M. F. Flame-assisted synthesis of O-coordinated single-atom catalysts for efficient electrocatalytic oxygen reduction and hydrogen evolution reaction. *Small Methods* **2022**, *6*, 2101324.

[78] Ma, M. Z.; Huang, Z. A.; Doronkin, D. E.; Fa, W. J.; Rao, Z. Q.; Zou, Y. Z.; Wang, R.; Zhong, Y. Q.; Cao, Y. H.; Zhang, R. Y. et al. Ultrahigh surface density of $Co\text{-}N_2C$ single-atom-sites for boosting photocatalytic CO_2 reduction to methanol. *Appl. Catal. B Environ.* **2022**, *300*, 120695.

[79] Wei, S. M.; Jiang, X. X.; He, C. Y.; Wang, S. Y.; Hu, Q.; Chai, X. Y.; Ren, X. Z.; Yang, H. P.; He, C. X. Construction of single-atom copper sites with low coordination number for efficient CO_2 electroreduction to CH_4. *J. Mater. Chem. A* **2022**, *10*, 6187–6192.

[80] Luo, E. G.; Wang, C.; Li, Y.; Wang, X.; Gong, L. Y.; Zhao, T.; Jin, Z.; Ge, J. J.; Liu, C. P.; Xing, W. Accelerated oxygen reduction on Fe/N/C catalysts derived from precisely-designed ZIF precursors. *Nano Res.* **2020**, *13*, 2420–2426.

[81] Tao, L.; Wang, Y. Q.; Zou, Y. Q.; Zhang, N. N.; Zhang, Y. Q.; Wu, Y. J.; Wang, Y. Y.; Chen, R.; Wang, S. Y. Charge transfer modulated activity of carbon-based electrocatalysts. *Adv. Energy Mater.* **2020**, *10*, 1901227.

[82] Wei, S. J.; Li, A.; Liu, J. C.; Li, Z.; Chen, W. X.; Gong, Y.; Zhang, Q. H.; Cheong, W. C.; Wang, Y.; Zheng, L. R. et al. Direct observation of noble metal nanoparticles transforming to thermally stable single atoms. *Nat. Nanotechnol.* **2018**, *13*, 856–861.

[83] Ji, S. F.; Qu, Y.; Wang, T.; Chen, Y. J.; Wang, G. F.; Li, X.; Dong, J. C.; Chen, Q. Y.; Zhang, W. Y.; Zhang, Z. D. et al. Rare-earth single erbium atoms for enhanced photocatalytic CO_2 reduction. *Angew. Chem., Int. Ed.* **2020**, *59*, 10651–10657.

[84] Fu, N. H.; Liang, X.; Li, Z.; Chen, W. X.; Wang, Y.; Zheng, L. R.; Zhang, Q. H.; Chen, C.; Wang, D. S.; Peng, Q. et al. Fabricating Pd isolated single atom sites on C_3N_4/rGO for heterogenization of homogeneous catalysis. *Nano Res.* **2020**, *13*, 947–951.

[85] Zhang, Z. D.; Zhou, M.; Chen, Y. J.; Liu, S. J.; Wang, H. F.; Zhang, J.; Ji, S. F.; Wang, D. S.; Li, Y. D. Pd single-atom monolithic catalyst: Functional 3D structure and unique chemical selectivity in hydrogenation reaction. *Sci. China Mater.* **2021**, *64*,

1919–1929.
[86] Wang, Y. C.; Liu, Y.; Liu, W.; Wu, J.; Li, Q.; Feng, Q. G.; Chen, Z. Y.; Xiong, X.; Wang, D. S.; Lei, Y. P. Regulating the coordination structure of metal single atoms for efficient electrocatalytic CO_2 reduction. *Energy Environ. Sci.* **2020**, *13*, 4609–4624.
[87] Chen, W. X.; Pei, J. J.; He, C. T.; Wan, J. W.; Ren, H. L.; Zhu, Y. Q.; Wang, Y.; Dong, J. C.; Tian, S. B.; Cheong, W. C. et al. Rational design of single molybdenum atoms anchored on N-doped carbon for effective hydrogen evolution reaction. *Angew. Chem., Int. Ed.* **2017**, *56*, 16086–16090.
[88] Ren, Y. J.; Tang, Y.; Zhang, L. L.; Liu, X. Y.; Li, L.; Miao, S.; Sheng Su, D.; Wang, A. Q.; Li, J.; Zhang, T. Unraveling the coordination structure–performance relationship in Pt_1/Fe_2O_3 single-atom catalyst. *Nat. Commun.* **2019**, *10*, 4500.
[89] Sun, T. T.; Xu, L. B.; Wang, D. S.; Li, Y. D. Metal organic frameworks derived single atom catalysts for electrocatalytic energy conversion. *Nano Res.* **2019**, *12*, 2067–2080.
[90] Zhang, N. Q.; Ye, C. L.; Yan, H.; Li, L. C.; He, H.; Wang, D. S.; Li, Y. D. Single-atom site catalysts for environmental catalysis. *Nano Res.* **2020**, *13*, 3165–3182.
[91] Tian, S. B.; Peng, C.; Dong, J. C.; Xu, Q.; Chen, Z.; Zhai, D.; Wang, Y.; Gu, L.; Hu, P.; Duan, H. H. et al. High-loading single-atomic-site silver catalysts with an Ag_1-C_2N_1 structure showing superior performance for epoxidation of styrene. *ACS Catal.* **2021**, *11*, 4946–4954.
[92] Chen, Z.; Chen, Y. J.; Chao, S. L.; Dong, X. B.; Chen, W. X.; Luo, J.; Liu, C. G.; Wang, D. S.; Chen, C.; Li, W. et al. Single-atom Au^I-N_3 Site for acetylene hydrochlorination reaction. *ACS Catal.* **2020**, *10*, 1865–1870.
[93] Chen, Z.; Zhang, Q.; Chen, W. X.; Dong, J. C.; Yao, H. R.; Zhang, X. B.; Tong, X. J.; Wang, D. S.; Peng, Q.; Chen, C. et al. Single-site Au^I catalyst for silane oxidation with water. *Adv. Mater.* **2018**, *30*, 1704720.
[94] Jing, H. Y.; Liu, W.; Zhao, Z. Y.; Zhang, J. W.; Zhu, C.; Shi, Y. T.; Wang, D. S.; Li, Y. D. Electronics and coordination engineering of atomic cobalt trapped by oxygen-driven defects for efficient cathode in solar cells. *Nano Energy* **2021**, *89*, 106365.
[95] Pan, Y.; Chen, Y. J.; Wu, K. L.; Chen, Z.; Liu, S. J.; Cao, X.; Cheong, W. C.; Meng, T.; Luo, J.; Zheng, L. R. et al. Regulating the coordination structure of single-atom Fe-N_xC_y catalytic sites for benzene oxidation. *Nat. Commun.* **2019**, *10*, 4290.
[96] Wang, X. Q.; Chen, Z.; Zhao, X. Y.; Yao, T.; Chen, W. X.; You, R.; Zhao, C. M.; Wu, G.; Wang, J.; Huang, W. X. et al. Regulation of coordination number over single Co sites: Triggering the efficient electroreduction of CO_2. *Angew. Chem., Int. Ed.* **2018**, *57*, 1944–1948.
[97] Gong, Y. N.; Jiao, L.; Qian, Y. Y.; Pan, C. Y.; Zheng, L. R.; Cai, X. C.; Liu, B.; Yu, S. H.; Jiang, H. L. Regulating the coordination environment of MOF-templated single-atom nickel electrocatalysts for boosting CO_2 reduction. *Angew. Chem., Int. Ed.* **2020**, *59*, 2705–2709.
[98] Pan, Y.; Lin, R.; Chen, Y. J.; Liu, S. J.; Zhu, W.; Cao, X.; Chen, W. X.; Wu, K. L.; Cheong, W. C.; Wang, Y. et al. Design of single-atom Co-N_5 catalytic site: A robust electrocatalyst for CO_2 reduction with nearly 100% CO selectivity and remarkable stability. *J. Am. Chem. Soc.* **2018**, *140*, 4218–4221.
[99] Xiong, Y.; Wang, S. B.; Chen, W. X.; Zhang, J.; Li, Q. H.; Hu, H. S.; Zheng, L. R.; Yan, W. S.; Gu, L.; Wang, D. S. et al. Construction of dual-active-site copper catalyst containing both Cu-N_3 and Cu-N_4 sites. *Small* **2021**, *17*, 2006834.
[100] Xiong, Y.; Sun, W. M.; Han, Y. H.; Xin, P. Y.; Zheng, X. S.; Yan, W. S.; Dong, J. C.; Zhang, J.; Wang, D. S.; Li, Y. D. Cobalt single atom site catalysts with ultrahigh metal loading for enhanced aerobic oxidation of ethylbenzene. *Nano Res.* **2021**, *14*, 2418–2423.
[101] Jing, H. Y.; Zhao, Z. Y.; Zhang, J. W.; Zhu, C.; Liu, W.; Li, N. N.; Hao, C.; Shi, Y. T.; Wang, D. S. Atomic evolution of metal-organic frameworks into Co-N_3 coupling vacancies by cooperative cascade protection strategy for promoting triiodide reduction. *J. Phys. Chem. C* **2021**, *125*, 6147–6156.
[102] Gong, H. S.; Wei, Z. X.; Gong, Z. C.; Liu, J. J.; Ye, G. L.; Yan, M. M.; Dong, J. C.; Allen, C.; Liu, J. B.; Huang, K. et al. Low-coordinated Co-N-C on oxygenated graphene for efficient electrocatalytic H_2O_2 production. *Adv. Funct. Mater.* **2022**, *26*, 2106886.
[103] Ding, R.; Chen, Y. W.; Li, X. K.; Rui, Z. Y.; Hua, K.; Wu, Y. K.; Duan, X.; Wang, X. B.; Li, J.; Liu, J. G. Atomically dispersed, low-coordinate Co-N sites on carbon nanotubes as inexpensive and efficient electrocatalysts for hydrogen evolution. *Small* **2022**, *18*, 2105335.
[104] Yan, C. C.; Li, H. B.; Ye, Y. F.; Wu, H. H.; Cai, F.; Si, R.; Xiao, J. P.; Miao, S. H.; Xie, S. H.; Yang, F. et al. Coordinatively unsaturated nickel-nitrogen sites towards selective and high-rate CO_2 electroreduction. *Energy Environ. Sci.* **2018**, *11*, 1204–1210.
[105] Sa, Y. J.; Jung, H.; Shin, D.; Jeong, H. Y.; Ringe, S.; Kim, H.; Hwang, Y. J.; Joo, S. H. Thermal transformation of molecular Ni^{2+}-N_4 sites for enhanced CO_2 electroreduction activity. *ACS Catal.* **2020**, *10*, 10920–10931.
[106] Rong, X.; Wang, H. J.; Lu, X. L.; Si, R.; Lu, T. B. Controlled synthesis of a vacancy-defect single-atom catalyst for boosting CO_2 electroreduction. *Angew. Chem., Int. Ed.* **2020**, *59*, 1961–1965.
[107] Han, Y. H.; Wang, Y. G.; Xu, R. R.; Chen, W. X.; Zheng, L. R.; Han, A. J.; Zhu, Y. Q.; Zhang, J.; Zhang, H. B.; Luo, J. et al. Electronic structure engineering to boost oxygen reduction activity by controlling the coordination of the central metal. *Energy Environ. Sci.* **2018**, *11*, 2348–2352.
[108] Hu, L. Y.; Dai, C. L.; Chen, L. W.; Zhu, Y. H.; Hao, Y. C.; Zhang, Q. H.; Gu, L.; Feng, X.; Yuan, S.; Wang, L. et al. Metal-triazolate-framework-derived FeN_4Cl_1 single-atom catalysts with hierarchical porosity for the oxygen reduction reaction. *Angew. Chem., Int. Ed.* **2021**, *60*, 27324–27329.
[109] Liu, X.; Jiao, Y.; Zheng, Y.; Jaroniec, M.; Qiao, S. Z. Building up a picture of the electrocatalytic nitrogen reduction activity of transition metal single-atom catalysts. *J. Am. Chem. Soc.* **2019**, *141*, 9664–9672.
[110] Zhao, D.; Sun, K. A.; Cheong, W. C.; Zheng, L. R.; Zhang, C.; Liu, S. J.; Cao, X.; Wu, K. L.; Pan, Y.; Zhuang, Z. W. et al. Synergistically interactive pyridinic-N-MoP sites: Identified active centers for enhanced hydrogen evolution in alkaline solution. *Angew. Chem., Int. Ed.* **2020**, *59*, 8982–8990.
[111] Li, J. J.; Jiang, Y. F.; Wang, Q.; Xu, C. Q.; Wu, D. J.; Banis, M. N.; Adair, K. R.; Doyle-Davis, K.; Meira, D. M.; Finfrock, Y. Z. et al. A general strategy for preparing pyrrolic-N_4 type single-atom catalysts via pre-located isolated atoms. *Nat. Commun.* **2021**, *12*, 6806.
[112] Zhu, C. Z.; Fu, S. F.; Song, J. H.; Shi, Q. R.; Su, D.; Engelhard, M. H.; Li, X. L.; Xiao, D. D.; Li, D. S.; Estevez, L. et al. Self-assembled Fe-N-doped carbon nanotube aerogels with single-atom catalyst feature as high-efficiency oxygen reduction electrocatalysts. *Small* **2017**, *13*, 1603407.
[113] Büechele, S.; Chen, Z. P.; Mitchell, S.; Hauert, R.; Krumeich, F.; Pérez-Ramírez, J. Tailoring nitrogen-doped carbons as hosts for single-atom catalysts. *ChemCatChem* **2019**, *11*, 2812–2820.
[114] Wu, G.; Mack, N. H.; Gao, W.; Ma, S. G.; Zhong, R. Q.; Han, J. T.; Baldwin, J. K.; Zelenay, P. Nitrogen-doped graphene-rich catalysts derived from heteroatom polymers for oxygen reduction in nonaqueous lithium-O_2 battery cathodes. *ACS Nano* **2012**, *6*, 9764–9776.
[115] Wu, G.; Santandreu, A.; Kellogg, W.; Gupta, S.; Ogoke, O.; Zhang, H. G.; Wang, H. L.; Dai, L. M. Carbon nanocomposite catalysts for oxygen reduction and evolution reactions: From nitrogen doping to transition-metal addition. *Nano Energy* **2016**, *29*, 83–110.
[116] Lin, S. R.; Xu, H. X.; Wang, Y. K.; Zeng, X. C.; Chen, Z. F. Directly predicting limiting potentials from easily obtainable physical properties of graphene-supported single-atom electrocatalysts by machine learning. *J. Mater. Chem. A* **2020**, *8*, 5663–5670.
[117] Zhao, R.; Peng, H.; Wang, H. L.; Liang, J.; Lv, Y. Y.; Ma, G. F.; Lei, Z. Q. Tuning nitrogen doping types and pore structures in carbon nanosheets as electrodes for supercapacitor by controlling existence form of iron species. *J. Energy Storage* **2020**, *28*, 101174.
[118] Jin, J. Y.; Wang, Z. W.; Wang, R.; Wang, J. L.; Huang, Z. D.; Ma, Y. W.; Li, H.; Wei, S. H.; Huang, X.; Yan, J. X. et al. Achieving

high volumetric lithium storage capacity in compact carbon materials with controllable nitrogen doping. *Adv. Funct. Mater.* **2019**, *29*, 1807441.

[119] Wang, X. R.; Liu, J. Y.; Liu, Z. W.; Wang, W. C.; Luo, J.; Han, X. P.; Du, X. W.; Qiao, S. Z.; Yang, J. Identifying the key role of pyridinic-N–Co bonding in synergistic electrocatalysis for reversible ORR/OER. *Adv. Mater.* **2018**, *30*, 1800005.

[120] Jin, X. X.; Xie, Y.; Fu, J. H.; Zhao, C. Y.; Xu, Y. H.; Lv, Y.; Zhang, B. S.; Sun, K. J.; Si, R.; Huang, J. H. A highly efficient Fe-N-C electrocatalyst with atomically dispersed FeN_4 sites for the oxygen reduction reaction. *ChemCatChem* **2021**, *13*, 2683–2690.

[121] Yang, L.; Cheng, D. J.; Xu, H. X.; Zeng, X. F.; Wan, X.; Shui, J. L.; Xiang, Z. H.; Cao, D. P. Unveiling the high-activity origin of single-atom iron catalysts for oxygen reduction reaction. *Proc. Natl. Acad. Sci. USA* **2018**, *115*, 6626–6631.

[122] Wang, C.; Hu, X.; Hu, X. S.; Liu, X. Y.; Guan, Q. X.; Hao, R.; Liu, Y. P.; Li, W. Typical transition metal single-atom catalysts with a metal-pyridine N structure for efficient CO_2 electroreduction. *Appl. Catal. B Environ.* **2021**, *296*, 120331.

[123] Gu, J.; Hsu, C. S.; Bai, L. C.; Chen, H. M.; Hu, X. L. Atomically dispersed Fe^{3+} sites catalyze efficient CO_2 electroreduction to CO. *Science* **2019**, *364*, 1091–1094.

[124] Zhang, J.; Zheng, C. Y.; Zhang, M. L.; Qiu, Y. J.; Xu, Q.; Cheong, W. C.; Chen, W. X.; Zheng, L. R.; Gu, L.; Hu, Z. P. et al. Controlling N-doping type in carbon to boost single-atom site Cu catalyzed transfer hydrogenation of quinoline. *Nano Res.* **2020**, *13*, 3082–3087.

[125] Zhang, L.; Wang, Q.; Si, R. T.; Song, Z. X.; Lin, X. T.; Banis, M. N.; Adair, K.; Li, J. J.; Doyle-Davis, K.; Li, R. Y. et al. New insight of pyrrole-like nitrogen for boosting hydrogen evolution activity and stability of Pt single atoms. *Small* **2021**, *17*, 2004453.

[126] Fan, M. M.; Cui, J. W.; Wu, J. J.; Vajtai, R.; Sun, D. P.; Ajayan, P. M. Improving the catalytic activity of carbon-supported single atom catalysts by polynary metal or heteroatom doping. *Small* **2020**, *16*, 1906782.

[127] Ramaswamy, N.; Tylus, U.; Jia, Q. Y.; Mukerjee, S. Activity descriptor identification for oxygen reduction on nonprecious electrocatalysts: Linking surface science to coordination chemistry. *J. Am. Chem. Soc.* **2013**, *135*, 15443–15449.

[128] Cabán-Acevedo, M.; Stone, M. L.; Schmidt, J. R.; Thomas, J. G.; Ding, Q.; Chang, H. C.; Tsai, M. L.; He, J. H.; Jin, S. Efficient hydrogen evolution catalysis using ternary pyrite-type cobalt phosphosulphide. *Nat. Mater.* **2015**, *14*, 1245–1251.

[129] Wan, J. W.; Zhao, Z. H.; Shang, H. S.; Peng, B.; Chen, W. X.; Pei, J. J.; Zheng, L. R.; Dong, J. C.; Cao, R.; Sarangi, R. et al. In situ phosphatizing of triphenylphosphine encapsulated within metal-organic frameworks to design atomic Co_1-P_1N_3 interfacial structure for promoting catalytic performance. J. Am. *Chem. Soc.* **2020**, *142*, 8431–8439.

[130] Wei, X.; Zheng, D.; Zhao, M.; Chen, H. Z.; Fan, X.; Gao, B.; Gu, L.; Guo, Y.; Qin, J. B.; Wei, J. et al. Cross-linked polyphosphazene hollow nanosphere-derived N/P-doped porous carbon with single nonprecious metal atoms for the oxygen reduction reaction. *Angew. Chem., Int. Ed.* **2020**, *59*, 14639–14646.

[131] Qiao, Y. Y.; Yuan, P. F.; Hu, Y. F.; Zhang, J. N.; Mu, S. C.; Zhou, J. H.; Li, H.; Xia, H. C.; He, J.; Xu, Q. Sulfuration of an Fe-N-C catalyst containing Fe_xC/Fe species to enhance the catalysis of oxygen reduction in acidic media and for use in flexible Zn-Air batteries. *Adv. Mater.* **2018**, *30*, 1804504.

[132] Yang, H. B.; Miao, J. W.; Hung, S. F.; Chen, J. Z.; Tao, H. B.; Wang, X. Z.; Zhang, L. P.; Chen, R.; Gao, J. J.; Chen, H. M. et al. Identification of catalytic sites for oxygen reduction and oxygen evolution in N-doped graphene materials: Development of highly efficient metal-free bifunctional electrocatalyst. *Sci. Adv.* **2016**, *2*, e1501122.

[133] Ito, Y.; Cong, W. T.; Fujita, T.; Tang, Z.; Chen, M. W. High catalytic activity of nitrogen and sulfur Co-doped nanoporous graphene in the hydrogen evolution reaction. *Angew. Chem., Int. Ed.* **2015**, *54*, 2131–2136.

[134] Shang, H. S.; Zhou, X. Y.; Dong, J. C.; Li, A.; Zhao, X.; Liu, Q. H.; Lin, Y.; Pei, J. J.; Li, Z.; Jiang, Z. L. et al. Engineering unsymmetrically coordinated Cu-S_1N_3 single atom sites with enhanced oxygen reduction activity. *Nat. Commun.* **2020**, *11*, 3049.

[135] Hou, Y.; Qiu, M.; Kim, M. G.; Liu, P.; Nam, G.; Zhang, T.; Zhuang, X. D.; Yang, B.; Cho, J.; Chen, M. W. et al. Atomically dispersed nickel-nitrogen-sulfur species anchored on porous carbon nanosheets for efficient water oxidation. *Nat. Commun.* **2019**, *10*, 1392.

[136] Chen, Y. J.; Gao, R.; Ji, S. F.; Li, H. J.; Tang, K.; Jiang, P.; Hu, H. B.; Zhang, Z. D.; Hao, H. G.; Qu, Q. Y. et al. Atomic-level modulation of electronic density at cobalt single-atom sites derived from metal-organic frameworks: Enhanced oxygen reduction performance. *Angew. Chem., Int. Ed.* **2021**, *60*, 3212–3221.

[137] Jiao, D. X.; Liu, Y. J.; Cai, Q. H.; Zhao, J. X. Coordination tunes the activity and selectivity of the nitrogen reduction reaction on single-atom iron catalysts: A computational study. *J. Mater. Chem. A* **2021**, *9*, 1240–1251.

[138] Guo, Y. Y.; Yuan, P. F.; Zhang, J. N.; Hu, Y. F.; Amiinu, I. S.; Wang, X.; Zhou, J. G.; Xia, H. C.; Song, Z. B.; Xu, Q. et al. Carbon nanosheets containing discrete Co-N_x-B_y-C active sites for efficient oxygen electrocatalysis and rechargeable Zn-Air batteries. *ACS Nano* **2018**, *12*, 1894–1901.

[139] Wang, S. Y.; Sun, M. H.; Zheng, L. R.; Zhou, S. D. On the promising performance of single Ta atom in efficient nitrogen fixation. *Chem Catal.* **2021**, *1*, 1322–1330.

[140] Xu, Q.; Guo, C. X.; Tian, S. B.; Zhang, J.; Chen, W. X.; Cheong, W. C.; Gu, L.; Zheng, L. R.; Xiao, J. P.; Liu, Q. et al. Coordination structure dominated performance of single-atomic Pt catalyst for anti-Markovnikov hydroboration of alkenes. *Sci. China Mater.* **2020**, *63*, 972–981.

[141] Xie, J. F.; Zhao, X. T.; Wu, M. X.; Li, Q. H.; Wang, Y. B.; Yao, J. N. Metal-free fluorine-doped carbon electrocatalyst for CO_2 reduction outcompeting hydrogen evolution. *Angew. Chem., Int. Ed.* **2018**, *57*, 9640–9644.

[142] Shen, H. J.; Gracia-Espino, E.; Ma, J. Y.; Zang, K. T.; Luo, J.; Wang, L.; Gao, S. S.; Mamat, X.; Hu, G. Z.; Wagberg, T. et al. Synergistic effects between atomically dispersed Fe-N-C and C-S-C for the oxygen reduction reaction in acidic media. *Angew. Chem., Int. Ed.* **2017**, *56*, 13800–13804.

[143] Zhang, W.; Mao, K. K.; Zeng, X. C. B-doped MnN_4-G nanosheets as bifunctional electrocatalysts for both oxygen reduction and oxygen evolution reactions.. *ACS Sustainable Chem. Eng.* **2019**, *7*, 18711–18717.

[144] Ji, S. F.; Chen, Y. J.; Zhang, Z. D.; Cheong, W. C.; Liu, Z. R.; Wang, D. S.; Li, Y. D. Single-atomic-site cobalt stabilized on nitrogen and phosphorus co-doped carbon for selective oxidation of primary alcohols. *Nanoscale Horiz.* **2019**, *4*, 902–906.

[145] Sun, X. H.; Tuo, Y.; Ye, C. L.; Chen, C.; Lu, Q.; Li, G. N.; Jiang, P.; Chen, S. H.; Zhu, P.; Ma, M. et al. Phosphorus induced electron localization of single iron sites for boosted CO_2 electroreduction reaction. *Angew. Chem., Int. Ed.* **2021**, *60*, 23614–23618.

[146] Yin, H. B.; Yuan, P. F.; Lu, B. A.; Xia, H. C.; Guo, K.; Yang, G. G.; Qu, G.; Xue, D. P.; Hu, Y. F.; Cheng, J. Q. et al. Phosphorus-driven electron delocalization on edge-type FeN_4 active sites for oxygen reduction in acid medium. *ACS Catal.* **2021**, *11*, 12754–12762.

[147] Li, Q. H.; Chen, W. X.; Xiao, H.; Gong, Y.; Li, Z.; Zheng, L. R.; Zheng, X. S.; Yan, W. S.; Cheong, W. C.; Shen, R. G. et al. Fe isolated single atoms on S, N codoped carbon by copolymer pyrolysis strategy for highly efficient oxygen reduction reaction. *Adv. Mater.* **2018**, *30*, 1800588.

[148] Wu, K. L.; Chen, X.; Liu, S. J.; Pan, Y.; Cheong, W. C.; Zhu, W.; Cao, X.; Shen, R. A.; Chen, W. X.; Luo, J. et al. Porphyrin-like Fe-N_4 sites with sulfur adjustment on hierarchical porous carbon for different rate-determining steps in oxygen reduction reaction. *Nano Res.* **2018**, *11*, 6260–6269.

[149] Yang, L. P.; Zhang, X.; Yu, L. X.; Hou, J. H.; Zhou, Z.; Lv, R. T. Atomic Fe-N_4/C in flexible carbon fiber membrane as binder-free air cathode for Zn-Air batteries with stable cycling over 1000 h. *Adv. Mater.* **2022**, *34*, 2105410.

[150] Chen, Y. J.; Ji, S. F.; Zhao, S.; Chen, W. X.; Dong, J. C.; Cheong, W. C.; Shen, R. G.; Wen, X. D.; Zheng, L. R.; Rykov, A. I. et al. Enhanced oxygen reduction with single-atomic-site iron catalysts for a zinc-air battery and hydrogen-air fuel cell. *Nat. Commun.* **2018**, *9*, 5422.

[151] Wang, H. H.; Lv, L. B.; Zhang, S. N.; Su, H.; Zhai, G. Y.; Lei, W. W.; Li, X. H.; Chen, J. S. Synergy of Fe-N_4 and non-coordinated boron atoms for highly selective oxidation of amine into nitrile. *Nano Res.* **2020**, *13*, 2079–2084.

[152] Jung, E.; Shin, H.; Lee, B. H.; Efremov, V.; Lee, S.; Lee, H. S.; Kim, J.; Hooch Antink, W.; Park, S.; Lee, K. S. et al. Atomic-level tuning of Co-N-C catalyst for high-performance electrochemical H_2O_2 production. *Nat. Mater.* **2020**, *19*, 436–442.

[153] Zhang, X. M.; Zhai, P. L.; Zhang, Y. X.; Wu, Y. Z.; Wang, C.; Ran, L.; Gao, J. F.; Li, Z. W.; Zhang, B.; Fan, Z. Z. et al. Engineering single-atomic Ni-N_4-O sites on semiconductor photoanodes for high-performance photoelectrochemical water splitting. *J. Am. Chem. Soc.* **2021**, *143*, 20657–20669.

[154] Wang, Y.; Tang, Y. J.; Zhou, K. Self-adjusting activity induced by intrinsic reaction intermediate in Fe-N-C single-atom catalysts. *J. Am. Chem. Soc.* **2019**, *141*, 14115–14119.

[155] Li, L. B.; Huang, S. H.; Cao, R.; Yuan, K.; Lu, C. B.; Huang, B. Y.; Tang, X. N.; Hu, T.; Zhuang, X. D.; Chen, Y. W. Optimizing microenvironment of asymmetric N, S-coordinated single-atom Fe via axial fifth coordination toward efficient oxygen electroreduction. *Small* **2022**, *18*, 2105387.

[156] DeRita, L.; Resasco, J.; Dai, S.; Boubnov, A.; Thang, H. V.; Hoffman, A. S.; Ro, I.; Graham, G. W.; Bare, S. R.; Pacchioni, G. et al. Structural evolution of atomically dispersed Pt catalysts dictates reactivity. *Nat. Mater.* **2019**, *18*, 746–751.

[157] Lu, Z.; Liu, X. Y.; Zhang, B.; Gan, Z. R.; Tang, S. W.; Ma, L.; Wu, T. P.; Nelson, G. J.; Qin, Y.; Turner, C. H. et al. Structure and reactivity of single site Ti catalysts for propylene epoxidation. *J. Catal.* **2019**, *377*, 419–428.

[158] Lin, C.; Liu, X. P.; Qu, J. L.; Feng, X.; Seh, Z. W.; Wang, T. S.; Zhang, Q. F. Strain-controlled single Cr-embedded nitrogen-doped graphene achieves efficient nitrogen reduction. *Mater. Adv.* **2021**, *2*, 5704–5711.

[159] Liang, Z. Z.; Kong, N. N.; Yang, C. X.; Zhang, W.; Zheng, H. Q.; Lin, H. P.; Cao, R. Highly curved nanostructure-coated Co, N-doped carbon materials for oxygen electrocatalysis. *Angew. Chem., Int. Ed.* **2021**, *60*, 12759–12764.

[160] Jiang, K.; Luo, M.; Liu, Z. X.; Peng, M.; Chen, D. C.; Lu, Y. R.; Chan, T. S.; De Groot, F. M. F.; Tan, Y. W. Rational strain engineering of single-atom ruthenium on nanoporous MoS_2 for highly efficient hydrogen evolution. *Nat. Commun.* **2021**, *12*, 1687.

[161] Daelman, N.; Capdevila-Cortada, M.; López, N. Dynamic charge and oxidation state of Pt/CeO_2 single-atom catalysts. *Nat. Mater.* **2019**, *18*, 1215–1221.

[162] Jiang, D.; Wan, G.; García-Vargas, C. E.; Li, L. Z.; Pereira-Hernández, X. I.; Wang, C. M.; Wang, Y. Elucidation of the active sites in single-atom Pd_1/CeO_2 catalysts for low-temperature CO oxidation. *ACS Catal.* **2020**, *10*, 11356–11364.

[163] Kunwar, D.; Zhou, S. L.; DeLaRiva, A.; Peterson, E. J.; Xiong, H. F.; Pereira-Hernández, X. I.; Purdy, S. C.; Ter Veen, R.; Brongersma, H. H.; Miller, J. T. et al. Stabilizing high metal loadings of thermally stable platinum single atoms on an industrial catalyst support. *ACS Catal.* **2019**, *9*, 3978–3990.

[164] Jiang, D.; Yao, Y. G.; Li, T. Y.; Wan, G.; Pereira-Hernández, X. I.; Lu, Y. B.; Tian, J. S.; Khivantsev, K.; Engelhard, M. H.; Sun, C. J. et al. Frontispiece: Tailoring the local environment of platinum in single-atom Pt_1/CeO_2 catalysts for robust low-temperature CO oxidation. *Angew. Chem., Int. Ed.* **2021**, *60*, 26054.

[165] Li, J. Z.; Zhang, H. G.; Samarakoon, W.; Shan, W. T.; Cullen, D. A.; Karakalos, S.; Chen, M. J.; Gu, D. M.; More, K. L.; Wang, G. F. et al. Thermally driven structure and performance evolution of atomically dispersed FeN_4 sites for oxygen reduction. *Angew. Chem., Int. Ed.* **2019**, *58*, 18971–18980.

[166] Meng, G.; Sun, W. M.; Mon, A. A.; Wu, X.; Xia, L. Y.; Han, A. J.; Wang, Y.; Zhuang, Z. B.; Liu, J. F.; Wang, D. S. et al. Strain regulation to optimize the acidic water oxidation performance of atomic-layer IrO_x. *Adv. Mater.* **2019**, *31*, 1903616.

[167] Jiang, Z. L.; Wang, T.; Pei, J. J.; Shang, H. S.; Zhou, D. N.; Li, H. J.; Dong, J. C.; Wang, Y.; Cao, R.; Zhuang, Z. B. et al. Discovery of main group single Sb-N_4 active sites for CO_2 electroreduction to formate with high efficiency. *Energy Environ. Sci.* **2020**, *13*, 2856–2863.

[168] Shang, H. S.; Jiang, Z. L.; Zhou, D. N.; Pei, J. J.; Wang, Y.; Dong, J. C.; Zheng, X. S.; Zhang, J. T.; Chen, W. X. Engineering a metal-organic framework derived Mn-N_4-C_xS_y atomic interface for highly efficient oxygen reduction reaction. *Chem. Sci.* **2020**, *11*, 5994–5999.

[169] Han, G. K.; Zhang, X.; Liu, W.; Zhang, Q. H.; Wang, Z. Q.; Cheng, J.; Yao, T.; Gu, L.; Du, C. Y.; Gao, Y. Z. et al. Substrate strain tunes operando geometric distortion and oxygen reduction activity of CuN_2C_2 single-atom sites. *Nat. Commun.* **2021**, *12*, 6335.

[170] Fang, M. W.; Wang, X. P.; Li, X. Y.; Zhu, Y.; Xiao, G. Z.; Feng, J. J.; Jiang, X. H.; Lv, K. L.; Zhu, Y.; Lin, W. F. Curvature-induced Zn 3D electron return on Zn-N_4 single-atom carbon nanofibers for boosting electroreduction of CO_2. *ChemCatChem* **2021**, *13*, 603–609.

[171] Zhang, J.; Wang, Z. Y.; Chen, W. X.; Xiong, Y.; Cheong, W. C.; Zheng, L. R.; Yan, W. S.; Gu, L.; Chen, C.; Peng, Q. et al. Tuning polarity of Cu–O bond in heterogeneous Cu catalyst to promote additive-free hydroboration of alkynes. *Chem* **2020**, *6*, 725–737.

[172] Calle-Vallejo, F.; Tymoczko, J.; Colic, V.; Vu, Q. H.; Pohl, M. D.; Morgenstern, K.; Loffreda, D.; Sautet, P.; Schuhmann, W.; Bandarenka, A. S. Finding optimal surface sites on heterogeneous catalysts by counting nearest neighbors. *Science* **2015**, *350*, 185–189.

[173] Cao, S. W.; Tao, F. F.; Tang, Y.; Li, Y. T.; Yu, J. G. Size- and shape-dependent catalytic performances of oxidation and reduction reactions on nanocatalysts. *Chem. Soc. Rev.* **2016**, *45*, 4747–4765.

[174] Wang, H. T.; Xu, S. C.; Tsai, C.; Li, Y. Z.; Liu, C.; Zhao, J.; Liu, Y. Y.; Yuan, H. Y.; Abild-Pedersen, F.; Prinz, F. B. et al. Direct and continuous strain control of catalysts with tunable battery electrode materials. *Science* **2016**, *354*, 1031–1036.

[175] Bu, L. Z.; Zhang, N.; Guo, S. J.; Zhang, X.; Li, J.; Yao, J. L.; Wu, T.; Lu, G.; Ma, J. Y.; Su, D. et al. Biaxially strained PtPb/Pt core/shell nanoplate boosts oxygen reduction catalysis. *Science* **2016**, *354*, 1410–1414.

[176] Yao, Y. C.; Hu, S. L.; Chen, W. X.; Huang, Z. Q.; Wei, W. C.; Yao, T.; Liu, R. R.; Zang, K. T.; Wang, X. Q.; Wu, G. et al. Engineering the electronic structure of single atom Ru sites via compressive strain boosts acidic water oxidation electrocatalysis. *Nat. Catal.* **2019**, *2*, 304–313.

[177] Bian, T.; Zhang, H.; Jiang, Y. Y.; Jin, C. H.; Wu, J. B.; Yang, H.; Yang, D. R. Epitaxial growth of twinned Au-Pt core–shell star-shaped decahedra as highly durable electrocatalysts. *Nano Lett.* **2015**, *15*, 7808–7815.

[178] Zhang, X.; Liu, Y. X.; Deng, J. G.; Yu, X. H.; Han, Z.; Zhang, K. F.; Dai, H. X. Alloying of gold with palladium: An effective strategy to improve catalytic stability and chlorine-tolerance of the 3DOM CeO_2-supported catalysts in trichloroethylene combustion. *Appl. Catal. B Environ.* **2019**, *257*, 117879.

[179] Cai, S. F.; Duan, H. H.; Rong, H. P.; Wang, D. S.; Li, L.; He, W.; Li, Y. D. Highly active and selective catalysis of bimetallic Rh_3Ni_1 nanoparticles in the hydrogenation of nitroarenes. *ACS Catal.* **2013**, *3*, 608–612.

[180] Strasser, P.; Koh, S.; Anniyev, T.; Greeley, J.; More, K.; Yu, C. F.; Liu, Z. C.; Kaya, S.; Nordlund, D.; Ogasawara, H. et al. Lattice-strain control of the activity in dealloyed core–shell fuel cell catalysts. *Nat. Chem.* **2010**, *2*, 454–460.

[181] Matsubu, J. C.; Zhang, S. Y.; DeRita, L.; Marinkovic, N. S.; Chen, J. G.; Graham, G. W.; Pan, X. Q.; Christopher, P. Adsorbate-mediated strong metal–support interactions in oxide-supported Rh catalysts. *Nat. Chem.* **2017**, *9*, 120–127.

[182] Liu, P. X.; Qin, R. X.; Fu, G.; Zheng, N. F. Surface coordination chemistry of metal nanomaterials. *J. Am. Chem. Soc.* **2017**, *139*, 2122–2131.

[183] Kattel, S.; Ramírez, P. J.; Chen, J. G.; Rodriguez, J. A.; Liu, P. Active sites for CO_2 hydrogenation to methanol on Cu/ZnO

catalysts. *Science* **2017**, *355*, 1296–1299.
[184] Schoenbaum, C. A.; Schwartz, D. K.; Medlin, J. W. Controlling the surface environment of heterogeneous catalysts using self-assembled monolayers. *Acc. Chem. Res.* **2014**, *47*, 1438–1445.
[185] Mao, J. J.; Chen, W. X.; Sun, W. M.; Chen, Z.; Pei, J. J.; He, D. S.; Lv, C. L.; Wang, D. S.; Li, Y. D. Rational control of the selectivity of a ruthenium catalyst for hydrogenation of 4-nitrostyrene by strain regulation. *Angew. Chem., Int. Ed.* **2017**, *56*, 11971–11975.
[186] Ye, C. L.; Peng, M.; Wang, Y. H.; Zhang, N. Q.; Wang, D. S.; Jiao, M. L.; Miller, J. T. Surface hexagonal Pt_1Sn_1 intermetallic on Pt nanoparticles for selective propane dehydrogenation. *ACS Appl. Mater. Interfaces* **2020**, *12*, 25903–25909.
[187] Wang, C. Y.; Sang, X. H.; Gamler, J. T. L.; Chen, D. P.; Unocic, R. R.; Skrabalak, S. E. Facet-dependent deposition of highly strained alloyed shells on intermetallic nanoparticles for enhanced electrocatalysis. *Nano Lett.* **2017**, *17*, 5526–5532.
[188] Escudero-Escribano, M.; Malacrida, P.; Hansen, M. H.; Vej-Hansen, U. G.; Velázquez-Palenzuela, A.; Tripkovic, V.; Schiøtz, J.; Rossmeisl, J.; Stephens, I. E. L.; Chorkendorff, I. Tuning the activity of Pt alloy electrocatalysts by means of the lanthanide contraction. *Science* **2016**, *352*, 73–76.
[189] Feng, Q. C.; Zhao, S.; He, D. S.; Tian, S. B.; Gu, L.; Wen, X. D.; Chen, C.; Peng, Q.; Wang, D. S.; Li, Y. D. Strain engineering to enhance the electrooxidation performance of atomic-layer Pt on intermetallic Pt_3Ga. *J. Am. Chem. Soc.* **2018**, *140*, 2773–2776.
[190] Cheng, Q. Q.; Yang, S.; Fu, C. C.; Zou, L. L.; Zou, Z. Q.; Jiang, Z.; Zhang, J. L.; Yang, H. High-loaded sub-6 nm Pt_1Co_1 intermetallic compounds with highly efficient performance expression in PEMFCs. *Energy Environ. Sci.* **2022**, *15*, 278–286.
[191] Wang, D. C.; Xin, H. L.; Hovden, R.; Wang, H. S.; Yu, Y. C.; Muller, D. A.; DiSalvo, F. J.; Abruña, H. D. Structurally ordered intermetallic platinum-cobalt core–shell nanoparticles with enhanced activity and stability as oxygen reduction electrocatalysts. *Nat. Mater.* **2013**, *12*, 81–87.
[192] Serna, P.; Concepción, P.; Corma, A. Design of highly active and chemoselective bimetallic gold-platinum hydrogenation catalysts through kinetic and isotopic studies. *J. Catal.* **2009**, *265*, 19–25.
[193] Guan, Q. Q.; Zhu, C. W.; Lin, Y.; Vovk, E. I.; Zhou, X. H.; Yang, Y.; Yu, H. C.; Cao, L. N.; Wang, H. W.; Zhang, X. H. et al. Bimetallic monolayer catalyst breaks the activity-selectivity trade-off on metal particle size for efficient chemoselective hydrogenations. *Nat. Catal.* **2021**, *4*, 840–849.
[194] Feng, Q. C.; Zhao, S.; Wang, Y.; Dong, J. C.; Chen, W. X.; He, D. S.; Wang, D. S.; Yang, J.; Zhu, Y. M.; Zhu, H. L. et al. Isolated single-atom Pd sites in intermetallic nanostructures: High catalytic selectivity for semihydrogenation of alkynes. *J. Am. Chem. Soc.* **2017**, *139*, 7294–7301.
[195] Li, C. C.; Nakagawa, Y.; Yabushita, M.; Nakayama, A.; Tomishige, K. Guaiacol hydrodeoxygenation over iron-ceria catalysts with platinum single-atom alloy clusters as a promoter. *ACS Catal.* **2021**, *11*, 12794–12814.
[196] Van Der Linden, M.; Van Bunningen, A. J.; Amidani, L.; Bransen, M.; Elnaggar, H.; Glatzel, P.; Meijerink, A.; De Groot, F. M. F. Single Au atom doping of silver nanoclusters. *ACS Nano* **2018**, *12*, 12751–12760.
[197] Bai, L. C.; Hsu, C. S.; Alexander, D. T. L.; Chen, H. M.; Hu, X. L. Double-atom catalysts as a molecular platform for heterogeneous oxygen evolution electrocatalysis. *Nat. Energy* **2021**, *6*, 1054–1066.
[198] Jiang, M.; Wang, F.; Yang, F.; He, H.; Yang, J.; Zhang, W.; Luo, J. Y.; Zhang, J.; Fu, C. P. Rationalization on high-loading iron and cobalt dual metal single atoms and mechanistic insight into the oxygen reduction reaction. *Nano Energy* **2022**, *93*, 106793.
[199] Jiao, J. Q.; Lin, R.; Liu, S. J.; Cheong, W. C.; Zhang, C.; Chen, Z.; Pan, Y.; Tang, J. G.; Wu, K. L.; Hung, S. F. et al. Copper atom-pair catalyst anchored on alloy nanowires for selective and efficient electrochemical reduction of CO_2. *Nat. Chem.* **2019**, *11*, 222–228.
[200] Tian, S. B.; Fu, Q.; Chen, W. X.; Feng, Q. C.; Chen, Z.; Zhang, J.; Cheong, W. C.; Yu, R.; Gu, L.; Dong, J. C. et al. Carbon nitride supported Fe_2 cluster catalysts with superior performance for alkene epoxidation. *Nat. Commun.* **2018**, *9*, 2353.
[201] Wang, X.; Li, Y.; Wang, Y.; Zhang, H.; Jin, Z.; Yang, X. L.; Shi, Z. P.; Liang, L.; Wu, Z. J.; Jiang, Z. et al. Proton exchange membrane fuel cells powered with both CO and H_2. *Proc. Natl. Acad. Sci. USA* **2021**, *118*, e2107332118.
[202] Wei, Y. S.; Sun, L. M.; Wang, M.; Hong, J. H.; Zou, L. L.; Liu, H. W.; Wang, Y.; Zhang, M.; Liu, Z.; Li, Y. W. et al. Fabricating dual-atom iron catalysts for efficient oxygen evolution reaction: A heteroatom modulator approach. *Angew. Chem., Int. Ed.* **2020**, *59*, 16013–16022.
[203] Liu, P. X.; Huang, X.; Mance, D.; Copéret, C. Atomically dispersed iridium on MgO (111) nanosheets catalyses benzene–ethylene coupling towards styrene. *Nat. Catal.* **2021**, *4*, 968–975.
[204] Su, X.; Jiang, Z.; Zhou, J.; Liu, H.; Zhou, D.; Shang, H.; Ni, X.; Peng, Z.; Yang, F.; Chen, W., et al. Complementary operando spectroscopy identification of *in-situ* generated metastable charge-asymmetry Cu_2-CuN_3 clusters for CO_2 reduction to ethanol. *Nat. Commun.* **2022**, *13*, 1322.
[205] Liang, Z.; Song, L. P.; Sun, M. Z.; Huang, B. L.; Du, Y. P. Tunable CO/H_2 ratios of electrochemical reduction of CO_2 through the Zn-Ln dual atomic catalysts. *Sci. Adv.* **2021**, *7*, eabl4915.
[206] Lin, R.; Ma, X. L.; Cheong, W. C.; Zhang, C.; Zhu, W.; Pei, J. J.; Zhang, K. Y.; Wang, B.; Liang, S. Y.; Liu, Y. X. et al. PdAg bimetallic electrocatalyst for highly selective reduction of CO_2 with low $COOH^*$ formation energy and facile CO desorption. *Nano Res.* **2019**, *12*, 2866–2871.
[207] Mao, J. J.; Yin, J. S.; Pei, J. J.; Wang, D. S.; Li, Y. D. Single atom alloy: An emerging atomic site material for catalytic applications. *Nano Today* **2020**, *34*, 100917.
[208] Zheng, T. T.; Liu, C. X.; Guo, C. X.; Zhang, M. L.; Li, X.; Jiang, Q.; Xue, W. Q.; Li, H. L.; Li, A. W.; Pao, C. W. et al. Copper-catalysed exclusive CO_2 to pure formic acid conversion via single-atom alloying. *Nat. Nanotechnol.* **2021**, *16*, 1386–1393.
[209] Pang, B. B.; Liu, X. K.; Liu, T. Y.; Chen, T.; Shen, X. Y.; Zhang, W.; Wang, S. C.; Liu, T.; Liu, D.; Ding, T. et al. Laser-assisted high-performance PtRu alloy for pH-universal hydrogen evolution. *Energy Environ. Sci.* **2022**, *15*, 102–108.
[210] Meng, G.; Sun, J. Q.; Tao, L.; Ji, K. Y.; Wang, P. F.; Wang, Y.; Sun, X. H.; Cui, T. T.; Du, S. X.; Chen, J. G. et al. Ru_1Co_n single-atom alloy for enhancing Fischer–Tropsch synthesis. *ACS Catal.* **2021**, *11*, 1886–1896.
[211] Kang, J. C. ; Fan, Q. Y. ; Zhou, W. ; Zhang, Q. H. ; He, S. ; Yue, L. X. ; Tang, Y. ; Nguyen, L. ; Yu, X. ; You, Y. et al. Iridium boosts the selectivity and stability of cobalt catalysts for syngas to liquid fuels. *Chem*, in press, https://doi.org/10.1016/j.chempr.2021.12.016.
[212] Mao, J. J.; He, C. T.; Pei, J. J.; Chen, W. X.; He, D. S.; He, Y. Q.; Zhuang, Z. B.; Chen, C.; Peng, Q.; Wang, D. S. et al. Accelerating water dissociation kinetics by isolating cobalt atoms into ruthenium lattice. *Nat. Commun.* **2018**, *9*, 4958.
[213] Giannakakis, G.; Kress, P.; Duanmu, K.; Ngan, H. T.; Yan, G.; Hoffman, A. S.; Qi, Z.; Trimpalis, A.; Annamalai, L.; Ouyang, M. Y. et al. Mechanistic and electronic insights into a working NiAu single-atom alloy ethanol dehydrogenation catalyst. *J. Am. Chem. Soc.* **2021**, *143*, 21567–21579.
[214] Liu, Y. X.; Liu, X. W.; Feng, Q. C.; He, D. S.; Zhang, L. B.; Lian, C.; Shen, R. G.; Zhao, G. F.; Ji, Y. J.; Wang, D. S. et al. Intermetallic Ni_xM_y (M = Ga and Sn) nanocrystals: A non-precious metal catalyst for semi-hydrogenation of alkynes. *Adv. Mater.* **2016**, *28*, 4747–4754.
[215] Cao, Y. Q.; Zhang, H.; Ji, S. F.; Sui, Z.; Jiang, Z.; Wang, D. S.; Zaera, F.; Zhou, X. G.; Duan, X. Z.; Li, Y. D. Adsorption site regulation to guide atomic design of Ni-Ga catalysts for acetylene semi-hydrogenation. *Angew. Chem., Int. Ed.* **2020**, *59*, 11647–11652.
[216] Zhang, L.; Wang, Q.; Li, L. L.; Banis, M. N.; Li, J. J.; Adair, K.; Sun, Y. P.; Li, R. Y.; Zhao, Z. J.; Gu, M. et al. Single atom surface engineering: A new strategy to boost electrochemical activities of Pt catalysts. *Nano Energy* **2022**, *93*, 106813.
[217] Peng, Y. H.; Geng, Z. G.; Zhao, S. T.; Wang, L. B.; Li, H. L.; Wang, X.; Zheng, X. S.; Zhu, J. F.; Li, Z. Y.; Si, R. et al. Pt single

atoms embedded in the surface of Ni nanocrystals as highly active catalysts for selective hydrogenation of nitro compounds. *Nano Lett.* **2018**, *18*, 3785–3791.

[218] Ding, J. B.; Ji, Y. J.; Li, Y. Y.; Hong, G. Monoatomic platinum-embedded hexagonal close-packed nickel anisotropic superstructures as highly efficient hydrogen evolution catalyst. *Nano Lett.* **2021**, *21*, 9381–9387.

[219] Mao, J. J.; He, C. T.; Pei, J. J.; Liu, Y.; Li, J.; Chen, W. X.; He, D. S.; Wang, D. S.; Li, Y. D. Isolated Ni atoms dispersed on Ru nanosheets: High-performance electrocatalysts toward hydrogen oxidation reaction. *Nano Lett.* **2020**, *20*, 3442–3448.

[220] Long, R.; Li, Y.; Liu, Y.; Chen, S. M.; Zheng, X. S.; Gao, C.; He, C. H.; Chen, N. S.; Qi, Z. M.; Song, L. et al. Isolation of Cu atoms in Pd lattice: Forming highly selective sites for photocatalytic conversion of CO_2 to CH_4. *J. Am. Chem. Soc.* **2017**, *139*, 4486–4492.

[221] Cheng, H. Y.; Wu, X. M.; Feng, M. M.; Li, X. C.; Lei, G. P.; Fan, Z. H.; Pan, D. W.; Cui, F. J.; He, G. H. Atomically dispersed Ni/Cu dual sites for boosting the CO_2 reduction reaction. *ACS Catal.* **2021**, *11*, 12673–12681.

[222] Tian, S. B.; Wang, B. X.; Gong, W. B.; He, Z. Z.; Xu, Q.; Chen, W. X.; Zhang, Q. H.; Zhu, Y. Q.; Yang, J. R.; Fu, Q. et al. Dual-atom Pt heterogeneous catalyst with excellent catalytic performances for the selective hydrogenation and epoxidation. *Nat. Commun.* **2021**, *12*, 3181.

[223] Wang, J. M.; Kim, E.; Kumar, D. P.; Rangappa, A. P.; Kim, Y.; Zhang, Y. X.; Kim, T. K. Highly durable and fully dispersed cobalt diatomic site catalysts for CO_2 photoreduction to CH_4. *Angew. Chem., Int. Ed.* **2022**, *61*, e202113044.

[224] Cao, X. Y.; Zhao, L. L.; Wulan, B.; Tan, D. X.; Chen, Q. W.; Ma, J. Z.; Zhang, J. T. Atomic bridging structure of nickel-nitrogen-carbon for highly efficient electrocatalytic reduction of CO_2. *Angew. Chem., Int. Ed.* **2022**, *61*, e202113918.

[225] Liu, M.; Li, N.; Cao, S. F.; Wang, X. M.; Lu, X. Q.; Kong, L. J.; Xu, Y. H.; Bu, X. H. A "pre-constrained metal twins" strategy to prepare efficient dual-metal-atom catalysts for cooperative oxygen electrocatalysis. *Adv. Mater.* **2022**, *34*, 2107421.

[226] Kumar, A.; Bui, V. Q.; Lee, J.; Wang, L. L.; Jadhav, A. R.; Liu, X. H.; Shao, X. D.; Liu, Y.; Yu, J. M.; Hwang, Y. et al. Moving beyond bimetallic-alloy to single-atom dimer atomic-interface for all-pH hydrogen evolution. *Nat. Commun.* **2021**, *12*, 6766.

[227] Jiao, L.; Zhu, J. T.; Zhang, Y.; Yang, W. J.; Zhou, S. Y.; Li, A. W.; Xie, C. F.; Zheng, X. S.; Zhou, W.; Yu, S. H. et al. Non-bonding interaction of neighboring Fe and Ni single-atom pairs on MOF-derived N-doped carbon for enhanced CO_2 electroreduction. *J. Am. Chem. Soc.* **2021**, *143*, 19417–19424.

[228] Chen, J. Y.; Li, H.; Fan, C.; Meng, Q. W.; Tang, Y. W.; Qiu, X. Y.; Fu, G. T.; Ma, T. Y. Dual single-atomic Ni-N_4 and Fe-N_4 sites constructing Janus hollow graphene for selective oxygen electrocatalysis. *Adv. Mater.* **2020**, *32*, 2003134.

[229] Chen, G. B.; Liu, P.; Liao, Z. Q.; Sun, F. F.; He, Y. H.; Zhong, H. X.; Zhang, T.; Zschech, E.; Chen, M. W.; Wu, G. et al. Zinc-mediated template synthesis of Fe-N-C electrocatalysts with densely accessible Fe-N_x active sites for efficient oxygen reduction. *Adv. Mater.* **2020**, *32*, 1907399.

[230] Wang, X.; Jia, Y.; Mao, X.; Liu, D. B.; He, W. X.; Li, J.; Liu, J. G.; Yan, X. C.; Chen, J.; Song, L. et al. Edge-rich Fe-N_4 active sites in defective carbon for oxygen reduction catalysis. *Adv. Mater.* **2020**, *32*, 2000966.

[231] Han, A. L.; Wang, X. J.; Tang, K.; Zhang, Z. D.; Ye, C. L.; Kong, K. J.; Hu, H. B.; Zheng, L. R.; Jiang, P.; Zhao, C. X. et al. An adjacent atomic platinum site enables single-atom iron with high oxygen reduction reaction performance. *Angew. Chem., Int. Ed.* **2021**, *60*, 19262–19271.

[232] Sun, M. Z.; Wu, T.; Dougherty, A. W.; Lam, M.; Huang, B. L.; Li, Y. L.; Yan, C. H. Self-validated machine learning study of graphdiyne-based dual atomic catalyst. *Adv. Energy Mater.* **2021**, *11*, 2003796.

[233] Sun, M. Z.; Wong, H. H.; Wu, T.; Dougherty, A. W.; Huang, B. L. Stepping out of transition metals: Activating the dual atomic catalyst through main group elements. *Adv. Energy Mater.* **2021**, *11*, 2101404.

[234] Huang, Z. F.; Song, J. J.; Dou, S.; Li, X. G.; Wang, J.; Wang, X. Strategies to break the scaling relation toward enhanced oxygen electrocatalysis. *Matter* **2019**, *1*, 1494–1518.

[235] Shen, X. C.; Nagai, T.; Yang, F. P.; Zhou, L. Q.; Pan, Y. B.; Yao, L. B.; Wu, D. Z.; Liu, Y. S.; Feng, J.; Guo, J. H. et al. Dual-site cascade oxygen reduction mechanism on SnO_x/Pt-Cu-Ni for promoting reaction kinetics. *J. Am. Chem. Soc.* **2019**, *141*, 9463–9467.

[236] Gao, R. J.; Wang, J.; Huang, Z. F.; Zhang, R. R.; Wang, W.; Pan, L.; Zhang, J. F.; Zhu, W. K.; Zhang, X. W.; Shi, C. X. et al. Pt/Fe_2O_3 with Pt–Fe pair sites as a catalyst for oxygen reduction with ultralow Pt loading. *Nat. Energy* **2021**, *6*, 614–623.

[237] Gao, R. J.; Xu, J. S.; Wang, J.; Lim, J.; Peng, C.; Pan, L.; Zhang, X. W.; Yang, H. M.; Zou, J. J. Pd/Fe_2O_3 with electronic coupling single-site Pd–Fe pair sites for low-temperature semihydrogenation of alkynes. *J. Am. Chem. Soc.* **2022**, *144*, 573–581.

[238] Yin, H. B.; Chen, Z.; Peng, Y.; Xiong, S. C.; Li, Y. D.; Yamashita, H.; Li, J. H. Dual active centers bridged by oxygen vacancies of ruthenium single-atom hybrids supported on molybdenum oxide for photocatalytic ammonia synthesis. *Angew. Chem., Int. Ed.* **2022**, *61*, e202114242.

[239] Ji, S. F.; Chen, Y. J.; Fu, Q.; Chen, Y. F.; Dong, J. C.; Chen, W. X.; Li, Z.; Wang, Y.; Gu, L.; He, W. et al. Confined pyrolysis within metal-organic frameworks to form uniform Ru_3 clusters for efficient oxidation of alcohols. *J. Am. Chem. Soc.* **2017**, *139*, 9795–9798.

[240] Ji, S. F.; Chen, Y. J.; Zhao, S.; Chen, W. X.; Shi, L. J.; Wang, Y.; Dong, J. C.; Li, Z.; Li, F. W.; Chen, C. et al. Atomically dispersed ruthenium species inside metal-organic frameworks: Combining the high activity of atomic sites and the molecular sieving effect of MOFs. *Angew. Chem., Int. Ed.* **2019**, *58*, 4271–4275.

[241] Meng, F. C.; Peng, M.; Chen, Y. L.; Cai, X. B.; Huang, F.; Yang, L. N.; Liu, X.; Li, T.; Wen, X. D.; Wang, N. et al. Defect-rich graphene stabilized atomically dispersed Cu_3 clusters with enhanced oxidase-like activity for antibacterial applications. *Appl. Catal. B Environ.* **2022**, *301*, 120826.

[242] Gu, J.; Jian, M. Z.; Huang, L.; Sun, Z. H.; Li, A. W.; Pan, Y.; Yang, J. Z.; Wen, W.; Zhou, W.; Lin, Y. et al. Synergizing metal–support interactions and spatial confinement boosts dynamics of atomic nickel for hydrogenations. *Nat. Nanotechnol.* **2021**, *16*, 1141–1149.

[243] Peng, Y. K.; Hu, Y. C.; Chou, H. L.; Fu, Y. Y.; Teixeira, I. F.; Zhang, L.; He, H. Y.; Tsang, S. C. E. Mapping surface-modified titania nanoparticles with implications for activity and facet control. *Nat. Commun.* **2017**, *8*, 675.

[244] Zhang, J. R.; Wu, T. S.; Thang, H. V.; Tseng, K. Y.; Hao, X. D.; Xu, B. S.; Chen, H. Y. T.; Peng, Y. K. Cluster nanozymes with optimized reactivity and utilization of active sites for effective peroxidase (and oxidase) mimicking. *Small* **2022**, *18*, 2104844.